August 2019

Towards real-time monitoring of bacterial cultures without the need for physical sampling: elastic scattering, fluorescence and Raman spectroscopy of Escherichia coli cultures.

Richard Thomas McDonough
Syracuse University

Recommended Citation

McDonough, Richard Thomas, "Towards real-time monitoring of bacterial cultures without the need for physical sampling: elastic scattering, fluorescence and Raman spectroscopy of Escherichia coli cultures." (2019). *Dissertations - ALL*. 1099.
https://surface.syr.edu/etd/1099

ABSTRACT

The first part of this dissertation pertains to the fringe analysis of a hydration layer that forms spontaneously when biofilms dry. This layer at optical thickness < 20 µm is approximately 1-2 orders of magnitude thinner than the biofilm thickness as measured by confocal Raman microscopy and confocal fluorescent microscopy. Drying/rehydration experiments performed on films withstood multiple cycles, returning to the same optical thickness proving their robust nature. The strength of a distinct water peak (1451 nm) in addition to others, reflects the thickness of the hydration layer. Confocal Raman microscopy showed that biofilms are chemically very similar to pure alginate (synthetic) films. This shows that spontaneous formation of the hydration layer is a chemical process verses a biological process. The second chapter presents real-time, noninvasive, quantitative analysis of bacterial cultures for cell count and glucose uptake using turbidity corrected spectroscopy and Raman. We hypothesize that a Raman feature we ascribe to “biomass” (~1060 cm^{-1}) i.e. a υ(C-O-C) asymmetric stretch or (C-C) stretch, and a glucose peak (~1140 cm^{-1}) i.e. the υ(C–O) and/or υ(C–C) stretch allow for the real-time monitoring of cell count and nutrient depletion. We calibrated this technique to be backward compatible with OD600 for characterizing culture number density. The method involves irradiating a culture in fluid medium (LB/MM) in a quartz cuvette using a NIR laser (785 nm) and collecting all backscattered light from the cuvette. This approach may be useful in a broad range of academic/industrial applications that utilize bacterial cultures.

Towards real-time monitoring of bacterial cultures without the need for physical sampling: elastic scattering, fluorescence and Raman spectroscopy of Escherichia coli cultures.

by

Richard T. McDonough

B.A., West Virginia University, 2010

M.Phil., Syracuse University, 2015

Dissertation

Submitted in partial fulfillment of the requirements for the degree of

Doctor of Philosophy in Chemistry

Syracuse University

August 2019

To my loving family and friends.

ACKNOWLEDGMENTS

I would like to thank multiple people for all their support throughout my time at Syracuse University. Without the help and support of these individuals this work would not have been possible. My advisor Dr. Joseph Chaiken is the first person I would like to offer my sincere thanks for all the wisdom he passed on to me. He has encouraged and inspired me over the last five years which helped me to reach my full potential and landing me the professional career I have today.

I would like to acknowledge my PhD committee members Dr. Timothy Korter and Dr. Bruce Hudson for their valuable discussions and suggestions which helped me to successfully continue my research work throughout the years.

I would like to acknowledge my research group members from the past and present; Dr. Paul Dent, Seth Fillioe, Steve Ortiz, and Minh Quan Hoang Dinh for not only assisting me throughout the process but also continuing my research. Thank you for always being there for me and for all your collaboration in the lab.

I want to thank Dr. R. P. Doyle research group of Syracuse University for providing the Escherichia coli culture and training in culturing biological samples, and Dr. Yan-Yeung Luk research group of Syracuse University for providing knowledge on biofilms and collaborative research.

I am grateful for my friends and colleagues Dr. Alexandre Dixon, Dr. Hewen Zheng, Dr. Shawn Kowal, Dr. Jared Grossman and many others for their wisdom, guidance and ability to make graduate school enjoyable.

I would like to thank the gentlemen in the Machine Shop Lou Buda, Phil Arnold, and Charlie Brown for making my temperature-controlled base used for my research, Sally Prasch for some of the custom glass components used in the analysis of biofilms, and Mike Brandt for helping to make random electronics to help me complete my research.

I would also like to thank Cathy Vorhees, Jodi Randall, Beth Molloy, and April LePage for all their help as I made my transition to Syracuse University.

I am grateful for Syracuse University, the Department of Chemistry and the Graduate College for all the funding and support they provided throughout my research work.

Finally, I would like to thank my family, Joanna Bunker and my friends from the Syracuse area, for their support and encouragement. Thank you for being there for me with all the successes and shortcomings throughout my time at Syracuse University.

TABLE OF CONTENTS

LIST OF TABLES

LIST OF FIGURES

CHAPTER 1

INTRODUCTION

The primary region of light used to probe biological systems *in vivo* is the near-infrared (NIR). The whole NIR region is between 780-2500 nm but the “physiological window” through which virtually any biological system is *assumed* to be unperturbed is from about 780-1350 nm.[1] This part of the spectrum was often ignored in the past partly due to very broad and overlapping peaks in absorption. In this range the photon energy is too high in energy to excite pure fundamental vibrations and too low to excite all but the most conjugated electronic systems, or in some cases metals.[2] Instead the actual vibrations excited by absorption in the NIR are overtones and combinations. Recently, the enabling technologies for performing Raman spectroscopy in the NIR have improved considerably allowing advances in analyzing microscopic samples in a way that is nondestructive.[3, 4] This thesis concerns the NIR exclusively because it alone offers the possibility of probing biological systems in a manner that simultaneously gives qualitative and quantitative access to analytes’ vibrational fundamentals while being very insensitive to water, which is a part of every known living system.

Raman spectroscopy permits gathering qualitative and quantitative data in a variety of applications such as environmental, pharmaceutical, food, and clinical applications.[5-14] There are many different types of Raman instruments and each instrument has a unique setup that allows it to have added benefits for different types of analysis. Surface enhanced Raman spectroscopy (SERS)[15, 16] requires a rough metal substrate to enhance the local electric field allowing for an increase of signal from adsorbed species. People have proposed to insert metal substrates into people’s skin and to do SERS as a means of “noninvasive” glucose monitoring.[17] When studying molecules like with accessible electronic transitions, “resonance Raman” spectroscopy can be used.[18] Using this technique, you can target different molecules by selecting the laser wavelength closest to an absorption maximum for that molecule. This technique is great for single molecule analysis, but relies heavily on the laser being tunable or having multiple lasers at different wavelengths. A disadvantage of resonance Raman spectroscopy is that irradiating a molecule that absorbs the incident laser light usually causes heating and decomposition.

There is even a combination of these two which utilizes the added benefits of both.[19] Raman microscopes, with or without confocal capability are capable of increased spatial resolution, including in the plane normal to the laser, which allows for the accurate analysis of complex systems like synthetic and biological films.[20, 21] While all these techniques have their advantages and disadvantages, most commercial Raman instruments are designed to completely remove the Rayleigh-Mie line. All the research done in this dissertation used a custom designed Raman instrument that allows for the Rayleigh-Mie line to be present while not saturating the detector. This setup is shown and explained more in Chapter 3.

What benefit does having simultaneous access to the Rayleigh/Mie line afford us? There are two major issues in the spectroscopic probing of biological media once one has accounted for the overwhelming presence of water. First, all biological media are turbid and so to do spectroscopy in such media, one must account for the physical propagation of the light in addition to the spectroscopic interactions e.g. Raman and fluorescence emission. For this, we describe the adaptation of a new recently created algorithm for noninvasive *in vivo* blood and tissue analysis i.e. Binary spectronephelometry in this thesis.

The second major difficulty with Raman spectroscopy of biological media results from the necessity to extract the relatively narrow useful spectral data from the broad spectral features. Interestingly, all biological media fluoresce under NIR excitation so Raman spectra of virtually all biological samples require some pre-processing before choosing a chemometric or other method to analyze the data. While there have been schemes[22, 23] applied involving the way and kind of Raman data collected to address this issue, to date it has not been possible to separate the fluorescence from the Raman emission. Addressing this issue in post processing is termed "baseline correction".

All the Raman data shown in this dissertation initially had all spectral spikes removed, had a "101-7" baseline correction applied, and then principal component analysis (PCA) or our own binary spectronephelometry (BSN) algorithm applied. Spectral spikes in CCD data are caused by cosmic rays[24, 25] and cause easily recognized artifacts within the 101-7 smoothing technique or any if not removed.

The initial step in any chemometric technique is not to assume anything about the nature of the data. While some people prefer using a standard normal variant transform to achieve a zero baseline[22, 23, 26], we achieve the same thing in one step using the 101-7 point smoothing technique.[27, 28] This technique was determined to be the best for the spectra our Raman setup produces and is discussed in more detail in Chapter 3. There are many different types of chemometric methods[29-33] that can be applied to a Raman spectrum, but for our analysis we found PCA and our own BSN algorithm to be useful. Both chemometric methods will be discussed further in Chapter 3.

There are many ways to analyze bacterial cultures ranging from UV/Vis spectrophotometry, flow cytometry, fluorescence microscopy, and automated cell counters. [20, 34-42] These techniques allow you to get accurate cell counts, but really cannot give detailed information about a micro bacterial culture in real-time. Flow cytometry, fluorescence microscope and automated cell counters normally require a fluorescent tag in the microorganism or dye to get accurate results.[20, 37-42] All techniques above require sampling of a culture for analysis which risks contamination and is an isolated representation of the culture. These techniques are not able to analyze a culture in real-time and are therefore isolated representations at fixed time points which is no longer an accurate representation of the continuously growing culture. Chapter 3 explains that using Raman spectroscopy we were able to get an accurate cell count using the Rayleigh-Mie line i.e. BSN and we were able to monitor glucose/nutrient uptake in real-time. Also, there is potential that using this technique will allow one to monitor product production. While no data is shown in this dissertation, this will be discussed further in Chapter 4 and can be seen in data that will appear in Steve Ortiz's thesis.

This thesis shows that given the improvement in all relevant enabling technologies and continuing endeavors to learn more about biological systems, we should be looking for ways to improve upon OD600 as a means for monitoring bacterial cultures and obtaining a quick rough estimate of culture density that can be traced backwards to dry weight. We propose that using BSN with Raman is a sensible and practical possible replacement. And so, in our first attempt to connect OD600 to BSN, we consistently observed interference fringes in OD600 data that would lead to measurement artifacts in using such data to estimate bacterial number density. A substantial part of this thesis concerns understanding the nature of this artifact, how it could affect OD600 measurements, and what about the presence and properties of such films may be significant in the contexts of understanding bacteria themselves and biofilms as materials for applications.

Biofilms are made of an extracellular polymeric substance that is produced by the microorganism[43-45], and we were able to get some quantitative data by utilizing some of the instruments discussed above. Microorganisms tend to stay towards the middle of the film, as observed using a fluorescence microscope to scan the depth of the film.[20] These films act as a protective barrier for the microorganism and allow the microorganisms to have a safe place to grow and multiply[43-45] which is why it makes sense to find a higher concentration of microorganisms in the center. We also performed a drying experiment and determined that films have the ability to retain liquid/resist drying out.[20] Biofilms and their properties will be discussed further in Chapter 2. Thin film fringe analysis using the UV/Vis spectrophotometer allowed us to get an accurate measurement of the film thickness and specifically a hydration layer present in the film. I discuss synthetic films some in Chapter 2 and elaborate further in Chapter 4. Much more research is currently ongoing by Minh Quan Hoang Dinh.

Determining physical properties of biofilms is difficult even in a film formed by a culture containing only a single kind of organism. There are various general theories about how biofilms are formed, but to a physical chemist not much is taken as fact. We know films are formed by a molecule(s) produced from the microorganism,[43-45] but how exactly does the polymeric molecule attach itself to the substrate? Many researchers theorize the organism attaches itself to the substrate, exudes chemical that then form the film around itself.[44, 45] Do the organisms attach themselves to the substrate and then produce the polymeric molecule?[45] This is one of the theories most prominent in the literature, but from our collaboration with the Luk Lab we find a higher concentration of microorganisms in the center of the film and none/trace amounts at the substrate surface.[20] Microorganisms move throughout the film but is that motion over a large/small spatial scale i.e. centimeters or in the range of 10^2-10^3 microns, or are they stuck in relatively fixed locations, never straying more than 10^0-10^1 microns? From work shown in this dissertation, we have reason to believe the microorganisms can move throughout the film forming channels and can slightly disrupt the film.[20, 45] Chapter 2 shows some preliminary analytical results in an effort to characterize biofilms.

Monitoring a cell culture in a laboratory setting is based on random sampling at set time points throughout a cultures growth phases using OD600 which is still the most common and widely accepted testing method for fast cell count.[34, 36, 46] Other methods were previously discussed, but Chapter 3 shows how Raman spectroscopy will be a useful tool for analysis of microorganisms. Chapter 3 shows the effects of temperature on a culture in real-time without ever having to remove isolated samples from the culture. We examined the difference between LB medium and chemically defined medium (minimal medium) and while chemically defined medium has less interfering peaks, Raman spectroscopy can still be a useful tool to monitor a culture regardless of the medium. Since we can monitor the glucose peak as well as cell count, we were able to measure and calculate, possibly for the first time the rate of glucose molecule uptake per organism per second in a culture over any given period of time. Chapter 3 shows a more analytical approach using Raman spectroscopy to analyze microorganisms in the growth medium.

The final chapter (Chapter 4) of this dissertation is an expansion of some of the key concepts in Chapters 2 and 3 as well as proposing potential future plans to continue on with this research. One of the first things that we plan to try is testing a wide range of microorganisms and confirming that our technique and method of testing could be a useful tool on a larger scale. While we are capable of monitoring glucose depletions as shown in Chapter 3, in my work no testing was performed on microorganisms that *produced* a product that was Raman active. Future testing on microorganisms that produce Raman active products would be an obvious next step to prove Raman spectroscopy as a useful tool for analyzing cell cultures. Chapter 4 discusses plans for future testing with synthetic films and their uses in medical, environmental and food applications.[47-54] We were able to determine some physical properties of a biofilm which is discussed further in Chapter 2, but further testing should be done to determine the effect of different chemicals on the structural integrity of biofilms.[55] Finally, Chapter 4 discusses some potential thoughts on testing the effects of heat production in a given culture due to the metabolism of glucose. Chapter 4 will go into more detail on all of these concepts and I hope future students in the Chaiken Lab will continue this research.

CHAPTER 2

OPTICAL INTERFERENCE PROBE OF BIOFILM HYDROLOGY: LABEL-FREE CHARACTERIZATION OF THE DYNAMIC HYDRATION BEHAVIOR OF NATIVE BIOFILMS

2.1. Introduction

Under conditions that permit proliferation, formation of biofilms on surfaces is ubiquitous[56] for many different types of microbes. Biofilms have special properties, providing a space that allows a microbial population to efficiently and deterministically go through the different biological stages of growth and regeneration. Over the course of their development biofilms[56] attain a complex internal structure containing channels and a heterogeneous distribution of different organic materials and microbes of different phenotypes.[57] These biofilms are important because they host a vastly different microbial biology than do bulk fluid media, and permit different signaling than that employed by planktonic microbes.[58] In addition, biofilms are believed to be involved in more than 80% of the sources of infectious diseases.[56] Because of their dynamic and complex structures, biofilms have been extremely difficult to characterize.

In this work, we seek to understand the hydrology of these films i.e. the properties, distribution, and circulation of water in the films. We use Raman spectroscopy, near infrared absorption spectroscopy, and physical optics i.e. optical interference to measure the hydration and optical thickness characteristic of biofilms. We show that biofilms have the capacity to form a hydrated interior layer, capable of displaying well-defined interference fringes, when the film is removed from the culture medium. Measurement of the interference patterns is a new method of characterization of biofilms. We show that biofilms produced under different conditions and by different organisms all have the capacity to produce this layered structure. Some properties of this hydrated layer may depend on the biology of the biofilm: i.e. microbial species, maturation time, choice of substrate, choice of culture medium, exposure to light and possibly other factors.

Oscillations in optical loss or “fringes” result from the interference between a straight-through beam and a beam reflected from the two interior surfaces of a thin film.[59] Their observation allows calculation of the thickness and refractive index of the film. Several criteria must be fulfilled for the interference to be observable. First, there must be a discontinuity in the refractive index across both surfaces of the film (the geometric mean of the index of refraction differences across both sides of the film determines the amplitude of the fringes).[57] Second, the refractive index must be sufficiently homogeneous throughout the material. Third, the interfaces of the film must be smooth on the scale of the wavelength of the light. Fourth, the optical thickness of the film must be greater than a quarter of the wavelength of the light.

The fringes, which span the ultraviolet to near infrared spectral range, allow simultaneous calculation of optical thickness and index of refraction. Conveniently, it is easy to also observe a vibrational overtone absorption band for water[60] at 1451 nm. From the strength of the 1451 nm absorption, we obtain the total water content of the films. Across a broad range of bacteria and growth conditions, there is a correspondence between the thickness calculated from the interference fringes and the strength of the 1451 nm absorption feature. Given the vast knowledge[58] of thin film optical interference and the readily attainable spectroscopic characterization of the chemical composition of a thin film, there are surprisingly few studies that characterize the hydration properties and the chemical properties e.g. in the context of bond vibrations of biofilms.

2.2. Experimental

2.2.1. Materials and Methods

BL21 Gold (DE3) *E. coli* (EC) with a pET27b(+) sapB vector insert was obtained from Dr. R. P. Doyle (Syracuse University, Syracuse) grown in Luria-Bertani (LB) with 5 µL of kanamycin (35 mg/mL) (IBI Scientific Peosta, IA). Wild type *P. aeruginosa*, (PAO1) were obtained from Dr. Guirong Wang (Upstate Medical University, Syracuse) and both bacteria were cultured and prepared for experiments as described below. PAO1-Green Fluorescent Protein (PAO1-GFP) strain (plasmid pSMC2 expresses GFP) obtained from Dr. Guirong Wang (Upstate Medical University, Syracuse).

Phosphate buffered saline (PBS) (1X solution) (ICN Biomedical Inc. Aurora, OH), DifcoTM M9 Minimal Salts and NaCl (Fisher Scientific), BactoTMTryptone (Becton, Dickson and Company Sparks, MD), and yeast extract (aMReSCO, Solon, OH) were used without further purification.

Films grown on quartz utilized Hellma Analytics High Precision 1 cm cuvettes made of Quartz Suprasil (#101-10-40). Films grown on polystyrene utilized disposable polystyrene cuvettes (0.48x0.48x1.73in, Dynalon 1.5mL UV-VIS Range Semi-Micro Cuvette #302225-0002). Microscopy was done on films grown on the same materials obtained from broken cuvettes. Polystyrene and quartz surfaces were all rinsed with ethanol and dried before introducing a culture that would eventually provide a film for analysis.

Sample Preparation of LB Medium: All the bacterial strains were grown in Luria-Bertani (LB) medium containing 10 g/L tryptone, 5 g/L yeast extract, and 10 g/L NaCl at 37 °C. The pH of the medium was maintained at 7.0 with NaOH. The medium was then autoclaved at 121°C for 15 min in a water bath.

Nearly all OD600 spectra were obtained using a Perkin Elmer Lambda 950 UV/Vis spectrophotometer but some results were obtained using an Agilent Cary 60 UV/Vis. Spectral scans to observe fringes as in Figure 2-2 used the Lambda 950 UV/VIS set to a 2 nm slit width, 1.0 s integration time, and 1.0 nm data interval. Before scanning the sample, the spectrometer was first normalized ("auto-zeroed") with an empty cuvette over the same wavelength range. For the time drive experiment in Figure 2-3 data was collected using the Perkin Elmer instrument at 1451 nm and a 2 nm slit width for 15 sec intervals over various durations of time as indicated in the figures.

Some films in Figure 2-4 (as indicated in the Supplemental Materials) were grown in a cuvette with a different type of stirring and temperature control, the sample being housed in a custom-made temperature-controlled base. Using a flexible temperature probe attachment connected to a Vernier LabQuest2 Logger Pro, temperature data was collected to ensure constant temperature conditions. The anodized aluminum base height is 3.5 cm and the cuvette height is 4.5 cm. These dimensions ensure that the sample i.e. cuvette is covered by the walls of the base to allow homogeneity in heating and or cooling of the sample, but still allows facile removal of the cuvette from the base for rinsing and other operations. A magnetic stirrer/micro stir bar was added to the setup in order to maintain constant stirring of samples during the experiments. The stirrer itself was modified from a commercial device so that the rotating magnet could be placed sufficiently close to the side of the base in order to pull the stir bar to the side of the cuvette. This ensured that the stir bar axis of rotation was perpendicular to the side surfaces of the cuvette on which the biofilms grew.

Sample Preparation for UV/VIS study in Figures 2-6 and 2-7: The culture was slowly poured out of the cuvette and the excess liquid was removed from the top of the cuvette. The data was collected, and the walls of the cuvette were gently rinsed with 1 mL of PBS or deuterated PBS (DPBS) as indicated in the Figures. The PBS or DPBS was removed in the same way as the initial culture. This procedure was repeated for each rinse.

E. coli (EC) sample preparation for Biofilm Drying Experiment (Figures 2-6 and 2-7): To prepare native culture (NC), 5 mL of LB with 5 µL of kanamycin was inoculated with EC and allowed to grow over a 24 hr period in an incubator at 37°C with shaking at 250 rpm. Then 200 µL of NC was used to inoculate a new 5.0 mL sample of LB with 5 µL of kendomycin. Then 3.50 mL of newly inoculated culture were placed in the quartz cuvette, covered with Parafilm®, and placed in a stationary temperature-controlled cuvette holder to maintain constant temperature of 37°C and allowed to grow overnight. The culture was gently poured out of the cuvette; the top of the cuvette was gently dabbed on a paper towel and then placed into the UV/Vis for the time drive experiment. Data was collected at 1451 nm for 15 sec intervals over various durations of time.

P. aeruginosa (PAO1) sample preparation for developmental stage synchronized experiment (Figure 2-11) was as follows. PAO1 was retrieved from -80 ºC stock and cultured in LB medium overnight at 37 ºC with shaking at 250 rpm. The cultured PAO1 gave an optical density close to 1 (OD600 =1.05), and was sub-cultured by adding 250 µL of overnight culture to 25 mL of fresh LB medium and shaken at 250 rpm and 37 ºC for additional 2 hr to obtain an OD600 close to 0.1 (OD600 = 0.11) of the bacteria. Multiple aliquots of 1 mL of the sub-cultured PAO1 (initial OD600= 0.11) were further cultured in disposable polystyrene cuvettes (see above for cuvette specification). The cuvettes were covered with Parafilm® (to prevent evaporation) and placed stationary in an incubator at 37 ºC for 24 h, before use. At the desired hour, the LB medium was removed, and the interior of the cuvette was rinsed 2 times with 1X

PBS. An additional ~0.1 mL of 1X PBS was added to the emptied cuvette (with biofilm on the wall) and immediately covered with Parafilm® to prevent evaporation of water from the biofilm.

For microscopy experiments a flat section of a broken cuvette of either material was placed into a cuvette in which a bacterial population was being cultured. After the designated procedure to produce a film was completed e.g. a specified time point is reached the flat section was placed on a thin steel plate that forms the base of a space within which the film could be studied. A compartment was created by a middle microscope slide acting as a spacer for another slide on top of that. The top slide was tightly secured to the bottom metal sheet, with the spacer in between, using metal clasps. The metal base provided a convenient surface to use for focusing and depth reference. The middle microscope slide comprised a rectangular annulus with a center section cut out to form the closed space within which the film could be studied. The outer seams were sealed with grease and some PBS could be introduced into the space to stabilize the film to drying without being in direct contact with the film.

Raman measurements were made using a Renishaw InVia confocal Raman microscope with 5x, 25x, 50x, and 100x magnifying objectives. The instrument has 532 nm and 785 nm lasers, and operates in reflection mode. The fluorescence microscope instrument was an LSM 710 by Carl Zeiss.

2.2.2. Fringe Analysis

Consider a layer of film (f) with a porous material (a) on one side and substrate (s) (thick quartz or polystyrene) on the other, and light incident normally from the air side. Interference occurs between light passing straight through the film and light reflected at the film-quartz and film-air interfaces.[57] Because the reflection coefficients are small, only the light reflected once at each interface is considered. The ratio of its electric field to that of the straight-through light is equal to

$$B = \frac{|n_f - n_a|\,|n_f - n_s|}{|n_f + n_a|\,|n_f + n_s|} \qquad [2\text{-}1]$$

which, for $n_a = 1$ and $n_s = 1.5$, never exceeds 1%. Thus interference between the two beams produces a sine wave whose electric field is B times that of the straight-through light, so the intensity of the fringe pattern (peak to trough) is $[(1+B)/(1-B)]^2$ times that of the straight-through light.[57] For B small, this factor is approximately 1+4B. Since absorbance A, which is measured, is defined as $\log_{10}(I_0/I)$, where I is intensity, the difference in absorbance, maximum minus minimum, is

$$\Delta A = \ln(1+4B)/\ln(10) \approx 4B/2.303 \qquad [2\text{-}2]$$

or 1.737B. Given measured ΔA one can obtain B, from which the refractive index of the film may be calculated using Equation [2-1], which is a quadratic equation for n_f.

The condition for constructive interference for a film of constant optical thickness ($n_f d$) in normal incident, incoherent light is[58]

$$2n_f d = (m+½)\lambda \quad m = 0, 1, 2 \ldots \qquad [2\text{-}3]$$

where the ½ comes from a phase shift accompanying one reflection. This condition allows interpretation of interference fringes observed in two different kinds of experiments.

Note that an absorption spectrum is measured through both sides of a cuvette so, unless one film is removed, the spectrum represents two films simultaneously. Equations [2-1] and [2-2] show that the same pattern is obtained for both films and, since B is small, the interference pattern should be just the sum of those for individual films. An experiment in which a fringe pattern was measured on a film-lined cuvette, and then re-measured after the biofilm on one side of the cuvette was removed, confirmed this expectation.

It was also noted that, for a set of 10 films produced simultaneously on different cuvettes under identical conditions/materials, the thickness varied by a standard deviation of about 10-

15% as indicated by the observed fringes after the first rinse of the native films. To check the effect of stirring, experiments were conducted involving light directed in both perpendicular directions and with removal of opposing films; they showed that the thickness of simultaneously produced films on all four sides were within ~1-2%. Thus the thicknesses given as results below correspond to the analog average of the two films on opposing sides of the cuvette.

2.2.3. Procedures and Data Analysis

Equation [2-3] suggests two kinds of measurements, both of which are given in this paper. First, one can monitor the apparent absorption at a single wavelength λ as the film dries or changes in some other way so that the optical thickness $n_f d$ changes. Results of this kind are shown in Figure 2-4. The absorption shows 1) a series of sinusoidal oscillations with maxima occurring when the thickness of the film satisfies Equation [2-3]. Each time a full oscillation is completed, i.e. for every 2π change in phase, the film has changed optical thickness by $\lambda/2$. Thus by counting the fringes (maxima) as the thickness reduces due to e.g. drying the original thickness can be calculated. We assume the index of refraction remains constant in this and the next experiment, and that the film has uniform and constant transverse extent in the region probed by the light used to measure the spectrum.

Second, one can measure absorption as a function of wavelength, as in Figure 2-6, and find the positions of a set of consecutive absorption maxima. Fitting those to Equation [2-3] allows a direct calculation of nd, the optical thickness of a film, assuming that the thickness does not change during the measurement of a spectrum (~7-8 min). A fractional error of less than 1 percent in peak position and the calculated value of nd is typical due to an error of several tens of nanometers for optical thicknesses that are typically in the 2,000-5,000 nanometer range. The physical thickness d and the index of refraction n_f cannot be calculated separately using just the positions of the maxima. They could be calculated from measurements at two different angles of incidence.[61-63] This would be subject to complicating effects of finite substrate thickness that do not exist for normal incidence. More practical is the use of Equation [2-1], which is a quadratic equation for n_f, given ΔA, n_a and n_g (see Figure 2-2). One can also calculate n_a from ΔA if the value of n_f is known.

2.3. Results

Figure 2-1 shows ΔA (= 1.737B) as a function of the layer index of refraction n_f, assuming a) that the layer is between porous and relatively dry alginate (n_a assumed for the sake of illustration to be 1.2) and solid substrate (n_s = 1.46 for quartz or 1.57 for polystyrene)[64, 65], and b) that n_f is between n_a and n_s. (The n_a for dry alginate is about midway between the indices of refraction of wet alginate[66-69], 1.334, and air, 1.00) We assume dry alginate because the dry layer has a smaller volume fraction of water than the layer in which interference occurs. Using a different value for n_a changes the minimum possible value of the film index (for this illustration) but does not change the qualtitative analysis. With this set of assumptions it appears that ΔA cannot exceed 0.004 for a quartz substrate or 0.008 for a polystyrene substrate for any reasonable value of the interfering film index of refraction.

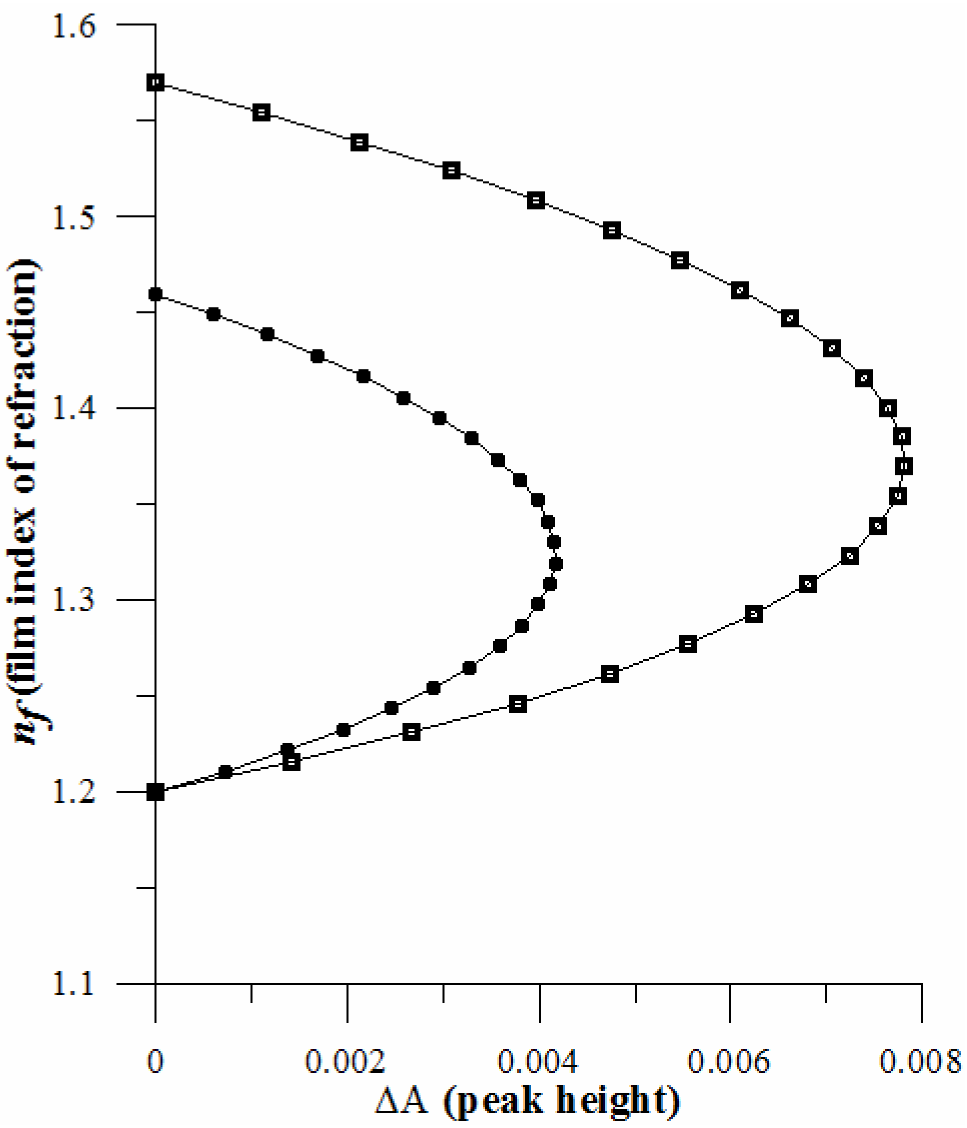

Figure 2-1. Index of refraction of film n_f as a function of fringe amplitude, as calculated from Equation [2-3] (since 3 is a quadratic, there are two roots). Solid circles are for quartz substrate, squares for polystyrene substrate. Index of refraction of alginate n_a = 1.334, index of refraction of substrate = 1.46 for quartz or 1.57 for polystyrene.

Figure 2-2 shows raw spectral data (with cuvette background subtracted) for a film produced by EC on a quartz substrate, after various treatments. (These four spectra correspond to the 1st, 3rd, 8th and 11th points in the time series shown in Figure 2-7.) Because the films reduce the net reflection loss at each of the internal cuvette surfaces, the baseline subtraction of the dry cuvette leaves the difference spectrum in slightly negative absorbance in the far UV and other parts of the spectrum. However, the actual absorbance at e.g. 1451 nm will always be referenced to the absorbance at 1310 nm i.e. we report A_{1451}-A_{1310}. The effects of lamp, grating and detector changes needed to span the whole spectral range can be easily seen.

Fringes are visible in all four traces (upper inset of Figure 2-2). Evidently, some types of structure that support optical interference forms spontaneously when a biofilm is removed from its birthplace and is allowed to drain by gravity. Note that the fringes can be analyzed for optical thickness regardless of the artifacts mentioned above because only their positions i.e. wavelengths are important. Also, the calculation of B in Equation [2-2] requires the change of absorbance across fringes, so the absorbance differences between a few fringe maxima and adjacent fringe minima can be used to calculate the index of refraction without correcting for these artifacts.

The absorbance near 3000 nm of the native film and that of the same film after a PBS rinse always exceed the dynamic range of the instrument (OD 10.00) but, after a DPBS rinse and a subsequent PBS wash, the film can be accommodated since the absorbance is reduced to about OD 2.75. The explanation is the H-to-D isotope shift accompanying D_2O exchange, which also explains the well-known[70] loss in absorbance of the 1451 nm feature. The loss here is essentially total. The lower inset shows that the 1451 nm feature is shifted to 1988 nm and the 2608 nm feature is shifted to 1932 nm. In both cases the ratio of vibrational frequencies is about 1.36 which compares well with the expected value of ≈ 1.41. Despite rinsing the small feature between about 220 nm and 300 nm is associated with protein and nucleic acids, is always visible, although reduced in intensity by the rinsing.[71, 72]

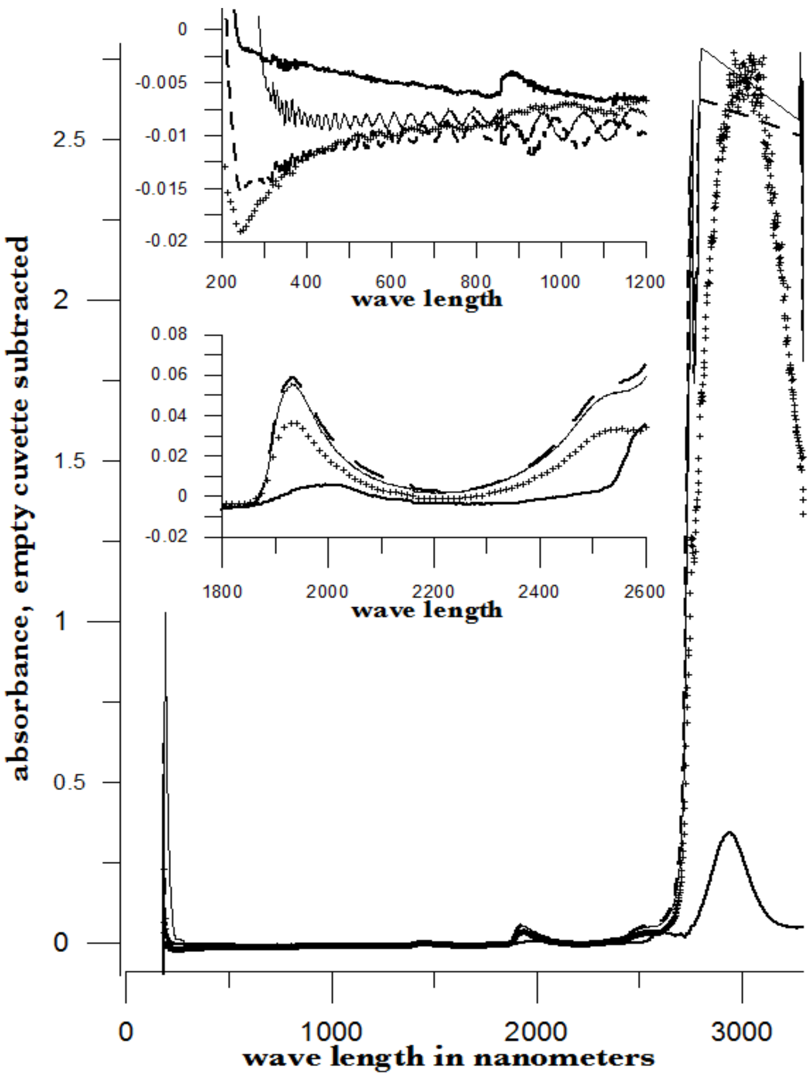

Figure 2-2. Typical raw spectra of (a) native film (thin solid line), (b) the same film subsequently rinsed with PBS (dashed line), (c) after a subsequent rinse with deuterated-PBS (heavy solid line) and (d) after a final PBS rinse (+ signs).

The fringe patterns can be analyzed to obtain the optical thickness by fitting the peak frequencies to Equation [2-3]. Considering Figure 2-2, we examined the first trace (native film) and worked with the 24 peaks with wavelengths from 381 nm through 1167 nm. To obtain the best fit to Equation [2-3], we calculated wavelengths according to 2T/(*m*+½) as functions of two parameters: the optical thickness T = *nd* and the value of *m* for the peak at 321 nm (*m* was decreased by 1 for each subsequent peak). We then calculated the squared deviations between measured and calculated wavelengths and minimized the sum of the squared deviations with respect to the two parameters. The resulting values were n_{321} = 31 and T = 5016 nm, with the sum of squared deviations 211. For the “rinsed film” the same analysis yielded n_{321} = 28 and T = 4593 nm, with the sum of squared deviations 1700. A plot of calculated wavelength vs. measured wavelength for this data is shown in Figure 2-3.

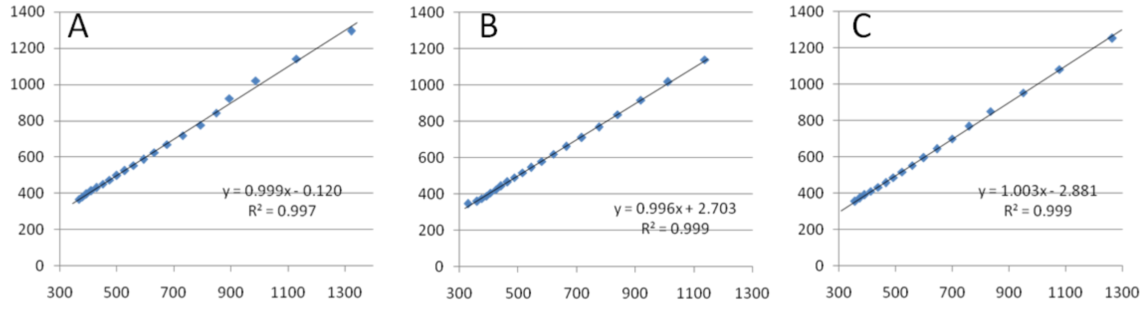

Figure 2-3. Calculated peak position is plotted against measured peak position for the three films, A) Native film with no rinses, B) Film after first rinse and C) Film after 2 rinses.

Figure 2-4 shows the second type of experiment: absorbance at 1451 nm was measured as a function of time. Measurements were made every 15 sec for the four combinations of substrate and organism: quartz or polystyrene with EC or PAO1. All four display a drop in absorbance over several hours, and all display fringes. Water is physically lost, first to draining across the surface of a fully hydrated biofilm and later by evaporation. The gravity-induced advancement of the boundary of the surface fluid (draining) produces an apparent small absorption loss. Observation of fringes requires that the index of refraction be relatively constant throughout the layer and, in the case of the spectral data, the thickness must not change much during the time of the measurement i.e. 7 minutes per spectral scan. The single-wavelength drying experiments in Figure 2-4 show the film thickness and water content change by only a few percent on that time scale. Furthermore, the spectral fringe data and the timed fringe data yield consistent thickness results (data not shown here).

Fringes are observed later, when the interfering subsurface layer becomes thinner (a peak is observed each time the condition for constructive interference, Equation [2-3], is satisfied). Thus, the time between consecutive peaks is the time to decrease the thickness of the layer by one wavelength of light. If all peaks are observed, the original value of *nd* is the number of maxima multiplied by 0.725 µm. In the lowest plot (EC on polystyrene) 7 fringes are observed, indicating an optical thickness of at least 7µm. In the second lowest (EC on quartz), 17 fringes were observed, so the thickness is at least 12 µm.

After the absorptions of the films approach a minimum, the EC and the PA01 films behave somewhat differently. In the EC films fringes no longer appear and the absorption begins a smooth rise with high-frequency noise superimposed. This marks the beginning of the films' cracking, as direct visual observation reveals. Cracking apparently occurs in EC films after 2000 seconds for polystyrene and 3100 seconds for quartz. Cracking does not appear to begin in PAO1 films until an additional several thousand seconds has elapsed. The EC films also begin to display very small amplitude fringes corresponding to formation of uniform films several multiples of 1451 nm thick once the interfering layer is completely gone. The amplitude of these fringes is at most 10% of that of the early-time fringes.

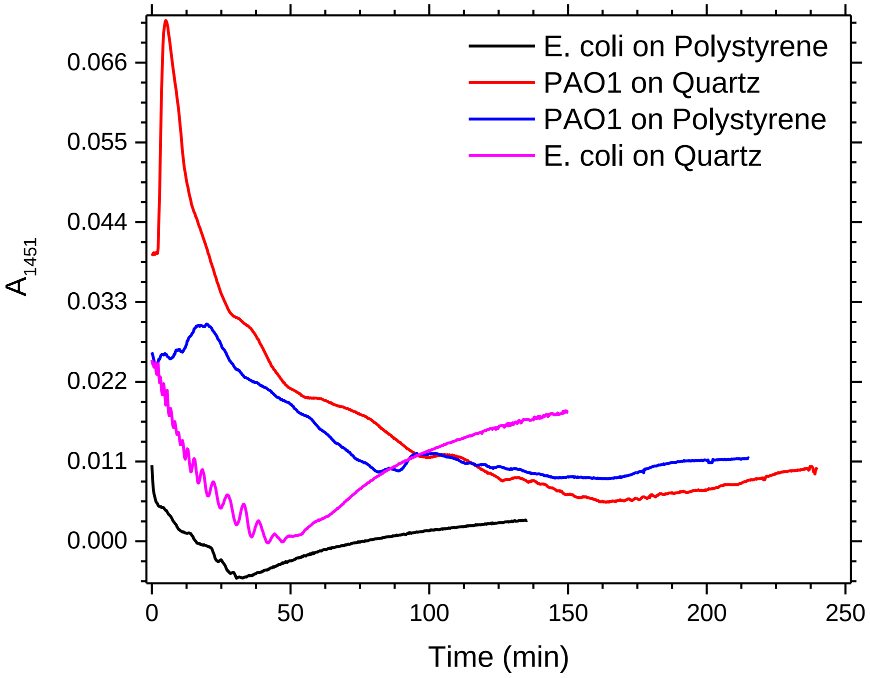

Figure 2-4. Absorbance at 1451 nm vs. time for EC or PAO1 on quartz or polystyrene substrates. Readings were taken every 15 seconds. Note[58] the peak at 1451 nm is due to water in the film. Fringes are evident in each of the four traces. The apparent absorbance always rises after reaching a minimum and, eventually, very small spikes in the absorbance vs. time plot appear with $\Delta A \approx 1 \times 10^{-3}$ Absorbance units, showing film cracking.

For some of the films, there were no fringes, even though the A_{1451} was substantial, and this will be discussed below. In Figure 2-5, A_{1451} is plotted against the optical thickness for all films for which both could be measured. The trend line is shown; the slope is $(2.9 \pm 0.2) \times 10^{-6}$ Absorbance units/nanometer. These films involve three different organisms, two different substrates, and both LB and minimal media. The data also includes several results for a single film during hydration and dehydration treatments like those shown in Figure 2-6. The trend line is for all films although the EC film and PA01 films appear to contain a different amount of water per unit thickness. Since the relative error is only 7%, it is clear that, in general, considering all bacteria, substrates, and experimental conditions, A_{1451} is proportional to the optical thickness *nd*.

Since the water content is proportional to film thickness, the range of hydration level for any particular thickness must be small. The apparent water content per unit thickness is about the same regardless of 1) the species of organism 2) the culture medium used or 3) the choice of substrate. That is, a single film at various levels of hydration fits into this graph with many other films at varying levels of hydration.

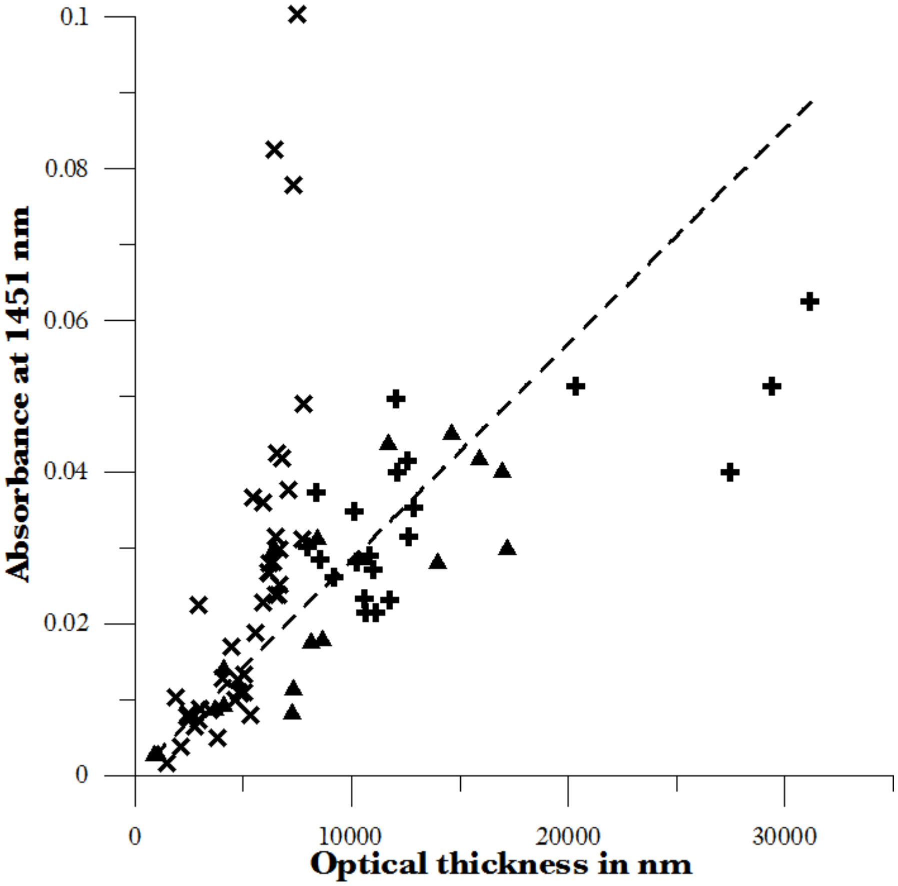

Figure 2-5. Absorbance at 1451 nm is plotted against optical thickness (from fringes) for all films for which both can be measured. × = EC films on quartz, + = PAO1 films on polystyrene, ▲ = PAO1 films on quartz. Dashed line is best-fit line through origin, showing overall trend.

The effect of successive PBS rinses for the same film (EC on quartz) is shown in Figure 2-6. These spectra correspond to the third, fourth, and fifth points in Figure 2-7, except that in Figure 2-7 one of the rinses was with DPBS. All the spectra show interference fringes. Referring to Figure 2-2, we note that there are two possible roots for the index of refraction of the layer for a given ΔA even assuming a value for n_a. We note that the interfering layers contain significant water, which has an index of 1.34, and ΔA *decreases* as the film dries. Therefore we choose the higher root for n_f and conclude that n_f is closer to n_s than to n_a.

Shown in Figure 2-5, the PAO1 films always have more water than the EC films and also that the quartz substrate films always have more water than the polystyrene substrate films. It is clear that the fringe spacing and the absorbance at 1451 nm are essentially unchanged by subsequent rinses after the first rinse. From the analysis of the fringe spacing, the optical thickness is 4848, 4730, and 3984 nm for the three spectra, i.e. 4521 ± 469 nm. Thus, the rinse-and-dry cycling does not affect the film’s ability to retain water. Measurements show that the 1451 nm absorbance intensity changes in unison with the thickness, as was noted in the presentation of Figure 2-5.

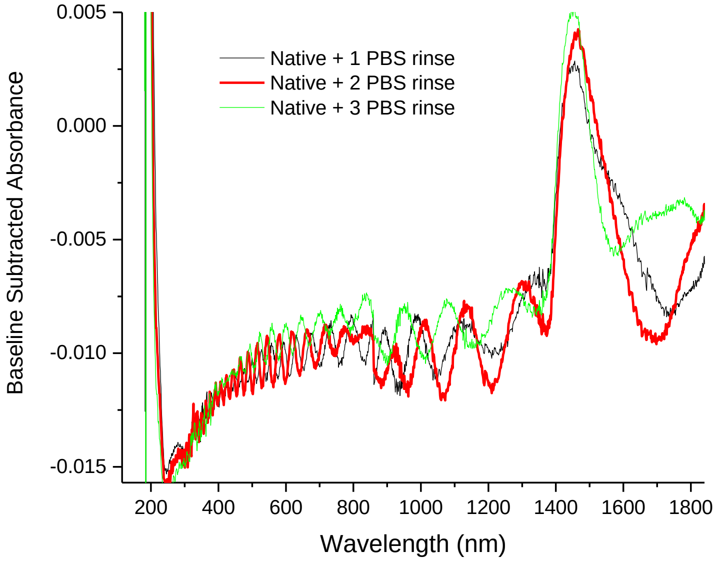

Figure 2-6. Absorption spectra for a single film (EC on quartz) after successive rinses with PBS. The spectra correspond to the 3rd, 4th and 5th points in Figure 2-7. The average optical thickness is 4521 ± 469 nm for the three measurements. The 1451 nm absorbance intensity changes in unison with the thickness, as shown in Figure 2-5.

Figure 2-7 shows, for a film (EC on quartz) undergoing successive drying and rehydration cycles, the optical thickness calculated from the fringe positions along with the corresponding absorbance at the 1451 nm water peak. These spectra were chosen as typical behavior from many obtained to illustrate the effects of hydration, drying and deuteration which form the basis for Figures 2-3 through 2-7. Figure 2-7 shows that the absorption at 1451nm and the optical thickness calculated from the fringes vary together. The successive treatments result in films being thinned by nearly a factor of two before being rehydrated and swelled using PBS to nearly the same initial thickness, while retaining sufficient surface smoothness and internal homogeneity to form fringes. There is apparently a limit to how much water can be retained after draining since the interfering layer is never thicker than about 15μm regardless of the total thickness of the biofilm i.e. how much carbohydrate material is present.

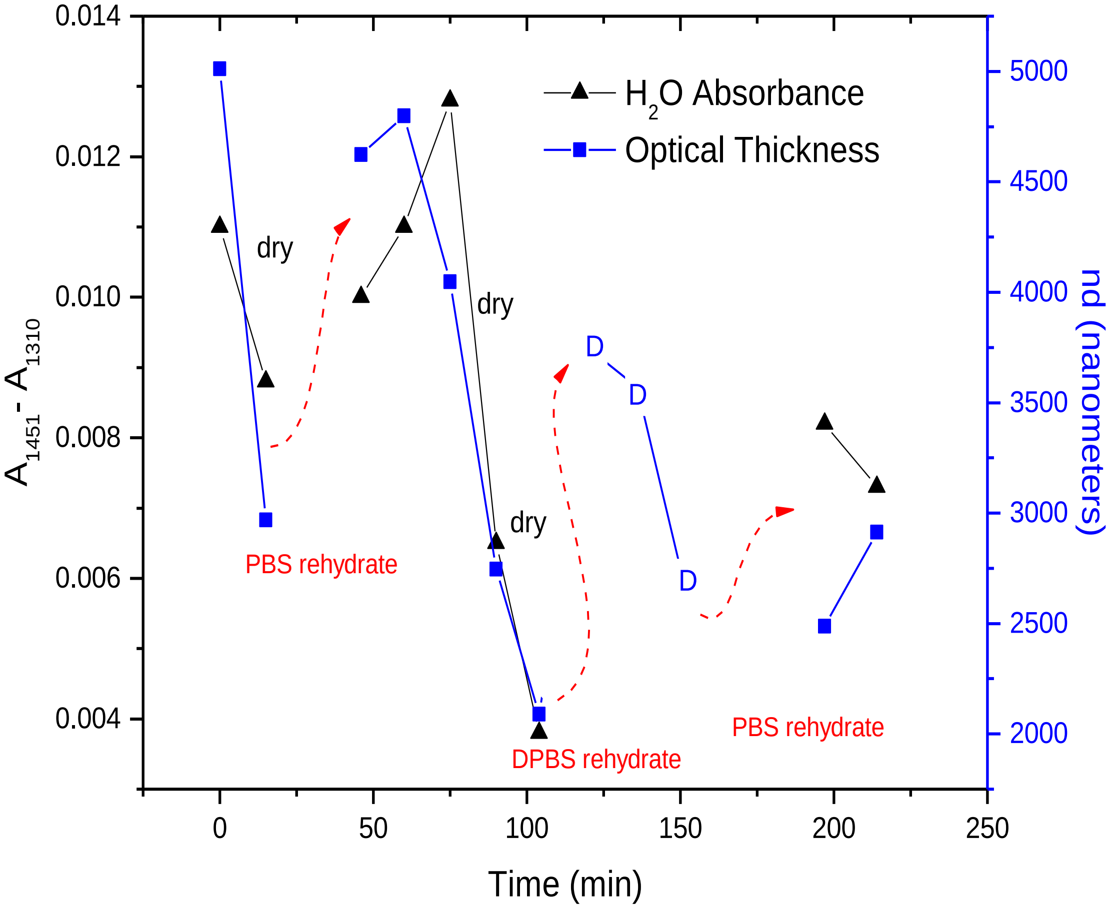

Figure 2-7. Absorbance (▲), optical thickness calculated from fringes (■) and rinse with DPBS (D) for a single film (EC on quartz) undergoing successive dryings and rehydration. "Dry" indicates that the film was air dried while the previous spectrum was being collected. Deuterium isotopic shift between 120 and 150 minutes did not have 1451 nm spectral features, therefore H_2O Abs not plotted. Two spectra, taken between 150 and 190 minutes, before rehydration with PBS, did not display fringes, so the points were not plotted. When the film was rehydrated with PBS fringes were again visible.

Figure 2-7 shows that a film rehydrated with PBS after hydration with DPBS and air drying, did not recover its full initial thickness, whereas films did when rinsed with only PBS. This could reflect the cumulative effect of all the previous rinses or the disruption of the hydrogen bonded network by deuteron exchange in a manner different from proton exchange.[73]

However, Figure 2-6 shows that three rehydration cycles with PBS did not diminish the capacity of the film to retain water or return to its full initial thickness. Thus, the deuteron exchange is more likely responsible for the decrease shown in Figure 2-7.

Information about the actual thickness of the entire biofilm is obtained from confocal optical measurements. Figure 2-8 shows the results of confocal fluorescence measurements (excitation wavelength of 480 nm) on a biofilm formed by PAO1-GFP on polystyrene for 24 hours at 37°C. The green fluorescence indicates the presence of bacteria. The panels show the series of fluorescence images for successive depths, passing through air, biofilm and then polystyrene. Each cross-section is approximately 760 μm by 760 μm. The difference in depth between successive images is 5 μm.

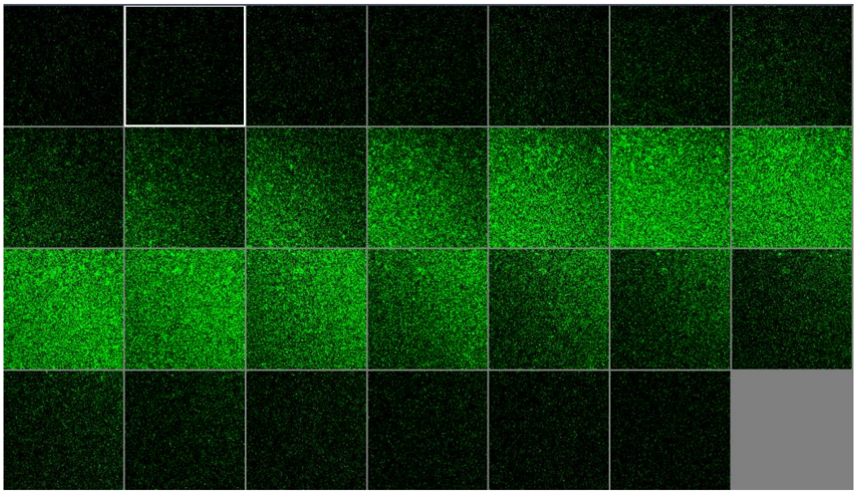

Figure 2-8. Confocal images with an excitation wavelength of 480 nm of PAO1-GFP biofilm formed on polystyrene surface over 24 hr at 37°C. The confocal planes are for stepwise penetration of the biofilm, with spacing between successive planes of 5μm.

From left to right starting in the upper left corner, the first 8 images show no fluorescence above background, the 9th shows weak (relative to the succeeding images) fluorescence, the next

8 show maximum fluorescence (all about the same), the 2 following show progressively decreasing fluorescence intensity, and the remaining 8 show no fluorescence above background. Therefore, bacteria are present in the 9th through the 19th images, corresponding to a total thickness of about 50 μm or $5x10^4$ nm. By curve-fitting the fluorescence intensities we obtain a somewhat smaller thickness, 44 μm.

This is about one order of magnitude larger than the thickness of the water-rich layer as measured by thin-film interference fringes. The thickness of the bacteria-containing layer in other films, as measured by confocal fluorescence, was as high as several hundred μm. Still, the thickness of the water layer for these films is never larger than 15 μm. Note that the thickness of the water layer is determined by how much water is retained in the films after the initial draining and some evaporation of surface fluid. The thickness measured by the confocal fluorescence measurement is the thickness of the bacteria-containing layer in the original film.

A third thickness may be obtained by confocal Raman measurements. Figure 2-9 shows a Raman spectrum obtained using a 532 nm excitation confocal Raman microscope of a wet biofilm (PAO1 on polystyrene), and also a Raman spectrum of dip coated film using commercial sodium alginate on polystyrene. Both PAO1 and sodium alginate have multiple features in common. The relatively weak features between 1300 cm^{-1} and 2100 cm^{-1}, both sharp and broad, coincide with polystyrene features. Although the relative intensities are not the same, both of the spectra contain a sharp feature[74] near 2950 cm^{-1}. A strong feature with a broad base peaks[73] near 1090 cm^{-1} exhibits the same behavior in depth profiles as the 2490 cm^{-1} feature. Microscopic images of films in a range of hydration states reveal a variety of surface textures. The Raman spectrum of the sodium alginate polymer film suggests that biofilm is also a polysaccharide.

The amount of biofilm material in a spatial region must be estimated (on a relative scale) from the intensity of the Raman peaks. In the confocal Raman measurements, the spatial regions are horizontal slices through the film at heights separated by 40 μm. As for the fluorescence measurements (Figure 2-8), not all locations at a particular height show the same intensity. This is consistent with the inhomogeneous nature of these films, and explains the scatter in the points in Figure 2-10.

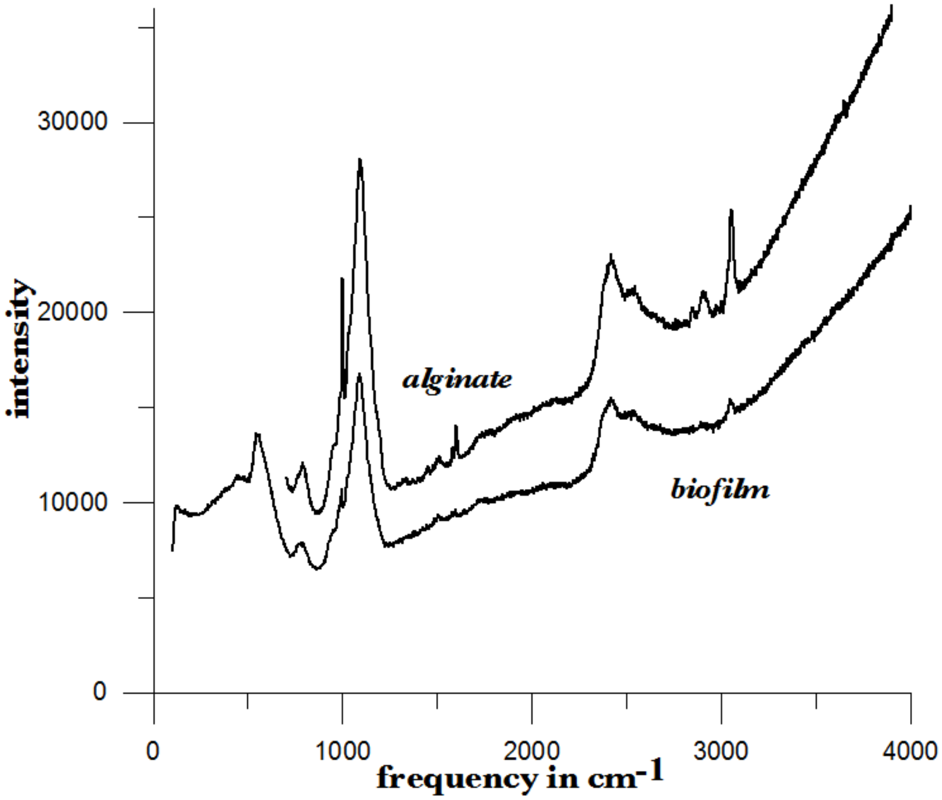

Figure 2-9. 532 nm excitation Raman spectrum of PAO1 biofilm and authentic alginate film on polystyrene substrate.

Figure 2-10 shows two depth profiles obtained by confocal Raman measurements (532 nm excitation, 2400 cm^{-1} Raman feature) on two biofilms, both PAO1 on polystyrene. One profile was obtained by starting at the air-film interface and probing successively deeper until Raman features of the substrate were observed; the other profile was obtained by going in the opposite direction i.e. from the substrate-film interface outward to the air-film interface. Relative intensity, or concentration of biofilm material, is plotted for successive heights, from 70 to 690 µm in steps of 40µm (20 points). The dashed lines are quartic fits, inserted for emphasis. In the upper plot, it is evident that the biofilm layer is about 750 µm thick, whereas the lower plot shows a thickness of about 850 µm. For these films, the thickness of the layer containing bacteria, from confocal fluorescence measurements, is about 300 µm. Thus, the bacteria are concentrated in a sublayer of thickness about half that of the complete biofilm. One cannot determine from these measurements whether this sublayer is at the top, bottom, or middle of the alginate layer.

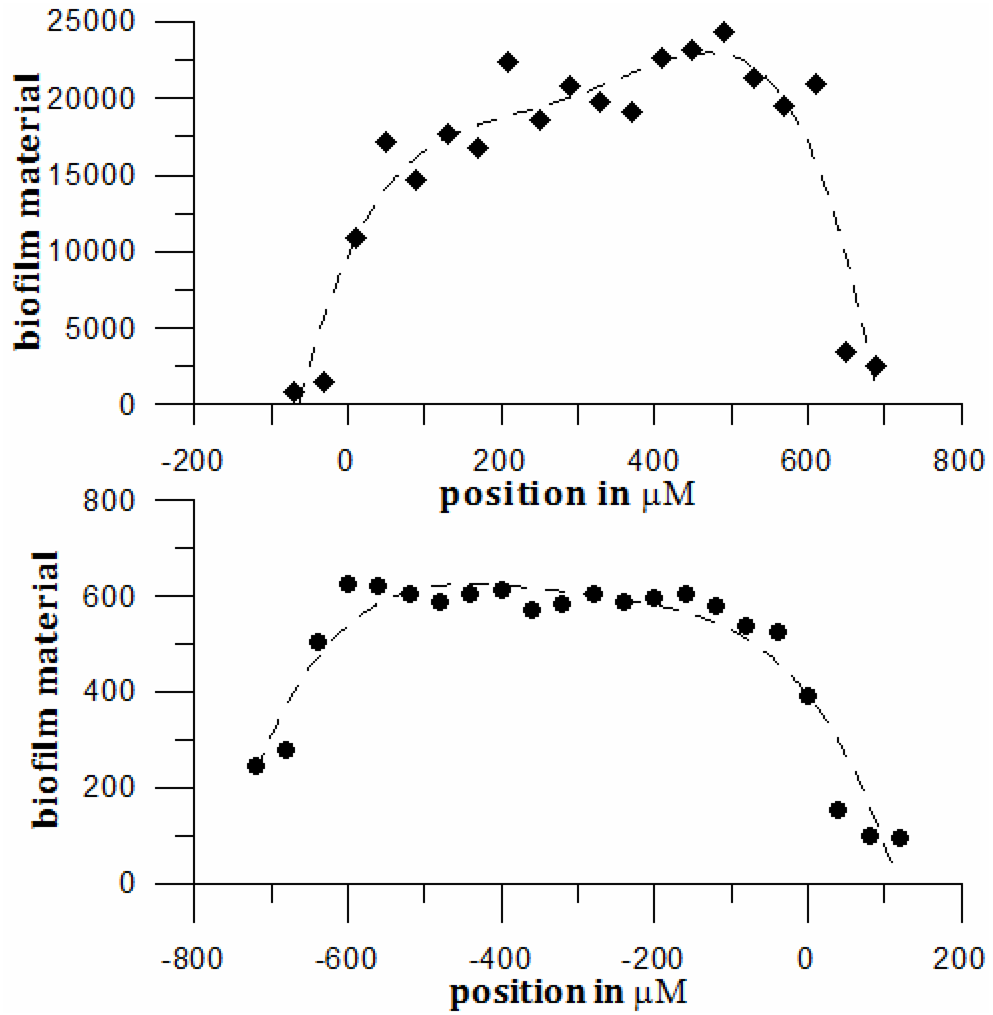

Figure 2-10. Depth profiles for two PAO1 on polystyrene biofilms, showing 2400 cm^{-1} Raman counts (alginate) at various heights. Separation between successive heights is 40 μm. Dashed lines are quartic fits, inserted for clarity.

Additional experiments were conducted to relate the properties of the films, such as the propensity to form an interfering layer, to the stage of bacterial life cycle during which the biofilms were produced. In these experiments, six cultures were initiated simultaneously and grown in parallel and the films produced by these identical cultures were assessed, after various incubation times, for fringes and 1451 nm absorption. The results are shown in Figure 2-11. One sample for the 550-minute incubation was lost inadvertently.

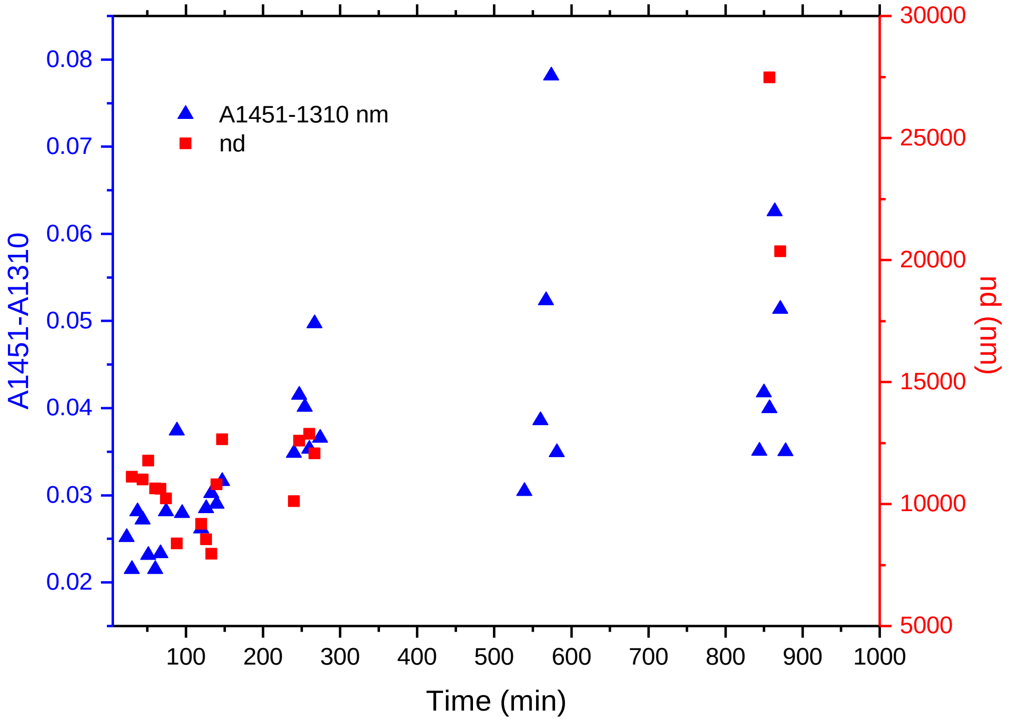

Figure 2-11. Results of measurement of 1451 nm absorbance (▲) and film thickness (■) for identical films produced in parallel for various formation times. The absorbance measurement is always possible but not all films produce interference fringes for thickness measurement.

The first observation one can make from Figure 2-11 concerns the scatter in the points for larger times. The root-mean-square deviation in A_{1451} or in nd is almost as large as the mean, and much larger than the experimental error. This large variation (much larger than the variation in other sets of supposedly identical films) explains some of the scatter in the data of Figure 2-5, and makes it important to always carry out several different measurements on the same and multiple films. Another observation is that both A_{1451} and nd increase with formation time, which is of course to be expected since the film is being built up. The results in Figure 2-11 also confirm that A_{1451} and nd increase together.

More interesting is the observation that many films do not display interference fringes. Nearly all the films for the smallest incubation times, which are produced during the “lag phase”, display fringes. These are relatively thin films and have correspondingly small 1451 nm absorptions. For films with incubation times between 500 and 600 minutes, corresponding to the “exponential” or stationary growth phase, no fringes are observed, although the water absorption shows that water is present, in amounts greater than that found in the films produced during the lag phase. However, for these films, the strength of the water absorption varies wildly. For even longer incubation times, extending to the late stationary or “death” phase, we observe fringes in some, but not all, the films. Films showing substantial A_{1451} but no fringes clearly contain water, but, if a layer exists, it does not satisfy one or more of the criteria for displaying fringes.

2.4. Discussion

Donlan[56] defines a biofilm as an “assemblage of microbial cells that is irreversibly associated with a surface…” Since much of the practical interest in biofilms lies in undermining the advantages bacteria derive from them, presented in this paper are optical and spectroscopic measurements showing the behavior of biofilms, grown on either a quartz (hydrophilic) or polystyrene (hydrophobic) substrate, following draining and gentle rinsing, and while drying. Presented here are results on two different bacteria, two different substrates, and one culture medium. Varied film development time, synchronized with the developmental stages of the cultures, as well as stirring, rinsing and drying conditions.

A layer that exhibits optical fringes from the UV to the NIR forms in most of the biofilms studied, after draining the films to remove some liquid. This layer can remain stable for minutes and hours. Its thickness, calculated unambiguously from the fringe spacing, is correlated with the strength of the water-associated NIR absorption at 1451 nm, isotopic shifts and the literature[60, 70] clearly assign the observed NIR absorption features. The physical interpretation of these fringes, and the conditions necessary for their observation, have been summarized.

The bulk of the material comprising the biofilm is polymeric carbohydrate having a Raman spectrum much like alginate. The thickness of this material, and the physical thickness of the region holding the bacteria in the film, are always much greater than the physical thickness of the interfering layer (which is unambiguously obtained from the wavelengths of the interference fringes). This must be the case if the interfering layer was contained within the carbohydrate matrix, supporting the picture depicted in Figure 2-12.

The new observation presented in this work is that most of the biofilms examined exhibit interference fringes after removal of the growth medium; to our knowledge this has not been reported before. The formation of biofilms at interfaces (liquid-gas, solid-gas etc.) is well documented[75-77] so that the biofilm structure and behavior observed here is relevant to these situations. Since biofilms are often found at locations associated with transient wetting and drying, as in a liquid-gas interface, the “hydrology” examined in this paper is relevant to the environment bacteria experience at the phase boundaries encountered in nature.

The primary concern in this paper was with the relationship between the fully hydrated native biofilm that is formed in the culture medium and the hydrated interfering layer that forms in the biofilm after removal from the culture medium. The interfering layer is probably bounded by the substrate on one side and dehydrated alginate on the other for reasons presented below. The dehydrated layer-interfering layer interface is within the carbohydrate material as represented in Figure 2-12. This suggests that understanding the properties of the hydrated interfering layer may be relevant to understanding the biology of biofilms.

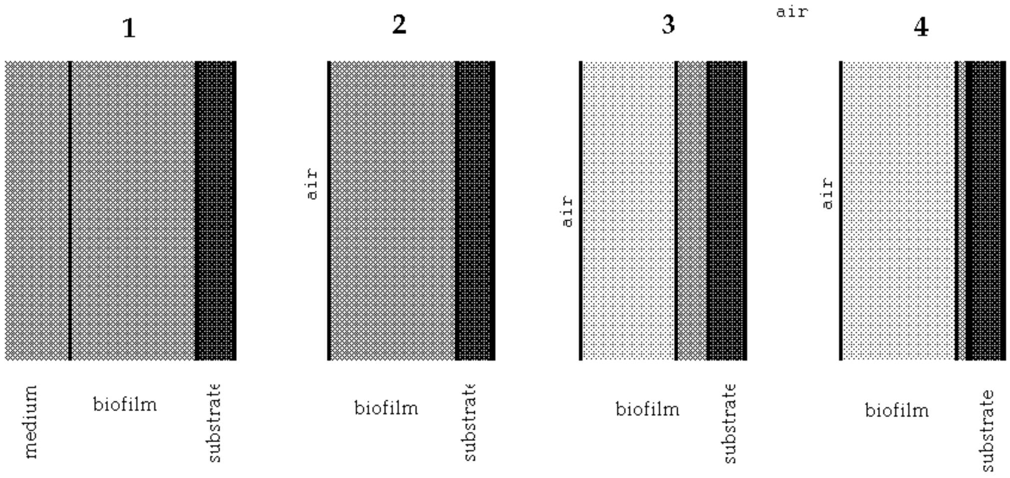

Figure 2-12. Schematic diagram showing structure of biofilm at various stages. 1: Biofilm in contact with growth medium on left and substrate on right. 2: Biofilm after removal of medium and draining of surface fluid, before evaporation of interior fluid. 3: Biofilm after some of residual interior liquid has condensed into a water-rich layer adjacent to substrate (darker color). The remainder of the film is dryer than the layer (lighter color). 4: Biofilm after air drying, which thins the water-rich layer. Thicknesses are not to scale.

Measurements on films produced by various bacterial species, with various growth conditions, substrates, hydration states and other parameters that could affect the properties of the films, show that the ability to produce an interfering hydrated layer is widespread. This tendency is ubiquitous and is a physical and chemical consequence of the biofilm composition (polymeric carbohydrate and water) rather than being biological in origin. It is possible to observe the formation of such layers in alginate films produced in the lab without bacteria, as will be reported in detail in a separate publication. Note that materials exuded by the bacteria into the medium can modify the medium and the biofilm in contact with the medium, and this modification can serve the purposes of the film's residents i.e. the bacterial culture.[71, 78-81]

There is apparently a limit to how thick the interfering layer can be. The thickness, as obtained by analysis of the interference fringes, is never more than about 15μm regardless of the total thickness of the biofilm. Also, the thickness of the layer containing bacteria, from confocal fluorescence measurements, is about half that of the total film thickness from confocal Raman spectroscopy, which shows the location of alginate. This shows that, in the late stage of film construction, the bacteria are not found everywhere, but are concentrated in a layer about half as thick as the biofilm. It is not clear from our observations if there is a preference for where within the film the organisms might be found e.g. whether nearer the substrate, or nearer the film-air interface.

Note that PAO1 films always retain more water than the EC films, and also that the quartz-substrate films always retain more water than the polystyrene-substrate films. Possibly this is associated with the more hydrophilic nature of quartz vs. polystyrene and the materials exuded by the PAO1 organisms into the fluid medium vs. those exuded by EC.[71, 82, 83] The index of refraction of either substrate is quite different from that of the hydrated layer as determined from our data i.e. 1.3343[65, 67] and so we expect that there will be adhesion of the bacteria to either substrate if they come close. Perhaps the bacteria can sense the presence of the substrate by the presence of the hydrated layer.

A possible mechanism for formation of the layer that gives interference fringes is shown in Figure 2-12. Stage 1 is after the bacteria secrete an alginate or alginate-like polymeric material which forms the bulk of the biofilm and plates out onto all contacted surfaces.[71, 75, 84, 85] This is a strongly hydrogen bonding material, like all polysaccharides in aqueous media, due to the presence of multiple hydroxyl groups on each monomer, and is infinitely miscible with water.[71, 75, 79] When the film is drained, bulk liquid medium is removed by gravity and evaporation, until only a thin coating exists on the surface of the alginate and some medium remains in the interior**.** After the surface water is gone (Stage 2), the presence of water in the interior is shown by the absorption at 1451 nm (A_{1451}). At this point the region closest to the air is losing water to evaporation and the water left in the interior is in the form of small droplets or perhaps individual water molecules. This water is distributed throughout the interior of the film, in channels or spaces in the carbohydrate framework.[71, 86, 87] In this form the water cannot show interference fringes, since there is no layer.

Because of the extensive hydrogen bonding between water and the bulk carbohydrate in the film, we propose that the material in the interior does not begin to lose water until essentially all the surface water is gone. Subsequent to the loss of surface water, water molecules continue to leave the film by evaporation to the gas phase. Simultaneously, water molecules in the interior move in all directions until, because of surface tension, smaller droplets coalesce into larger ones, which are more stable. The movement may be by evaporation-condensation, diffusion on interior surfaces, or other mechanisms. Eventually, the larger coalesced droplets distort, because of the planarity of the biofilm and surface tension, into a layer which can show fringes. This is illustrated in Stage 3 in Figure 2-12.

Air drying removes water from the drained biofilm, which means mainly from the water-rich layer. It is likely that, because of hydrogen bonding, some water remains distributed over the internal surfaces of the film, and probably is difficult to remove without affecting the film's structure. As shown experimentally, the thickness of the water-rich layer decreases as the water content of the film decreases, with the index of refraction remaining constant. This is shown as Stage 4 in Figure 2-12.

Another explanation for formation of the thin, water-rich layer after draining of the film is based on the well-known fact that biofilms are not uniform. Zhang and Bishop[88] showed that from the top to the bottom of a biofilm, the porosity decreases by a factor of two and the mean pore size by a factor of five. Thus, movement of water in the lower layers (furthest from the free surface) is 1) much more difficult than movement of water in the upper layers and 2) confined to moving parallel to the substrate surface. The movement of fluid parallel to the substrate encourages the formation of a film with the same orientation. Water may remain in the lower layers after the upper layers have been depleted of water. Surface tension will further stabilize this situation and help create a smooth enough surface to allow interferences to be observed.

To estimate how much water must leave the hydrated biofilm before the stable interfering layer forms, we estimate the index of refraction of the relatively "dry" alginate side of the interface. Since ΔA for the fringes decreases as the film dries, the higher value is chosen for n_f in Figure 2-1. Thus, the index of refraction of the film is always closer to the index of refraction of the substrate than to that of dry alginate. With this information, the absorbance spectra can be used such as those in Figure 2-6 to calculate one index of refraction when two others are known, based on Equation [2-1].

Calculating ΔA near 600 nm must be done first by subtracting the average absorbance at two adjacent minima from the absorbance at the included maximum. The results for ΔA are 0.00170, 0.00194, and 0.00154 for the three interference patterns shown in Figure 2-6. The closeness of the three results (average 0.00173, standard deviation 0.00020) confirms our finding that a dried film can be fully rehydrated. Since these spectra were taken through a cuvette, so that the beam passes through two identical films, the actual ΔA for one film is half what one measures in the spectrum, i.e. 0.00086. The diffracting layer is hydrated alginate, with an index of refraction $n_f = 1.334$, and the substrate is quartz, with $n_s = 1.46$.[63] Solving Equation [2-1] with $B = \Delta A/1.737 = 0.00050$ gives $n_a = 1.30$. This "dry" alginate (the remainder of the biofilm when the water-rich layer has formed adjacent to the substrate) probably still contains some water. Since the index of refraction of air-filled void spaces is close to 1.00, one can calculate the void volume fraction v from $(1.00)v + 1.4(1 - v) = 1.30$, which gives $v = 36\%$.

The index of refraction remains relatively constant as the layer becomes thinner or thicker with drying or rehydration. For observable fringes, it is necessary that the index of refraction within the film differ from the indices of refraction of the phases bounding the film, presumably relatively dry but porous alginate (n_a between 1.00 and 1.334, the index for hydrated alginate)[65, 67] and solid substrate ($n_{\text{quartz}} = 1.46$, $n_{\text{polystyrene}} = 1.57$).[61, 63] Since spectroscopic and other evidence indicates that the film is essentially hydrated alginate, its index is close to 1.334, only slightly higher than n_{H_2O}.

Note that the classical index of refraction in a nonmagnetic material is the square root of the material dielectric constant using Maxwell's equation.[59, 89] Thus the dielectric environment of the hydrated carbohydrate film is virtually identical to that of water itself. When the film is removed from the liquid in which it is immersed, the organism-friendly environment inside a biofilm is preserved in the interfering water-rich layer, which has a dielectric constant similar to that of the hydrated film. Since the dielectric constant of a material governs its response i.e. the reorientation and redistribution of charge caused by an electric field, one can suggest that the surface charge distribution of bacteria[90, 91] is not perturbed when the bacteria traverse spatial regions with the same dielectric environment. Bacterial movement within and between the surrounding mostly aqueous liquid and the fully hydrated film is therefore facile and without physiological consequence.[71, 84, 86] If the surface charge density of bacteria interacts with the local environment it may cause adhesion and impeded motion of the bacteria through the medium.[92, 93]

The proportionality between A_{1451} and *nd* shows that the thickness of the layer producing fringes is proportional to the amount of water present, which reinforces the notion that the interfering layer is a hydrated alginate-like material. Furthermore, the hydration within the interfering layer is relatively unchanged during the drying/thinning process since 1) the index of refraction remains the same and 2) the hydrated films thin as they lose water.

The constant of proportionality between A_{1451} and *nd* may depend on the substrate, the bacteria, and the conditions of biofilm formation. For the three choices of bacteria and substrate shown in Figure 2-8, the slopes are 4.94×10^{-6}, 2.27×10^{-6}, and 2.51×10^{-6}; understanding the differences will require a more detailed future study. Considering results for individual films during treatments like those described in Figure 2-7, i.e. a single film at various levels of hydration, the proportionality is excellent. The same is true for many other films, with different values for other parameters, observed at varying levels of hydration. However, the apparent water content per unit thickness is roughly the same regardless of 1) the species of organism, 2) the culture medium used or 3) the choice of substrate.

When native PAO1 films on polystyrene showing an interfering water layer 10-15 μm thick were soaked in 5M NaCl for 30 minutes, they were found to be swelled by as much as 30%. Fringe analysis indicated that the hydrated layer in these films expanded by 30-50%. We note that the ability to draw fluid, i.e. salt water, as observed for these films, is known for alginate aerogels/hydrogels.[94] There is clearly much work to be done to understand the structure and function of these films. Rinsing experiments with various species such as divalent metals like Ca^{+2} might prove interesting given their potential role in conventional hydrogels as cross linkers.[95-97]

Since these films are able to sequester water and possibly also NaCl from relatively concentrated aqueous salt solutions, the exchange of protons for protons is facile and nondestructive. The exchange of protons for deuterons is also facile and partly reversible but possibly somewhat destructive of the film's internal structure.[73] This is apparent in Figure 2-7: films hydrated with PBS and then dried and rehydrated retain the same amount of water after draining, whereas films hydrated with DPBS before drying and rehydration with PBS retain significantly less.

The hydration/dehydration sequence, either by direct immersion in liquid/draining or vapor deposition/evaporation, may dilute the nonstructural components of the hydrated layer. Note that the first rinse of a native film with PBS always reduces the strength of the 180 nm and 240-260 nm absorptions, but that these features are never completely removed even after four PBS washing cycles. RNA, DNA and proteins are well known to absorb in these spectral regions.[70, 71, 85, 98, 99] Some of these materials and also smaller molecules can be redistributed by rinsing, and the biofilm matrix can protect some of them from being removed.[71]

A series of films was formed in parallel with identical cultures and under identical conditions, but sampled at different times of culture development. As shown in Figure 2-11, almost every film cultured for less than 300 minutes produced, when drained, a water layer showing interference fringes (17 films). The thickness of the layer was proportional to the water absorbance intensity A_{1451}, as is generally found to be true. From the fringe spacing, these are among the thinnest films produced, with a correspondingly small 1451 nm absorption. Strikingly, of the 10 films cultured for times between 500 and 700 minutes, none produced an interfering water layer, although A_{1451} was of the expected size. For culture times between 800 and 900 minutes, 2 of the 10 films produced an interfering water layer. Thus, when the bacteria are most active, during exponential growth and active reproduction, at least one of the criteria for forming an interfering layer is not satisfied. Furthermore, the film structures existing at these later times are highly variable in their capacity to sequester water as indicated by the large variability across films produced.

The absence of observable fringes implies that something prevents the water, which is certainly present after draining, from coalescing into a planar layer. This may be due to the structure of the biofilm: perhaps the internal pores are blocked, too narrow, or too tortuous to allow rearrangement of the water. It may also be due to the bacteria, which may block pores.[84, 86] Also, if organisms produce an extra-cellular matrix (ECM) with a chemical structure that produces large, internal, Swiss cheese-like voids, it might preclude the observation of optical interference. Other explanations are that films sampled during or after the growth phase contain more and larger channels and voids, due to the larger numbers of bacteria or their increased activity, that impede the formation of the water layer.[84, 86, 89, 90, 100, 101] Further study might lead to a method for assaying bacterial cultures with the ability to observe their activities at different stages of development.

In an open system the stability of the two-layer structure is extended by the slow rate of gas transport through the relatively dry outer material i.e. the Knudsen Effect.[102] At least some alginate films[67] dried using supercritical fluids to produce aerogels and hydrogels have been shown to have a porous structure with internal cavities smaller than the mean free path of air molecules. Because mass transport is slow, evaporation is slow, and since the entire carbohydrate layer can be hundreds of microns thick, at least some of the layer structure is maintained as water in the interfering layer evaporates, extending the lifetime of that layer. The materials the bacteria exude tends to produce this structure, which is able to sequester water, thus enhancing their survivability when water becomes scarce.[71, 83, 85, 97] All the evidence suggests that with respect to accommodating the needs of a bacterial culture, the interfering layer closely resembles the original hydrated immersed film. It thus may help to protect the culture, when the film faces dehydration, by providing a stable environment for the bacteria.

2.5. Conclusions

We have discovered that most biofilms produced before a particular culture's exponential growth phase, when removed from the aqueous growth medium and drained to remove bulk medium, spontaneously produce an internal two-layer structure. Under the same conditions films produced during the exponential growth phase, when the bacteria are expected to be most physically active tend to not spontaneously produce an internal two-layer structure. A thin layer having an index of refraction higher than that of dry porous alginate (the principal component of the biofilm) is formed from the water remaining after draining. This layer, which is adjacent to the solid substrate, displays optical interference across the UV-visible-NIR region, showing that it is of uniform optical thickness and constitutes a distinct separate phase with an index of refraction different from both the substrate and the relatively dry porous alginate. The optical thickness and the degree of hydration can be obtained unambiguously from the optical interference fringes, providing unique quantitative physical and chemical information on this hydrated layer. As the film dries by evaporation, the layer maintains properties, although the layer becomes thinner. Formation of the layer occurs with all organisms tested and various growing conditions and so may be more dependent on the chemical nature of alginate than on any process involving the bacteria. It functions as a separate phase, distinct from the remainder of the film which has the same carbohydrate matrix but with about 30-40% less water per unit volume than the interfering layer. We speculate that the environment in the interfering layer is similar to that of the original medium immersed alginate, suggesting that this layer provides a protective environment for bacteria when water is scarce.

CHAPTER 3

COUPLED TURBIDITY AND SPECTROSCOPY PROBLEMS: A SIMPLE ALGORITHM FOR VOLUMETRIC ANALYSIS OF OPTICALLY THIN OR DILUTE, IN VITRO BACTERIAL CULTURE SYSTEMS

3.1. Introduction

From basic research in fields as disparate as evolutionary biology or the mechanisms of photosynthesis**,** to applied research on subjects from biofuel production to nuclear waste remediation, there is general interest in improving our basic understanding of bacteria and bacterial cultures[103-112]. In a variety of important situations, bacterial cultures in fluid media are optically thin or optically dilute systems such that light can be propagated into a culture and subsequently detected outside, all in the single scattering regime. This paper is about obtaining quantitative information from such mildly turbid systems, noninvasively and continuously.

In this limit all collected light has endured no more than two elastic scattering events involving either 1) the incoming probing light, 2) Rayleigh/Mie scattered light or 3) inelastically scattered light as it propagates from where it was created to where it is detected. For any given probing/collection geometry this implies an upper limit to the number density of bacteria and/or the physical thickness of the probed system, above which the single scattering requirement is not met. Although turbid systems are heterogeneous on the wavelength scale, our approach also requires the system to be spatially homogeneous on the larger scale of macroscopic propagation of the light through the sample. We report here an approach that allows spectroscopic and physical scattering probing of such mildly turbid systems, thereby noninvasively, simultaneously and quantitatively monitoring the number density of bacteria and the chemical state of the medium.

There are better methods for number density measurements, e.g. flow cytometry and medium composition and measuring the effects of metabolism like HPLC[37-39, 113, 114], but these require physical sampling and cannot be done simultaneously to the same sample nondestructively and continuously. They do not allow real-time, simultaneous recording of properties as a culture develops. Real time monitoring of organisms in their natural habitat could allow high-throughput measurements of the effects of many kinds of stimuli e.g. added chemicals and gases, temperature, light, or pressure, relative to baseline behavior that can be established with accuracy and precision, as we show in this paper.

3.1.1. Problems in characterizing and monitoring bacterial cultures

Conventional bacteriology[34, 36, 46] practice relies on measuring the apparent absorbance or optical density of a culture at 600 nm (OD600) to establish number density of organisms at the outset of an experiment and possibly later as well. This practice began with Koch[35] and others[115, 116] and was put on a quantitative basis by establishing an empirical correlation between the dry weight of bacteria recovered from a culture and the OD600 that could be measured with newly available UV-visible absorption spectrometers. Substituting OD600 measurements for dry weight measurements improved the throughput and quality of experimentation and thus accelerated the rate of discovery. The technologies of spectroscopic probing have improved steadily over the last 40 years to the point where, for bacterial cultures in fluid media, it is possible to improve on OD600 as a basis for estimating number density, culture viability, and phenotypic expression while improving the reproducibility of experimental conditions.

To appreciate the possible improvement, note that the use of OD600 by itself cannot differentiate between scattering losses due to bacteria, scattering/absorption losses due to debris/particulates in the culture and on the cuvette walls, and absorption by chemical species or films. As chemical species are consumed or produced during the lifespan of the culture, absorption changes cannot be separated from variation in scattering losses i.e. turbidity changes as the number density of organisms and/or their cellular size varies. Thus, by itself OD600 cannot provide chemical information about the medium. Furthermore, OD600 is susceptible to a small but systematic error if a film is deposited on the surfaces of the container e.g. the cuvette, as we have shownelsewhere[20]. Note that a film/debris that causes a change in apparent absorbance of 0.01 AU corresponds to a 3% discrepancy in organism apparent number density per surface, and there must be at least two surfaces in probing the absorbance of a cuvette and its contents.

In choosing a course to improve upon OD600, there is considerable latitude depending on the specific goals of an experiment. Our general goal is to provide a reproducible, convenient, noninvasive method for 1) establishing the initial number density of organisms and concentrations of nutrients and 2) allowing continuous, noninvasive monitoring of number density increase and measures of metabolic activity, with no physical sampling. Then, more experiments can be performed on the same culture, as the life cycle of the culture plays out. By establishing a quantitative connection with OD600, we establish full backward compatibility since we also establish a connection with dry weight.

We note that literally all samples produce a remitted light spectrum containing broadband fluorescence and weaker Raman emission like that shown in Figure 3-1. The emission near 0 cm^{-1} Raman shift is comprised of both Rayleigh and Mie scattered light and is termed elastic emission or “EE”. In our present experimental configuration, it is measured by integrating from -5 to +46 cm^{-1}. The inelastic emission is referred to as “IE” and in our present experimental configuration is measured by integrating Stokes emission from ~900 to 1802 cm^{-1}. The integration range for the IE was chosen to maximize the IE collected while minimizing the amount of EE contamination included in the IE. We note that either kind of emission presents specific possibilities for revealing information about the bacterial system using the approach described in this paper. Variations of Figure 3-1 have been shown in earlier publications where the algorithm was described in different contexts.[27, 117]

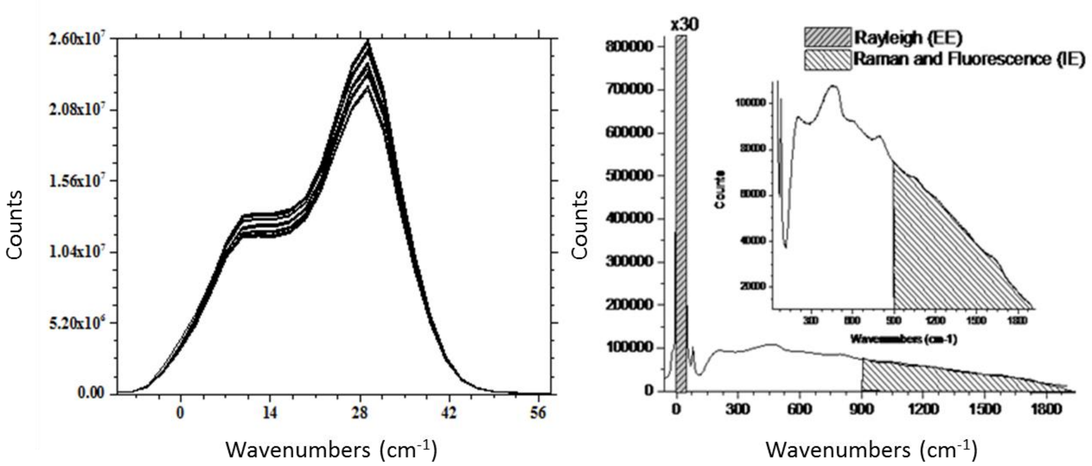

Figure 3-1. Using a 785 nm laser, an example of a spectrum taken with 200 msec frame of Andor CCD for a NC culture suspended in LB. The range used to calculate IE was ~900 to 1902 cm^{-1} and the range used to calculate EE was -5 to +46 cm^{-1} which are highlighted.

While attempting to improve our capacity to monitor bacterial cultures, the spectroscopy of traditional or "legacy" media like LB medium must be considered, if only to provide some backward compatibility in comparing future results with the existing extensive literature. Indeed, the ambiguity of the composition of LB leads to ambiguity in the spectroscopy and the interpretability of the behavior of the various contributors to the IE. This situation prevails in spite of a strong shift in research and applied bacteriology[118-123] towards use of so-called "chemically defined" media (CD), of which minimal medium (MM) is an example.

MM are isotonic fluids that contain single inorganic sources of the essential elements needed to support culture health as well as a single well-defined source of molecular carbon. CD media provide improved control and reproducibility of the cultures.[118-123] LB media contain a broad range of materials, such as proteins, carbohydrates and lipids as relatively unrefined biological sources e.g. yeast extract ortrypsinized milk. They are thus complex mixtures that defy the detailed analysis that is possible with CD media. In this work we show how to analyze for LB medium taken as a composite material and how to compare its effect on a bacterial culture with the corresponding effect of a more well-defined chemical like glucose. We also show that it is possible to achieve the single-scattering regime in bacterial cultures with a complicated fluid phase.

What chemical information can be obtained depends on the spectroscopic assignment of the sources of the various kinds of emission, and the propagation of light in the sample. Minimal media, despite comprising only a single molecular source of carbon, e.g. glucose or lactate, along with inorganic nitrogen, phosphorus and sulfur, can still produce complicated spectroscopic behavior. Absorbance can be as important as elastic scattering because it affects both EE and IE. Early experiments in our lab have shown that inclusion of transition metals in MM, e.g. Wolfe's trace metal mixture with copper[124, 125], that absorbs near infrared emission, can modulate the detected IE in complicated ways. Transition metals can complex to the nitrogen, sulfur and phosphorous donors, shifting absorption profiles and further complicating the IE.

The IE includes fluorescence and/or phosphorescence as well as Raman scattering. Either fluorescence or phosphorescence is usually more intense than any spontaneous Raman scattered emission component. We have previously[27] surveyed various kinds of biological materials that are potential sources of Raman scattering and fluorescence/or phosphorescence under NIR excitation[126] and that display photobleaching as is common for materials in biological media. [127] *In vitro* spectra of authentic samples of materials and constructs, e.g. tissue phantoms, can provide inferences or support for a hypothetical assignment. While specific assignments are rarely unequivocal it might be useful to discern if there are materials in e.g. LB medium that are either consumed or transformed from an emissive material into a non-emissive material or vice versa. We make this suggestion because of the observation of NIR induced autobleaching[126, 127] and also of that inflammation in injured spinal cord tissue in vivo or ex vivo is accompanied by increased autofluorescence.[128-133]

3.1.2. The BSN algorithm

The system is closed except for possible evaporation/condensation loss/gain of water, or loss of carbon as gaseous CO or CO_2. With those exceptions, the atoms that were present initially in a culture sample, or were added during the culture lifetime, remain in the culture. Since there may be a metabolic redistribution of the chemical bonds present, we might expect the Raman and/or fluorescence spectra to change, perhaps in complicated ways that cannot be fully accounted for using the BSN approach. For a complex medium, the approach we describe provides a sensitive and potentially quantitative probe of changes in the medium optical or spectroscopic properties due to culture growth and metabolism.

In collecting the EE we sometimes inadvertently include some light from reflections from the liquid sample surface or the bottom or other surfaces of the cuvette. This artifact must be managed as discussed below in order to produce reliable inferences concerning the behavior of the culture. Similar management is required for the IE because the IE can be contaminated by fluorescence or Raman from the cuvette produced by stray incident light.

For a 3-phase system like those considered previously[27], there are two independent intensive parameters, taken as the volume fractions of phases 1 and 2, i.e. ϕ_1 and ϕ_2. (Obviously, $\phi_1 + \phi_2 + \phi_3 = 1$.) In the present application, phases 1 and 2 will be NC and LB. Two spectroscopic parameters, IE and EE, are measured (see above). If the sample volume is fixed, and assuming we are in the single-scattering regime, these two parameters are linearly dependent on ϕ_{LB} and ϕ_{NC}. Consequently, ϕ_{LB} and ϕ_{NC} are linear functions of IE and EE. This linear dependence is defined by 6 constants, a, b, c, d, e, and f.

$$\phi_{NC} = a + b\mathrm{IE} + c\mathrm{EE} \qquad (3\text{-}1)$$

$$\phi_{LB} = d + e\mathrm{IE} + f\mathrm{EE} \qquad (3\text{-}2)$$

Once the values of these 6 parameters are established, a measurement of IE and EE becomes a measurement of the three volume fractions.

In general, we can determine the values of two independent intensive variables from measured EE and IE. In the case of a bacterial culture, which is a two-phase system, one of these parameters is the volume fraction of bacteria ϕ_1. The volume fraction of medium is just $1 - \phi_1$. The second intensive parameter, ϕ_2, may be the concentration of some biologically produced material like tryptone or peptone, or of specific chemicals/molecules added as sources of carbon, sulfur, phosphorus or nitrogen, like glucose.

In this paper we present and analyze results of probing an open-top culture with a single laser and show the advantages over measuring OD600. In general an absorption measurement has smaller signal-to-noise[134, 135] than an emission measurement, sometimes by as much as 3 orders of magnitude. The improved enabling technologies of emission spectroscopy make it relatively easy to use a single-color laser to induce both elastic and inelastic emission essentially simultaneously. Also, it is likely possible to achieve higher performance in smaller, less expensive and more highly integrated packages, so that the approach could enjoy easy adoption in production facilities. Separating emission into elastic and inelastic contributions is easily accomplished using commercial off the shelf filters and optical components. Because we detect some light that is physically scattered, as in nephelometry, as well as light that contains spectroscopic information, and because there are only two phases in the samples, a particulate/scattering phase and a non-turbid fluid phase, we call our approach and algorithm binary spectronephelometry i.e. BSN.

The total remitted inelastic light (IE) is comprised of two components, narrow band i.e. Raman scattered light, and broadband i.e. fluorescence and/or phosphorescence. Since there is no background emission, it is possible to measure the IE to better than ±0.01% precision, so small changes in IE can be easily discerned. Since Raman features can be localized to spectral intervals as narrow as ≈10-20 cm^{-1}, very specific and small changes can be observed even with the background produced by complicated media. Since spontaneous Raman scattering is usually a parts per thousand analytical technique[135], this can be a limitation on the proposed approach. If the chemical information is contained in the fluorescence, the sensitivity can be better i.e. less than parts per million is common place. Thus, complex media can be probed for changes in chemical state.

We show that for the complex medium LB, we can construct an empirical calibration system that enables quantitative monitoring of chemical and physical changes of the bacteria and the medium during the life of a culture. However, it may prove difficult to assign the source(s) of the changes. For CD media like MM on the other hand[118-123] we have a much simpler, less ambiguous and direct approach to monitor the metabolic activities of the culture.

We now turn to experimental details. Application of the BSN algorithm follows with typical calibration results and tests of internal and external consistency. We then show results of applying BSN to bacterial growth curves. To see how these results may be combined with conventional spectroscopy, we present experiments in which glucose was added to LB or MM growth media and we measured the uptake of glucose. We calculate the amount of glucose consumed per organism per second and compare that to the rate of glucose molecules arriving at the organism membranes. We suggest that if such measurements can be done with accuracy and precision it will be possible to characterize other processes in bacterial cultures. Standard chemometric analysis i.e. Principle Component Analysis is employed to probe the composition of the IE.

3.2. Materials and Methods

BL21 Gold (DE3) Escherichia coli (NC) with a pET27b(+) sapB vector insert was obtained from Dr. R.P. Doyle (Syracuse University, Syracuse) grown in LB with 5 μL of kanamycin (35 mg⁄mL) (IBI Scientific, Peosta, Iowa). Phosphate-buffered saline (PBS) (1× solution) (ICN Biomedical Inc., Aurora, Ohio), Difco^{TM} M9 Minimal Salts and NaCl (Fisher Scientific), Bacto™ Tryptone (Becton, Dickson and Company Sparks, Maryland), and yeast extract (aMReSCO, Solon, Ohio) were used without further purification.

Films grown on quartz utilized Hellma Analytics High Precision 1 cm cuvettes made of Quartz Suprasil (#101-10- 40). The surface quality, i.e., roughness of the quartz cuvettes or substrates, is assumed to be λ⁄10 across the entire UV-NIR range based on the specifications of comparable quartz discs produced by Heraeus, the entity that we believe produces the quartz for both Hellma cuvettes and Starnacells. High quality fused silica is the material of choice in order to minimize fluorescence from the cuvette produced by stray incident light although we have used inexpensive polystyrene successfully too.

Nearly all OD600 spectra were obtained using a Perkin Elmer Lambda 950 UV/Vis spectrophotometer but some results were obtained using an Agilent Cary 60 UV/Vis. Spectral scans were set to a 2 nm slit width, 1.0 s integration time, and 1.0 nm data interval. Before scanning the sample, the spectrometer was normalized ("auto-zeroed") with a cuvette containing 3 mL of LB over the same wavelength range.

Using a flexible temperature probe attachment connected to a Vernier LabQuest 2 Logger Pro, temperature data was collected. We employ a 785 nm, continuous wave external cavity laser (Process Instruments, Salt Lake, UT) that can generate a maximum of 450 mW at the location of the sample in a bandwidth of 1.5 cm^{-1} within a multimode spatial distribution. We employ ~180 mW of laser power in a roughly square shaped spatial distribution that is focused to a spot about 0.125 mm wide inside the sample.

The sample is housed in a custom made temperature controlled base. The base height is 3.50 cm and the cuvette height is 4.50 cm. These dimensions were used to ensure the sample is covered by the walls of the base to allow homogeneity in heating and or cooling of the sample, but still allow easy removal of the cuvette from the base. To set up a system that produces valid measurements across a range of variable turbidity, under conditions of relatively low turbidity, which restricts the light which can be collected to a smaller spatial region, the focus of the laser was preset to begin ~4 mm below the surface of the liquid. The depth of focus was such that all focused incident light was contained at a location ~1±0.5 cm below the top surface of the culture, or ~2±1 cm from the bottom of the culture. A magnetic stirrer was added to the setup in order to maintain constant stirring of samples during the experiments. To insure that the stir bar didn’t directly scatter light itself, the stirrer was place off center of the cuvette so that the stir bar was actually spinning parallel to one of its verticle sides i.e. around an axis normal to a cuvette side.

The following times/CCD temperature were chosen to allow data collection to ocur in the shot noise limit. The data for the training set was collected on the Andor CCD Camera, which was cooled to -55^{o}C, had an acquisition time of 5 minutes with 1500 accumulations of 200 msec frames for each spectrum. The experimental setup is shown in Figure 3-2.[27] Unlike standard Raman apparati, this system is not intended to completely suppress the Rayleigh/Mie scattered light i.e. the EE. Since the available filter set is commercial off the shelf (Semrock, Rochester, NY) and since it is not being used as designed/intended, detuning the edge filter induces some oscillations in the spectrum at Raman shiftslower than 800 cm^{-1}.

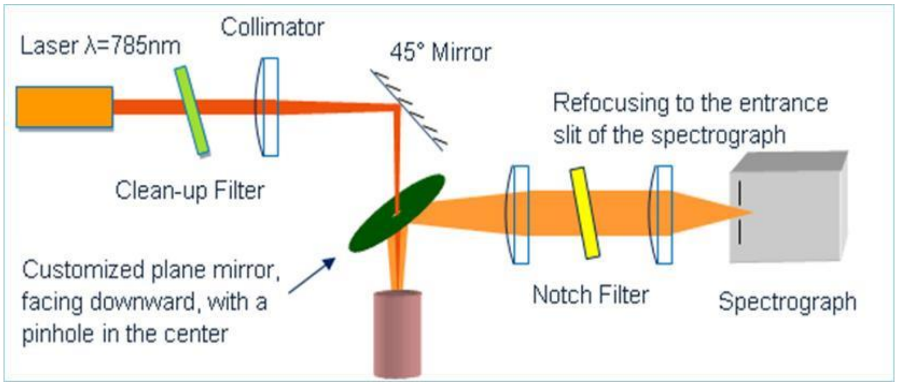

Figure 3-2. Experimental setup of the 785 nm NIR laser with an added stirrer and temperature controled base that was used in our apparatus.

Growth curve data had an acquisition time of 1 minute with 300 accumulations of 200 msec frames for each spectrum, and the counts were then scaled up to match that of training set data. Aliquot experiment data had an acquisition time of 30 seconds with 150 accumulations of 200 msec frames for each spectrum, and the counts were then scaled up to match that of training set data. The culture was grown and analyzed over a 24-hour period while stirred at 37^{o}C. Addition of 25 µL of medium every 30 min was required to keep the culture at a constant volume, and the focal point of the laser fully submerged.

Sample Preparation of LB: LB medium contained 10 g/L tryptone, 5 g/L yeast extract, and 10 g/L NaCl at 37°C. The pH of the medium was maintained at 7.0 with NaOH. The solution was stirred to homogeneity, and then diluted to a final volume of 500 mL with DI water. The medium was then autoclaved at 121°C for 15 min in a water bath.

Sample Preparation of MM: MM contained 5.64 g of Difco^{TM} M9 Minimal Salts 5x. The solution was stirred to homogeneity, and then diluted to a final volume of 500 mL with DI water. The medium was then autoclaved at 121°C for 15 min in a water bath. Then 10 mL sterilized 20% glucose solution, 1 mL of sterile 1.0 M $MgSO_4$, 0.1 mL sterile 1.0 M $CaCl_2$ and 500 µL of kendomycin was added to the medium after it was autoclaved.

Sample Preparation for Growth Curves: 5 mL of LB with 5 µL of kendomycin was inoculated with NC and allowed to grow over a 24 hr period in an incubator at 37^{o}C with stirring. 200 µL of NC was used to inoculate a new 5.00 mL sample of LB with 5 µL of kendomycin. 3.50 mL of newly inoculated culture and a micro stir bar were placed in the quartz cuvette, and placed in a temperature controled cuvette holder to maintain constant temperature of 37^{o}C and allowed to stir while data was being collected. Due to evaporation, aproximately 25 µL of LB needed to be added every 30 minutes in order to maintain a constant 3.50 mL in the cuvette.

Sample Preparation for Aliquot Experiment: 3 mL of LB with 3 µL of kendomycin was placed into a quartz cuvette with or without a biofilm present.[20] At ~45 seconds into each 3 minute kinetic series with a spec time of 30 sec, 5 µL of NC (OD600= ~1.000 in the same LB the bacteria were grown in) or pure unfiltered LB was added to the cuvette over a 2 hr period. At the temperature employed i.e. 37° C the 5 µL aliqouts were chosen because they were close to the evaporation loss thus the total volume of the cuvette remained constant.

A “101-7” arbitrary baseline correction, which allows narrow peaks on a sloping or broadly “hump-shaped” fluorescence background to be studied, was applied to all raw spectra.[27,

[28] The 101 and 7 point adjacent averaging was chosen partly by empirical observation after noting how others performed similar corrections.[22, 23, 26] From our own studies[27, 28], a 101-7 was shown to produce very reliable quantitative calibration curves as well as spectra that had the most realistic appearance of pure Raman spectra based on subjective judgment/visual inspection. Note that the instrument function for our spectroscopic system is not applied to any of the results shown because it does not facilitate the analysis or the background subtraction process.

The 101-7 procedure is statistically unbiased i.e. it produces a baseline-corrected spectrum with zero mean without making assumptions about what part of the total IE spectrum has little or no Raman activity. The effect on a spectrum can be expressed analytically aiding further data analysis and algorithm development.[27, 28] Note that before statistical/chemometric analysis raw spectra are usually processed as a set and the standard normal variant transform is used for normalization i.e. zero mean and unit standard deviation. The 101-7 baseline correction achieves zero mean in a single step while improving the dynamical range of the apparent Raman emission the providing a quantitative estimate of the amount of underlying fluorescence.

3.3. Results

3.3.1. Empirical calibration of the BSN algorithm-“Training Sets”

Sample Preparation for Training Sets: Four vials containing 5 mL of LB with 5 μL of kendomycin were inoculated with NC and incubated over a 24 hr period at 37°C with shaking. The contents of these four vials were then combined into one larger sterile vial. Six stock solutions of PBS and LB were prepared and placed into sterile plastic vials for all trials. Vial one contained 15.00 mL of filtered LB. Vial two contained 13.50 mL of filtered LB and 1.50 mL of filtered PBS. Vial three contained 12.00 mL of filtered LB and 3.00 mL of filtered PBS. Vial four contained 10.50 mL of filtered LB and 4.50 mL of filtered PBS. Vial five contained 9.00

mL of filtered LB and 6.00 mL of filtered PBS. Vial six contained 7.50 mL of filtered LB and 7.50 mL of filtered PBS. 1.50 mL of NC and 1.50 mL of respective stock. Serial half dilutions were made of each sample producing a training set containing 36 samples.

Since each sample was a mixture of NC, LB, and PBS, the volume fractions of NC and LB, ϕ_{NC} and ϕ_{LB}, were taken as the two independent intensive parameters, with $\phi_{PBS}= 1-\phi_{NC}-\phi_{LB}$. Since each sample was made from equal amounts of an LB-PBS mixture with volume fraction of LB v_{LB} and an NC-PBS mixture with volume fraction of NC v_{NC}, the actual volume fractions of LB and NC in the sample are $\phi_{LB} = 0.5\ v_{LB}$ and $\phi_{NC} = 0.5\ v_{NC}$. The measured EE and IE (counts) are plotted in Figure 3-3 vs. ϕ_{LB} or ϕ_{NC}.

Since the data is collected in the shot-noise limit the large number of counts for both the raw EE and IE makes the experimental error bars for each datum smaller than the symbols used in the graphs. The deviations from the lines are therefore due to errors in volume measurement and/or perhaps originate in inhomogeneity of the sample with changing concentration. The concentration ranges were chosen to avoid nonlinear dependence of counts on concentration (see below). Since one needs to state a tolerance to make such a definition, there is some subjectivity involved. We compared changing NC concentration with constant LB concentration and changing LB concentration with constant NC concentration (Figure 3-3). The linear range for NC is determined by the behavior of the EE data and for a 1 cm cuvette and our geometry was shown to extend to at least EE = 2.45×10^{8}counts$\approx$0.323 AU OD600 (Figure 3-3C).

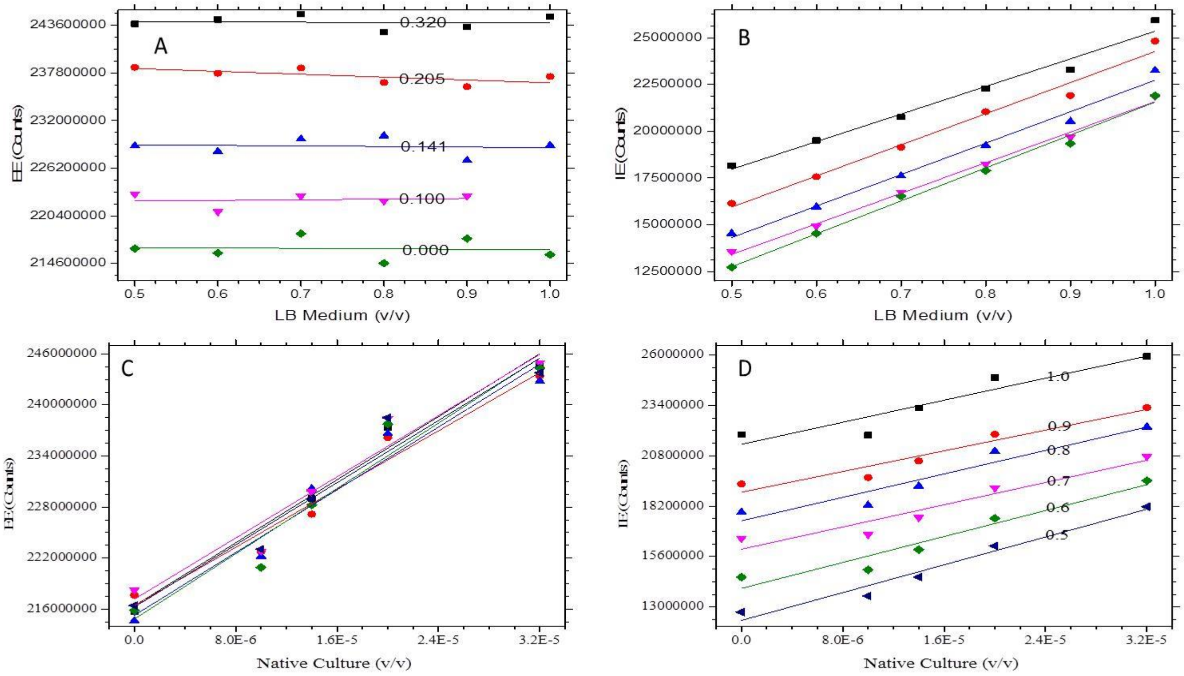

Figure 3-3. Training set data for both EE and IE for NC and LB. The EE (-5 to +46 cm^{-1}) and the IE (900-1902 cm^{-1}) are summed up after an average dark current subtraction of each spectrum has been performed. The EE (A) and IE (B) of changing LB at constant NC (v/v): 3.20E-5 (■), 2.05E-5 (●), 1.41E-5 (▲), 1.00E-5 (▼), 0.00 (♦). The EE (C) and IE (D) of changing NC (v/v) at constant LB (v/v): 1.00 (■), 0.900 (●), 0.800 (▲), 0.700 (▼), 0.600 (♦), and 0.500 (◀). One outlier at 1.00E-5 NC (v/v) in 1.00 v/v LB was removed from the training set with a certainty greater than 99% due to the Q test.

The training set results were used to find the values of the 6 parameters in Equation [3-1]. Then the BSN algorithm, with these parameters, was used to quantitatively analyze all other data acquired. For example, as shown below in the Results section, it was used to quantify the growth of NC and the depletion of nutrients.

To estimate the importance of the quadratic and combination terms EE^2, IE^2 and EE*IE, which may arise from the turbidity, these terms were added to Equation [3-1]. Results are shown in Figure 3-4. The reduction in residual sum of squares of deviations (RSS) was compared to the increase in number of parameters using the F test. Inclusion of a quadratic term in EE was not statistically significant at 95% confidence and inclusion of other terms by themselves or in combination were also not statistically significant. Including only the linear terms produces a model that predicts, within experimental error, both the NC and LB concentrations. Plotting calculated vs. actual LB concentration produces a line with a slope of 1, an intercept of 0 and with the slope known to better than ±2% precision at 2σ. This implies that, in the range studied, the variation of the IE with changing LB concentration is linear with a slope independent of the NC concentration.

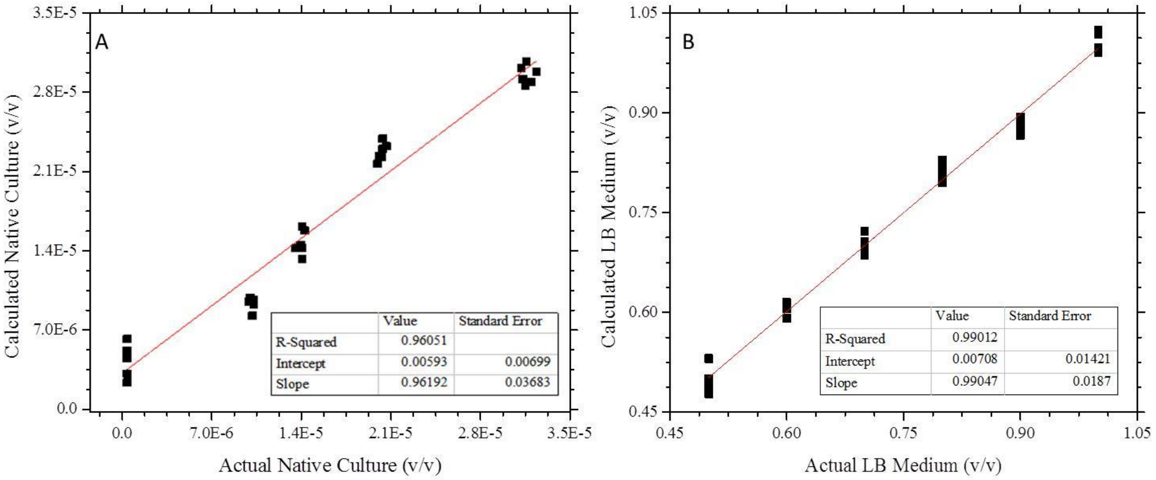

Figure 3-4. Calculated data for NC and LB generated by the algorithm when applied to the training set data. (A) The volume fraction of NC calculated using BSN without the quadratic terms plotted versus the actual volume fraction of NC. (B) The volume fraction of LB calculated using BSN without the quadratic terms plotted versus the actual volume fraction of LB.

For the training set results in Figure 3-3B we observe that while the intercepts of the linear IE dependence on LB concentration depend strongly on the NC concentration, the slopes do not. Thus, IE is a bilinear function of NC and LB with no cross term. Also, NC is independent of IE.

This has important ramifications for the use of Raman spectra to monitor specific components in the fluid phase. In particular, a simple Raman calibration curve using non-turbid solutions can be obtained for some component such as glucose. Then, within a constant additive factor, it will be valid for measuring glucose concentration for all bacterial volume fractions spanning the linear range of turbidity. The constant additive factor can be obtained from the training set data so long as the training set and the Raman measurements utilize the same optical probing geometry. A complete and general example of this approach is beyond the scope of the present paper and will be presented separately later, but we note that obtaining the additive factor involves using the fractional increase in IE with fractional increase in scattering phase i.e. Figures 3-3B and 3-3C. We denote the volume fractions of the three liquids in the samples in the training set by ϕ_{LB}, ϕ_{NC} and $\phi_{PBS} = 1 - \phi_{LB} - \phi_{NC}$. The parameters in the BSN algorithm (Equation [3-1]), determined from the training set, are given in the table.

Table 3-1. Parameter values obtained from applying the BSN algorithm to the Training Set data.

Parameter	Value	Standard Error
a	-2.28x10^{-4}	0.105x10^{-4}
b	1.07x10^{-12}	0.0510x10^{-12}
c	–3.01x10^{-14}	1.55x10^{-13}
d	1.87	0.130
e	–9.70x10^{-9}	0.629x10^{-9}
f	5.86x10^{-8}	0.192x10^{-8}

3.3.2. Application of the BSN algorithm

All the samples in the training set are mixtures of LB, PBS, and NC. PBS makes only a small contribution to IE and EE, and LB makes only a small contribution to EE. The algorithm allows us to calculate the volume fractions of the three components (ϕ_{LB}, ϕ_{NC} and ϕ_{PBS}) in an unknown mixture from measured EE and IE.

We note the organic fraction of the LB mixture contributing to the Raman scattering comprises tryptone and yeast extract i.e. enzymatic protein digests. Since the IE includes a large frequency range, we must group the contributions of tryptone and yeast extract together. Since both substances are mostly composed of amino acids, with average molecular mass of 137.20

g/mol (average over the 20 amino acids, essential and non-essential), we can convert the 15g/L to an amino acid concentration of (15/137.20)M. Thus the concentration of amino acids is [ϕ_{LB}][0.109M].

3.3.3. Known Artifacts and Internal Consistency

Although we explore the possibility of using the BSN approach in various types of research and production/reactor systems e.g. closed, open, batch, flow and hybrids, our current apparatus was open requiring maintenance. After dozens of preliminary experiments to provide a basis, we devised the aliquot experiment that we executed and completely repeated to produce the results in Figure 3-5. We show one full data set because it allows facile anticipation/demonstration of the appropriate BSN response. The volume of the aliquots was chosen to replace the net loss of culture volume due to apparent evaporation as closely as possible, so that the total volume in the cuvette remained constant (3 mL). Aliquots of either NC or LB were added at equal time intervals to fresh, non-bacteria-inoculated, kendomycin-protected LB. If NC contains only bacteria and LB, aliquots of NC should result in a (v/v) NC change per aliquot of $(2.6 \times 10^6 \mu m^3)/(3 \times 10^{12}\ \mu m^3) = 0.87 \times 10^{-6}$. If LB is a homogeneous phase, the LB v/v calculated by BSN should be unchanged from 1.0 with added LB aliquots, if the aliquots replace the exact volumes of that homogeneous phase that leaves by evaporation. These two expectations are indicated by green lines in Figure 3-5.

However, LB medium is demonstrably not homogeneous. First, the concentrations of fluorescence/Raman producing chemicals would be expected to increase over time if only water evaporates. Second, the presence of particulates in fresh or old LB is easily demonstrable. Third, particulates must also be transferred when either NC or LB aliquots are added. And finally, autofluorescence and photobleaching are well known contributors to IE and its variation over time for NIR irradiation of biological systems in general.[136, 137] Furthermore, biofilms contain bacteria, particulates and chemicals from whatever medium is present internally and on the surface.

Biofilms[20] form on surfaces in contact with bacterial cultures, whether in closed, open or flowing systems. Thus, we included experiments in which a cuvette had its internal surfaces prepared i.e. biofilm coated by a culture for 24 hrs before the old culture was poured out and fresh, non-inoculated LB was placed in the cuvette to start an aliquot experiment. All these effects are visible in the qualitative response of EE and IE with the added aliquots in the form of the calculated NC and LB volume percentages in Figure 3-5.

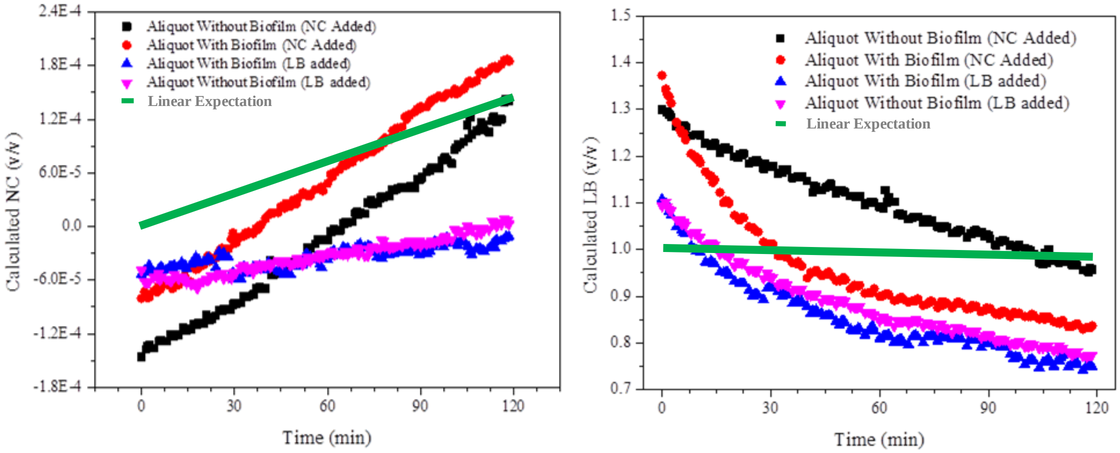

Figure 3-5. At ~45 seconds into each 3 minute kinetic series with a spec time of 30 sec, 5 µL of NC (OD600= ~1.000 in the same LB the bacteria were grown in) or pure unfiltered LB was added to the cuvette over a 2 hr period. At the temperature employed i.e. 37°C the 5 µL aliqouts were chosen because they were close to the evaporation loss thus the total volume of the cuvette remained constant. Left) Observed, i.e. calculated from IE and EE, NC concentration with timed addition of aliquots of NC (5 µL of NC, OD600 ~ 1.0) from a stock culture. Right) Observed LB concentration with addition of successive aliquots of LB from a stock LB.

At certain times the calculated volume fractions of NC and/or LB are either negative or greater than one relates 1) to the design of our optical system, 2) to the presence of particulates in LB and 3) the manner in which the BSN training set model was constructed and calibrated.

Furthermore, and not surprising for a manually executed experiment, there are occasional discontinuities, e.g. at about 30 minutes and again near 60 minutes, in the calculated LB and NC when LB were added with a biofilm present. The presence of an unwanted bubble, which can produce unwanted reflections affecting both the EE and IE, cannot always be anticipated or seen before making a measurement. Each data set contains 150, 5 μL aliquots and one aliquot involving a partially plugged/cracked pipettes tip will produce a response unlike the others.

In the construction of the training set, PBS was used to dilute "full strength" LB i.e. LB v/v=1 (by definition) to produce lower values of LB v/v. PBS does not contain particulates whereas LB necessarily contains particulates and in this approach to BSN calibration both, the chemicals in LB and the particulates change together, in constant proportion. But the inherent particulate fraction of LB itself must change over time if only because water can evaporate but particles cannot. This should affect the relative variation in EE and the production/collection of IE due to light propagation effects.

With regard to the design of our optical system, if the top level of the liquid in the cuvette varies by about 10^2 microns or more, the baseline raw EE and IE signal values change. The movement defeats the spatial filtering meant to block unwanted reflections from the top surface mostly affecting the EE. The movement also affects the collection efficiency of emission i.e. both EE and IE from within the cuvette. If the cuvette liquid surface in the aliquot experiment is shifted from the position used in constructing the training set, the position of 0 NC v/v or 0 LB v/v/ will be shifted. We also expect a proportional and opposite response of the calculated NC and LB responses reflecting the basic assumption of the model, $\phi_{NC} + \phi_{LB} + \phi_{PBS} = 1$.

In Figure 3-5 we observe the BSN-calculated NC response to added E. coli (NC) is linear regardless of whether the cuvette contained a biofilm. This is expected for the biofilm-free case since the aliquots were a small volume compared to the total cuvette volume, and they were delivered at equal time intervals. If the bacteria were sticking to the cuvette surfaces we might also expect a nonlinear effect. In contrast, as shown below a growth curve reflecting the increase in NC concentration obtained by normal reproduction after starting with e.g. an initially full cuvette containing NC is not linear over time. If the LB associated particulates dominate the production of EE after the bacteria, then the difference between the slope of the calculated value (green line) and observed value is mostly due to the scattering by the particulates.

In all experiments, once begun, the aliquots were added without moving the cuvette. The apparent constant shift between the average NC concentrations for the 2 experiments i.e. with and without biofilm present is due to the shift in cuvette position since the two experiments were executed on separate days. With no biofilm present and NC added, the calculated LB response was also linear, decreasing in a manner consistent with the basic assumption of the model.

Quantitatively, the values of LB measured using BSN should be 1.0 if the combined fluorescence and Raman do not change over time and nor does the EE. We observe the calculated LB vs time decreases monotonically and has an average value of somewhat less than ≈1.0 over 2 hours. There is a significant difference between whether there is a previous biofilm or not. The presence and inevitable production of particulates in LB independent of bacterial activities should cause a decrease in the apparent LB, as observed because the particles occupy volume. Note that there is no constraint that the observed variation in IE and EE be consistent with the overall model adding credibility to the inherent assumptions.

Whether or not a biofilm was present before NC was added, the calculated NC response was linear. However, when a biofilm was present initially the corresponding calculated LB response was not linear and decreased more rapidly than when no biofilm was present for the first 30 minutes. After the first 30 minutes, the BSN calculated LB decreased in a manner consistent with the variation with LB and NC aliquots. After the first 30 minutes the LB slopes were all roughly equal.

To help associate Raman features with either NC or medium, the variation of the Raman signals with LB and NC proportions is shown in Figure 3-6. We use 101-7 baseline corrected raw data for 900-1902 cm^{-1} to minimize the fluorescence contribution. The Raman shift range for these baseline-corrected spectra was chosen to be the same as that used to delineate the IE scattering with minimal contribution from EE scattering. Although we shall make some assertions as to possible assignments of Raman features to actual chemical entities, we harbor no delusions that these assignments are proven.

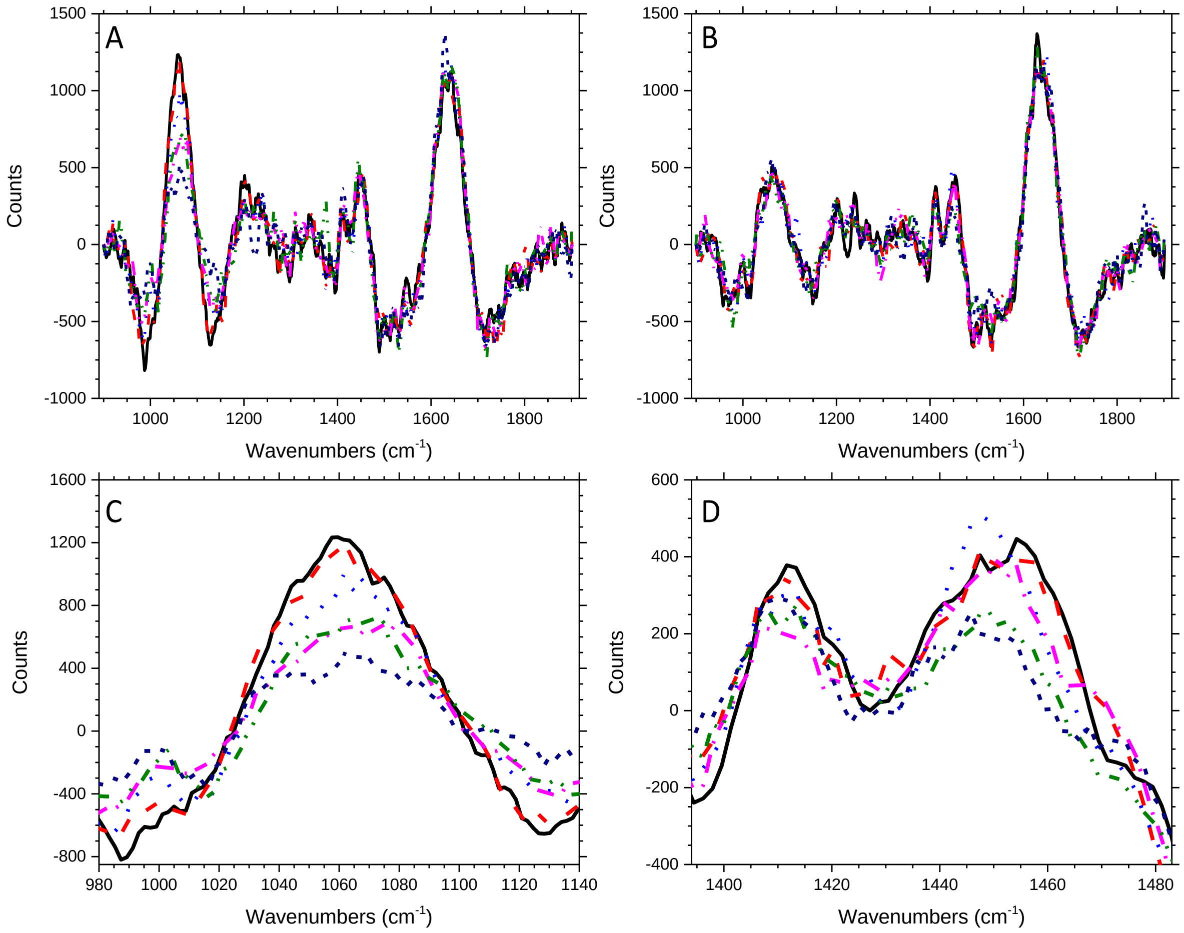

Figure 3-6. 101-7 baseline corrected Raman spectra of 6 serial dilutions of NC in LB. (A) 101-7 baseline correction applied to spectra with changing NC (v/v) at constant LB=(1.00 v/v): 5.03E-4 (——), 3.20E-4 (– –), 2.05E-4 (●●●), 1.41E-4 (–●–), 1.00E-4 (-●●-), and 0.000 (– –) over the range of 900-1902 cm^{-1}. (B) 101-7 baseline correction applied spectra with changing LB (v/v) at constant NC=(0.000 v/v) over the range of 900-1902 cm^{-1}. (C) Zoomed in on 1060 cm^{-1} peaks for a spectrum of changing NC (v/v) at constant LB: 5.03E-4 (——), 3.20E-4 (– –), 2.05E-4 (●●●), 1.41E-4 (–●–), 1.00E-4 (-●●-), and 0.000 (– –). (D) Zoomed in on ~1412 cm^{-1} and 1455 cm^{-1} peaks for a spectrum of changing LB (v/v) at constant NC: 1.00 (——), 0.90 (——), 0.80 (●●●), 0.70 (–●–), 0.60 (-●●-), and 0.50 (– –).

We note that, while LB is a very complicated mixture, Raman features at ~1412 cm^{-1} and 1455 cm^{-1} (Figure 3-6D) correlate strongly with (C(6)-H_2●COH) and (CH_3) stretches and that usually such moieties do not hydrolyze in aqueous media.[138] The most likely source of such vibrational motions, alkyl chains, are present extensively in both LB and the organisms themselves i.e. NC. The effect on the Raman spectrum of replacing one source of these Raman photons (NC) with another source (LB) is determined by the different CH_2 and CH_3 content of these sources. Thus, the strength of these two features generally increases with increasing LB above 0.6 v/v and constant NC. However, over the whole range in Figure 3-6 and in detail, their change was complicated and different for the two Raman features.

On spectroscopic grounds the feature at ~1060 cm^{-1} could come from a υ(C-O-C) asymmetric stretch or the (C-C) stretch, and be associated with the amount of “biomass” as shown in Figures 3-6A and 3-6C and more specifically in Figures 3-7 and 3-8.[138, 139] These types of moieties can certainly hydrolyze non-enzymatically, particularly if they are associated with ester linkages which would be depleted in LB. However, in viable bacteria the biomass materials are bacterial membranes e.g. phospholipids or triglycerides and these are not labile so long as the bacteria are viable.

Graphing the area under the curve (AUC) data of the peaks from Figure 3-6 in Figure 3-7, we observe that the strength of the 1060 cm^{-1} feature increases roughly linearly with the proportion of the culture that is NC, until the turbidity-limited value is reached. Thus, this feature largely comprises NC but may have LB contribution, or not, since the noise between spectra may be comparable with the changes induced by varying LB and NC proportions. The situation is better for the 1410 cm^{-1} and the 1455 cm^{-1} features as they too increase linearly in proportion to the amount of LB present in the sample apparently with less noise. The only exception is the 1410 cm^{-1} feature where the lowest concentration is higher due to interference from signal coming from the cuvette.[140] The 101-7 background-corrected Raman spectra, displaying some internal consistency, suggest that changes in the Raman spectra with perturbations caused by the cultures can be rationalized.

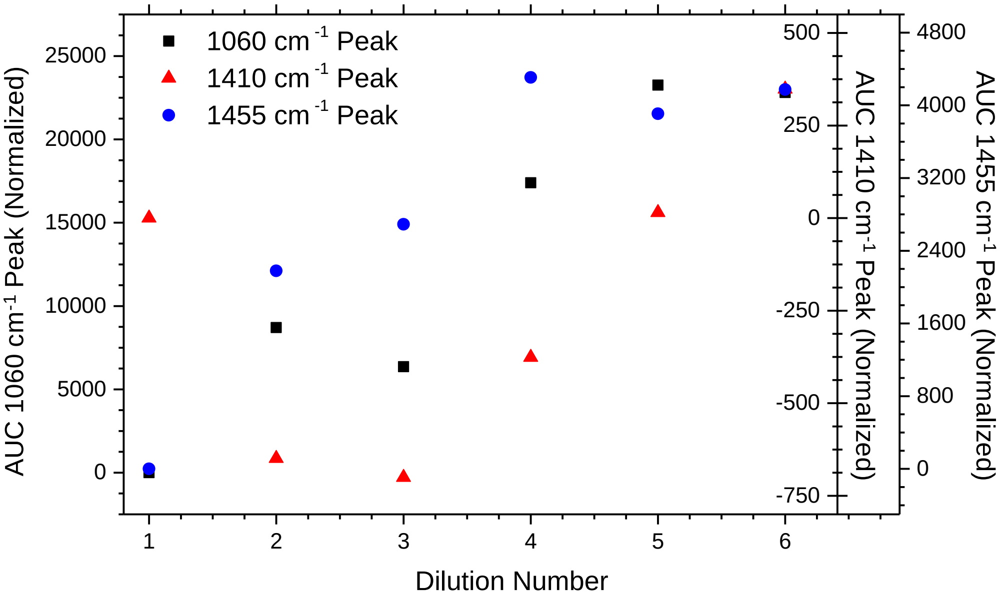

Figure 3-7. The 1060 cm^{-1} peak increases linearly with the proportion of NC while the 1410 cm^{-1} and 1455 cm^{-1} peaks increase linearly with proportion of LB. Dilution number refers to the 6 serial dilutions used in Figure 3-6 where 1-6 represent NC 0.000-0.503 respectively, and LB 0.50-1.00 respectively. All data in this figure was normalized for easy comparison.

3.3.4. Measurement of LB and glucose uptake by cells.

In order to check the plausibility of our analysis of the Raman spectra, we use these measurements to calculate the rate of glucose uptake by the bacteria. Since the NC volume fraction and therefore the turbidity increases over the course of the growth curve while the glucose concentration is changing, the rates we calculate are lower bounds. We will analyze data for bacteria in both MM and LB. LB, the traditional medium of choice for many biology and biochemistry protocols[141-145], contains multiple carbon sources such as glucose, predigested protein-containing peptides, and amino acids, whereas in these experiments MM contains only glucose as a carbon source. Therefore, MM will present less cluttered spectra for observation of depletion or growth of a chemical in a culture. This may explain why Figure 3-8B is more linear than Figure 3-8E.

In both cases, glucose was initially added to the medium in a single 25 μL bolus to produce a 0.1 M concentration, to render identification of glucose features obvious. The 101-7 baseline-corrected spectrum of culture before glucose addition was subtracted from the 101-7 baseline-corrected spectrum after glucose addition, to reveal the biomass (~996-1095 cm^{-1}) and glucose (~1095-1168 cm^{-1}) peaks and show the growth of biomass and depletion of glucose over time (Figure 3-8B, C, E, F).

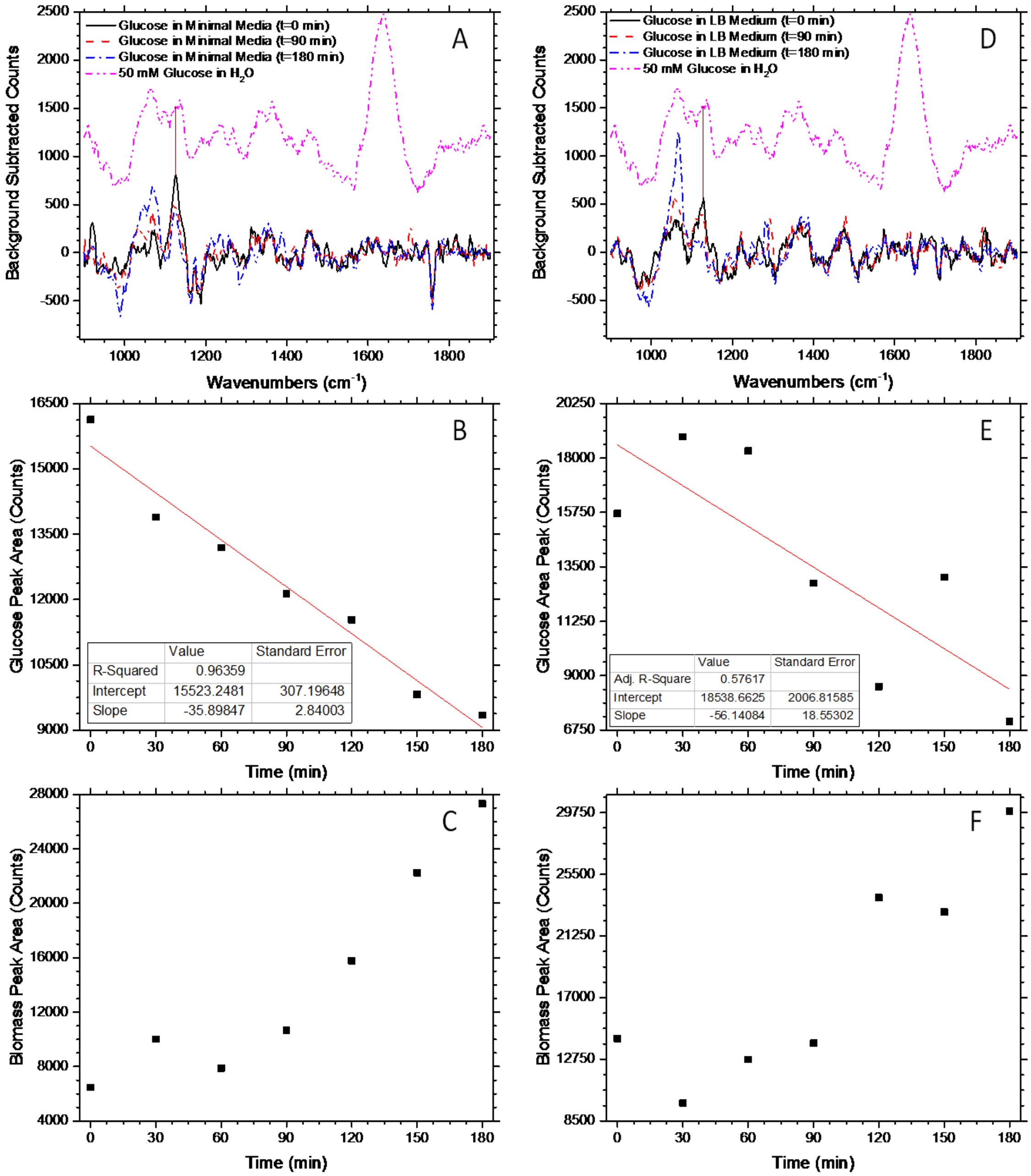

	Value	Standard Error
R-Squared	0.96359	
Intercept	15523.2481	307.19648
Slope	-35.89847	2.84003

	Value	Standard Error
Adj. R-Square	0.57617	
Intercept	18538.6625	2006.81585
Slope	-56.14084	18.55302

Figure 3-8. 101-7 data showing the growth of biomass and the depletion of glucose over time. (A) 101-7 baseline correction applied to the 900-1902 cm^{-1} range for NC grown in MM. (B) 101-7 data for the glucose peak (~1095-1157 cm^{-1}) in MM. (C) 101-7 data for the biomass peak (997-1095 cm^{-1}) in MM. (D) 101-7 baseline correction applied to the 900-1902 cm^{-1} range for NC grown in LB. (E) 101-7 data for the glucose peak (~1095-1168 cm^{-1}) in LB. (F) 101-7 data for the biomass peak (~996-1095 cm^{-1}) in LB.

From the best-fit line for MM, Figure 3-8B, Glucose Counts = 15523 – 35.90 t (min), we can obtain the factor for the conversion of counts to [glucose] as 0.1M/(15523 counts) =6.442×10^{-6} M/counts. For Figure 3-8E, for LB, Glucose Counts = 18539 – 56.141 t (min) which means that the initial glucose concentration was ($6.442\times10^{-6}\times18539$)M = 0.119 M. The additional 0.019 M must be present in the LB. This corresponds to 3.51 g glucose per L or 0.351% by weight.

The rate of glucose depletion in MM is obtained by multiplying the slope of the line in Figure 3-8B, 35.90 counts/min, by the conversion factor, 6.442×10^{-6} M/counts, to obtain 2.314×10^{-4} M/min. In LB, the rate of glucose depletion is somewhat larger, $6.442\times10^{-6}\times56.141$ M/min = 3.617×10^{-4} M/min. Multiplying by the sample volume of 3 mL, we obtain 6.919×10^{-7} mol/min for MM and 1.085×10^{-6} mol/min for LB. To convert the rates of glucose depletion to glucose intake rates per cell, we require the number of cells in the sample.

As stated above, all growth curves, including the results of Figure 3-8, started with OD600 = 0.142 and ended with OD600 = 0.733. Since OD600 = 1 corresponds to 8×10^{8} cells per mL and since the volume of sample is always 3 mL, the number of cells is 3.41×10^{8} at the beginning (t = 0) and 1.76×10^{9} at the end (t = 180 min). Dividing the glucose uptake rate by the number of cells gives the results in Table 2 (“measured”).

Table 3-2. Glucose uptake rates for a single cell, in molecules/sec.

Time	For MM		For LB	
	measured	calculated upper bound	measured	calculated upper bound
0 min	2.03×10^{7}	6.02×10^{19}	3.20×10^{7}	7.17×10^{19}
180 min	3.95×10^{6}	3.52×10^{19}	6.18×10^{6}	3.27×10^{19}

For comparison we calculate the rate of glucose molecules impinging on the surface of a single bacterium. We assume that 1/6 the molecules within 1 mean free path of the surface jump to the surface, and multiply this number by the number of jumps per second to get the rate at which molecules reach the surface. The factor of 1/6 comes because there are 6 possible directions a glucose molecule can jump, only one of which is favorable. The mean free path λ may be obtained from the Einstein-Smoluchowski equation, which relates the diffusion coefficient D to the parameters used in the formulations of a random walk model.[146-149]

$$D = \lambda^2 / 2\tau \qquad (3\text{–}3)$$

Where τ is the average time between jumps. For glucose in water we estimate λ as the diameter of a water molecule, = $2.5\text{x}10^{-8}$ cm, and D=$6.7\text{x}10^{-6}$ cm^2/sec, so $\tau = 4.66\text{x}10^{-11}$ sec. The rate at which glucose molecules in solution reach the surface of a cell is therefore

$$A(2.5\times10^{-8}\text{cm}/6)\times c/(4.66\times10^{-11}\text{sec}) = (89.4\ \text{cm/sec})Ac \qquad (3\text{-}4)$$

where A is the cell surface area and c is the concentration.

For NC, assuming spheres with cell volume of 0.65 μm^3, we calculate a radius of 0.537 µm and A = $3.63\text{x}10^{-8}$ cm^2. The rate at which glucose molecules strike the surface of one cell is thus $3.24\text{x}10^{-6}$c cm^3/sec. The value of c at time 0 is $6.02\text{x}10^{19}$ molecules/cm^3 for MM and $7.17\text{x}10^{19}$ molecules/cm^3 for LB. At 180 min, c is $3.52\text{x}10^{19}$ molecules/cm^3 for MM and $3.27\text{x}10^{19}$ molecules/cm^3 for LB. These numbers are used to obtain the “calculated” rates in Table 2. These rates are upper bounds to the rate at which glucose molecules enter a cell, since most of the molecules striking the surface do not stick, and most of those that stick cannot enter. In fact, the rate of glucose consumption is orders of magnitude smaller than the rate of glucose arrival at the surface. We were not able to find any comparable measurement of the rate of glucose consumption in the literature.[150]

3.3.5. Growth Curves

Bacterial cultures are often studied in the context of a life cycle and therefore growth curves are important. In assessing the utility of the BSN approach, we produced 27 complete growth curves in two different media and also performed experiments with various perturbations. A standard growth curve, as described in the Experimental Procedure, produces a series of Raman spectra that can be analyzed quantitatively and qualitatively as shown individually in Figure 3-9 and averaged together in Figure 3-10.

BSN was used to follow cultures that were inoculated with NC. Tracking with OD600 measurements every 30 minutes showed that the bacteria volume fractions calculated by BSN correlated well with OD600. In addition, the LB v/v was seen to decrease rapidly initially and then to decrease slowly. For short times these results resemble the linear addition of NC into LB with a biofilm present as shown in Figure 3-5, but for a growth curve the decrease in LB does not level off in 30 minutes. For a growth curve the initial rapid decrease continues throughout the observation time.

The growth curves started with average OD600=0.142 AU σ= 0.011 and were terminated after 24 hours with average OD600=0.733 AU σ= 0.022. In each case a biofilm was produced that could affect the measured OD by at most 0.04.[20] The algorithm was applied to the growth curve data (IE and EE) to determine the v/v of NC and LB (Figure 3-9). Variation in the starting point of the growth curve is attributed to 1) variation in the initial concentration of NC and 2) variation in the position of the liquid surface in the cuvette.

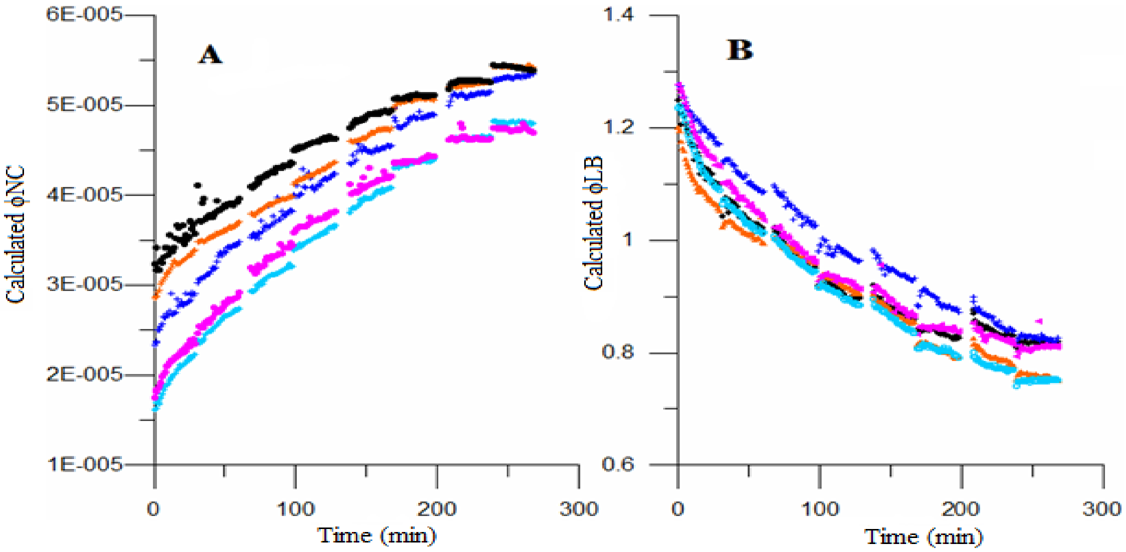

Figure 3-9. A) Calculated ϕ_{NC} and B) ϕ_{LB} for five growth curves, using the algorithm. Results for growth curves 5, 6, 7, 8 and 9 are, respectively, blue-green, violet, blue, orange, and black. These are representative of the variation in the full set of 20 produced under identical conditions. The starting OD600, averaged over the 5 curves shown, was 0.14 AU with $\sigma = 0.011$; at 270 min the average OD600 was 0.733 AU with $\sigma = 0.022$. Temperature for all growth curves was 37°C.

The linear region observed in Figure 3-9A extends to a calculated ϕ_{NC} of 0.42×10^{-4} v/v≈0.420 AU OD600 which is slightly higher than that in the training set. This difference may be attributed to differences in cuvette height or liquid level between the growth curves and the training set. We note that the general shape and curvature of the plots of LB and NC concentrations vs. time are quite reproducible.

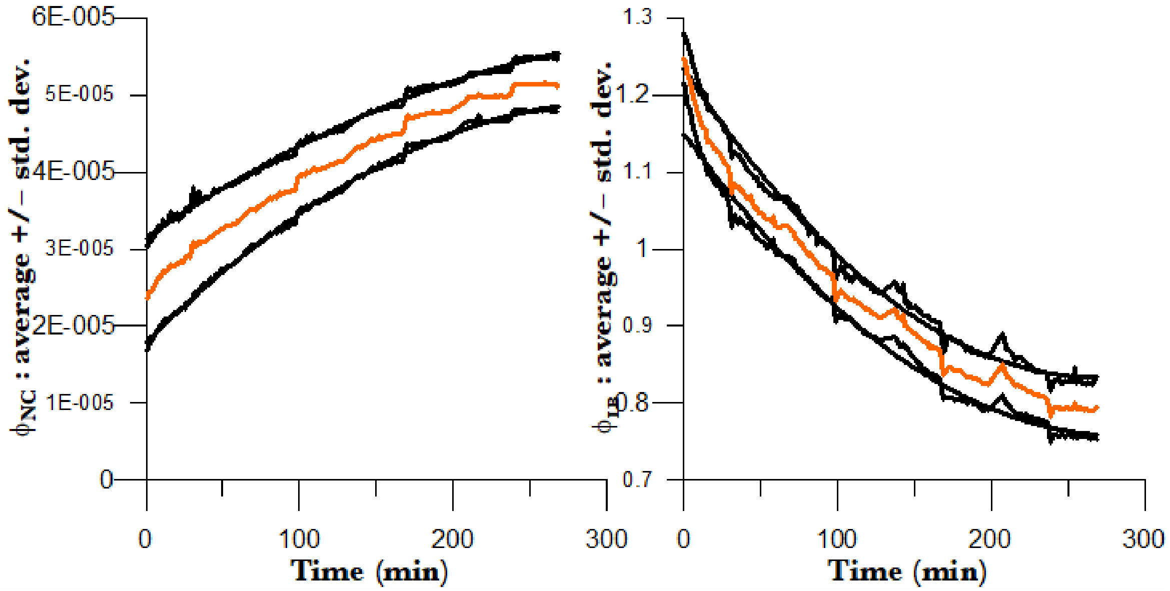

Figure 3-10. Average volume fractions of NC and LB for the five growth curves of Figure 3-9. The average is shown in orange. The black curves are ±1 σ. Parabolic fits to these two are also shown.

Experiments were also performed at ±5°C from the optimal temperature of 37°C (Figure 3-11). The calculated ϕ_{NC} for the growth curve at 42°C starts at a relatively high value, which may reflect back scattering caused by bubbles at the surface (Figure 3-10A). The growth curve at 32°C is similar to growth curves at optimal temperature (Figure 3-10A). Figure 3-10B shows calculated ϕ_{LB} which behaves similarly to growth curves at optimal temperature (Figure 3-10A). The variation in the liquid level of the cultures due to evaporation is particularly evident for the 42°C culture.

Also, the shape of the curves seems to change with temperature within the relatively narrow range of the starting NC concentrations sampled. Whereas the starting LB concentration is constant to within 5%, the starting NC concentration varies by more than a factor of 2. In fact, the final NC concentration varies less than the starting NC and the final LB varies more. The final OD600 for the 37°C curves was nearly a factor of 2 larger than all the others suggesting the possibility of some kind of artifact e.g. biofilm production is different at 37°C than at the other temperatures.

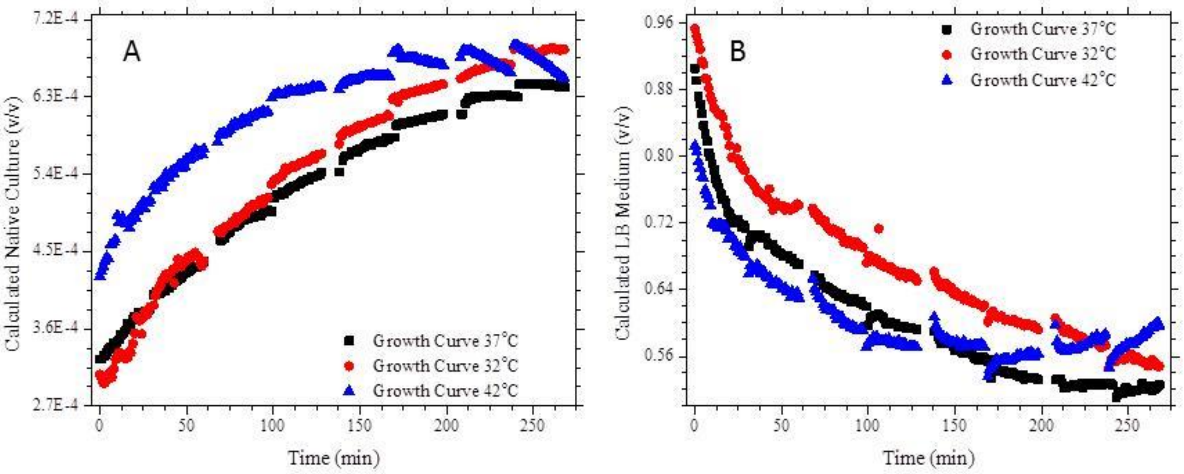

Figure 3-11. Calculated volume fractions of NC (panel A) and LB (panel B) for growth curves at three temperatures. Curve at 37°C has starting OD600=0.068, final OD600=0.793. Curve 32°C has starting OD600=0.054, final OD600=0.491. Curve at 42°C has starting OD600=0.057, final OD600=0.419.

Aliquots of LB must be added during these growth curves in order to maintain the volume of the culture, and their effect is evident in Figure 3-11, especially at the highest temperature. We found that replacing one of the aliquots with an aliquot of glucose reproducibly produced a visible increase in the growth rate of NC (Figure 3-12). A leveling off of the LB decrease rate is also observed. Since glucose is one of the primary nutrients that NC utilizes for energy, it makes sense that an increase in the abundance of glucose causes an increase in growth.[151] Also, glucose perhaps is a preferred nutrient over LB until at least some amount of free glucose is consumed.

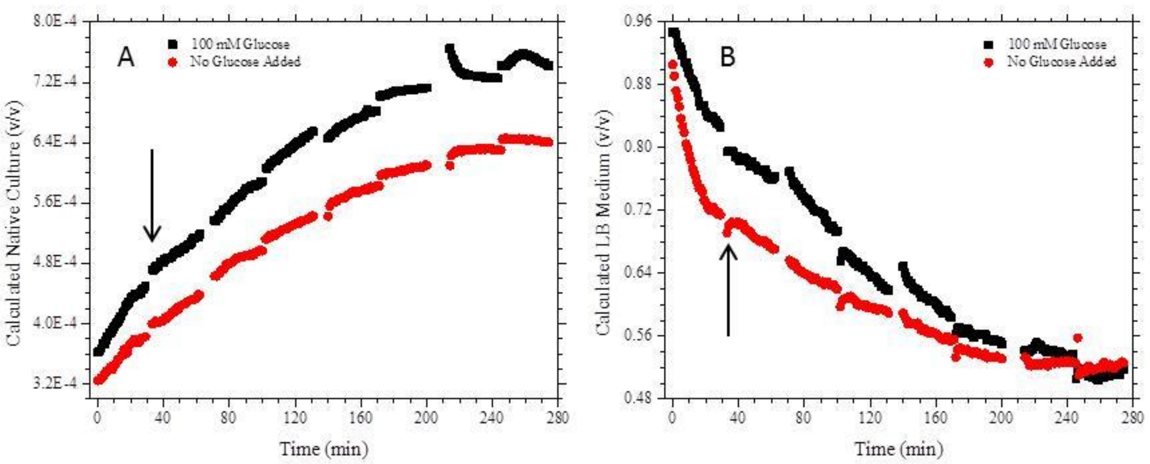

Figure 3-12. (A) Calculated NC for growth curves with and without addition of glucose. (B) Calculated LB for growth curves with and without addition of glucose. Note the increase in the growth rate of NC with the addition of 25 μL of 7 M glucose into the culture (becomes 100 mM once diluted into the culture) at 30 min as indicated by arrow and a decrease in the growth rate of LB.

Finally, since visual inspection of the Raman spectra revealed only minor differences across all the experiments, Principal Component Analysis (PCA) of the 101-7 baseline-corrected LB spectra was used to search for the main contribution(s) to the observed Raman spectra. Figure 3-13 to Figure 3-15 show the results for growth curves with added glucose (Figure 3-14), d-glucose (Figure 3-15) and no glucose (Figure 3-13).

In each PCA related Figure that follows, the graph at the upper left is a Scree plot, which shows the sum of squared deviations between the experimental spectra and the weighted sums of the first n principal components, as a function of n. Each sum of squared deviations has been normalized by dividing by the sum of squared deviations for n = 1. (It should be noted that the sum for n = 1 is typically less than 1% of the sum of squared values of the spectra themselves.) In each case the 3 most important components for each data set accounts for 64.1%, 57.5%, and 64.0% of the total sum of squares of deviations for glucose, d-glucose, and no glucose respectively. For each data set 3 components represent the spectra almost equally well. The presence of deuterium has the potential of making vibrational spectra more complex. That is, introducing some deuterium in addition to the protonated forms should cause the sheer number of Raman features increase relative to the pure nondeuterated analogue.

The graph at the upper right in each PCA Figure shows the coefficients corresponding to the three most important components as functions of time t, where t= 0 is the time of addition of glucose or d-glucose. The last three graphs show the vectors i.e. the spectra corresponding to these first three principal components. The coefficients relate to the raw spectra and the covariance matrix derived from that data with no correction for turbidity. The behavior of the coefficients is therefore also affected by the variable turbidity of the culture over time.

The most significant principal component, i.e. component 1, is similar for all cultures we have analyzed, including those shown here. This suggests that this component corresponds to cellular material, which is supported by the observation that, in every growth curve, the coefficient of this component increases with time. Since MM contains no added protein, the large feature near 1660 cm^{-1} present in all the spectra is mostly water. Glucose cannot be the main contributor to component 1 given the absence of a peak at 1127 cm^{-1}.

Comparing the components of the MM supported culture versus the LB cultures, we see features in MM that are either not present or discernable in LB, perhaps because of less spectral congestion. For example, not visible in spectra of LB supported cultures, we have a Raman feature at about 958 cm^{-1} consistent with added phosphate in MM. Also, in component 3 there is a well-defined feature at about 1127 cm^{-1} that could be associated with glucose. The coefficient for this component behaves correctly in terms of the timing of added glucose as well. Note that added d-glucose produces a similar variation in component 3 for the associated spectra but the vector for component 3 does not contain a similar feature, possibly because that feature is in fact altered by deuteration.

Simple assignment of spectral features within a vector to specific molecules may be problematic. Because the concentrations of chemical species in reactive mixtures vary in time at fixed stoichiometric ratios, and equilibrium constants impose similar “constraints” on the concentrations of species that lead to observable Raman features, a single principal component produced by the PCA process is expected to reflect features of all the linearly related Raman features. We have produced simulations that reflect this expectation, consistent with the chemometric literature[152], that a single PCA component can contain features from more than one chemical species, when their concentrations are so mutually constrained. With this in mind we also note that overall metabolism involves catabolism and anabolism and a reshuffling of the chemical bonds should be expected. Clearly, more studies are needed to provide definitive answers to these issues but these particular sets of spectra were included to demonstrate the kinds of information that may be accessible by monitoring bacterial cultures using Raman spectroscopy, with and without using BSN.

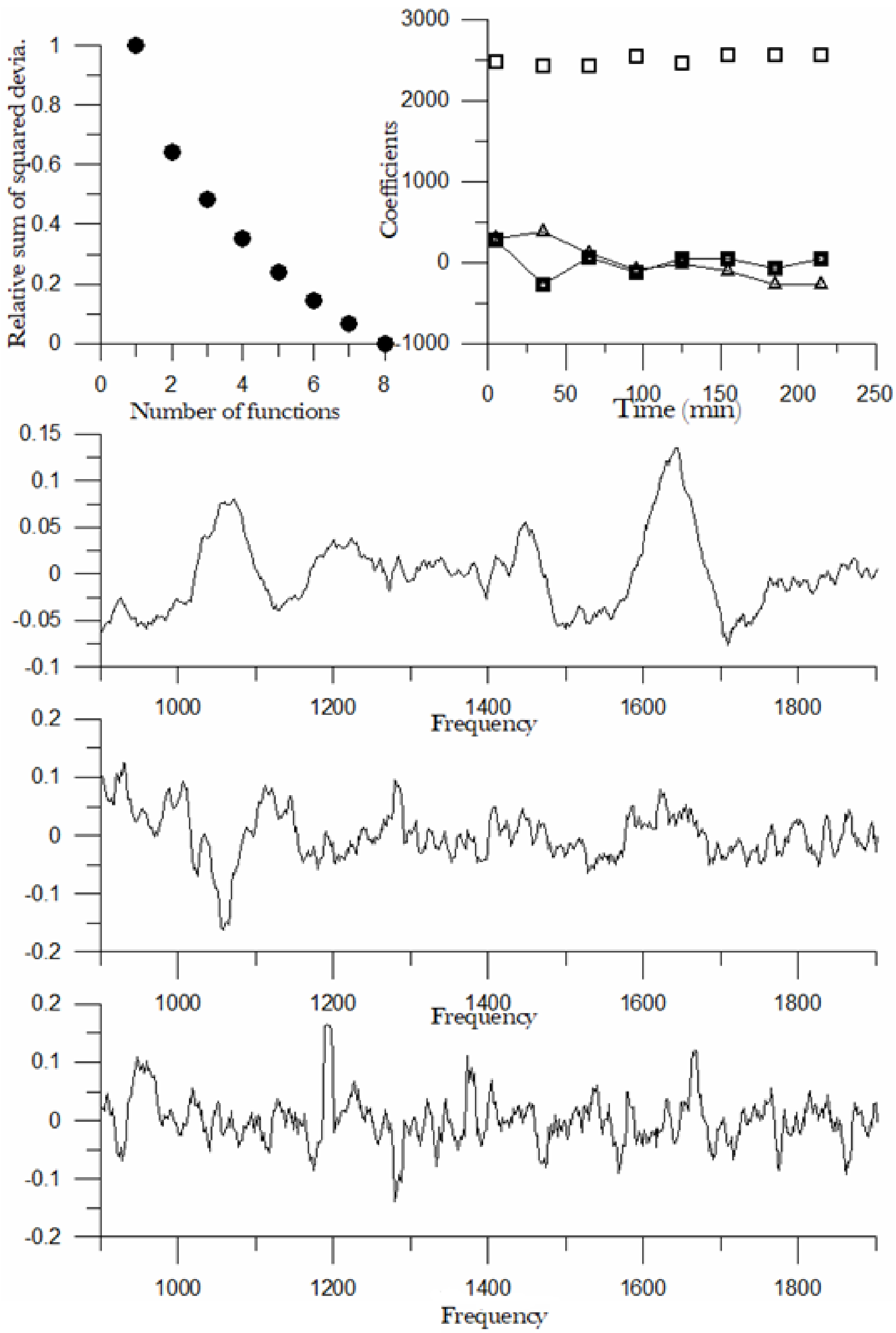

Figure 3-13. Results of Principal Component Analysis applied to a LB supported growth curve with no added glucose. Upper left: sum of squared deviations between spectra and fits using the first n principal components, divided by the sum for n = 1. Upper right: coefficients of the first three components as functions of time (light squares = 1st component, heavy triangles = 2nd component, heavy squares = 3rd component). Third, fourth, and fifth plots: spectra of the 1st, 2nd, and 3rd principal components.

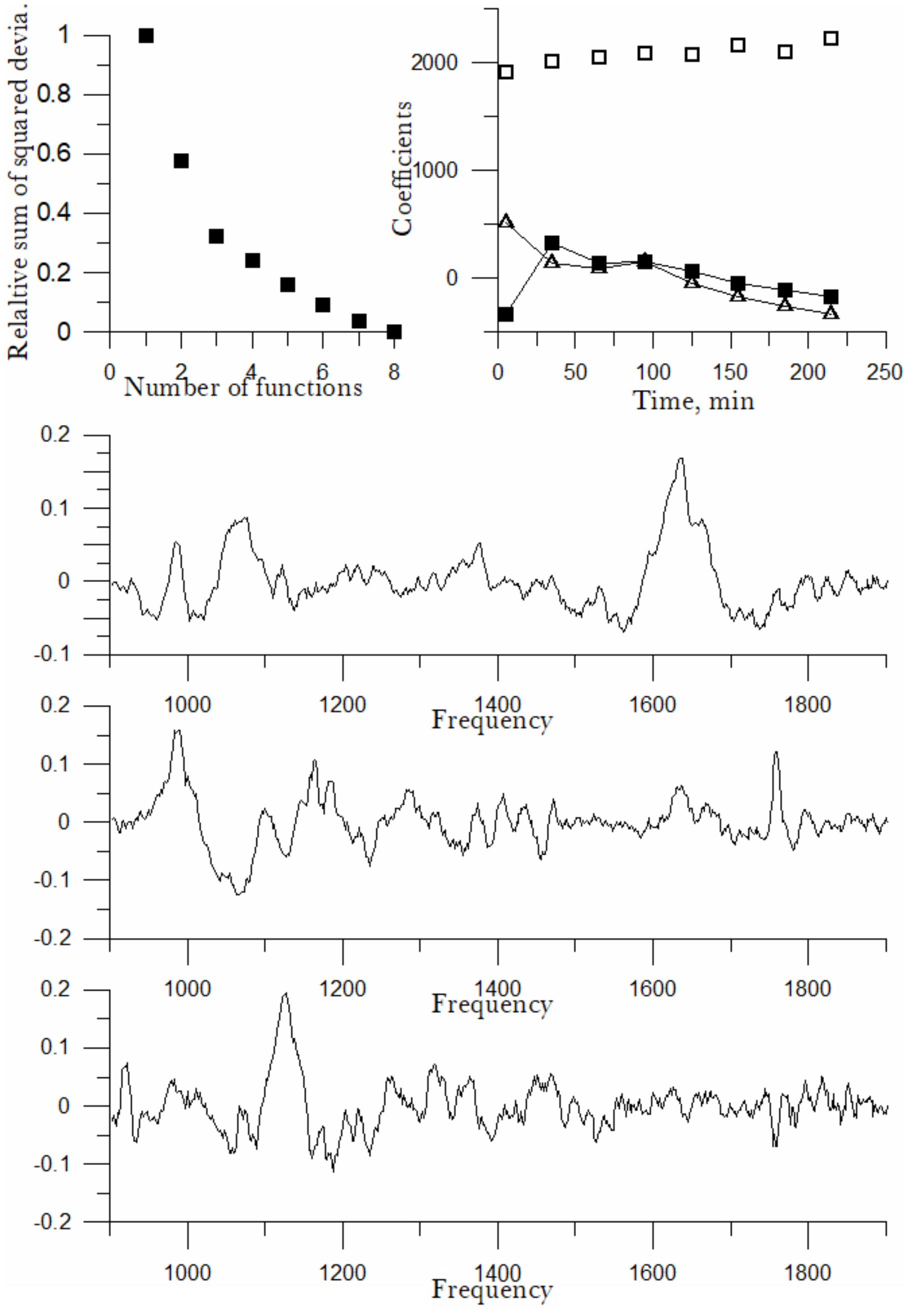

Figure 3-14. Results of Principal Component Analysis applied to a growth curve with glucose added at t = 0. Upper left: sum of squared deviations between spectra and fits using the first n principal components, divided by the sum for n = 1. Upper right: coefficients of the first three components as functions of time (light squares = 1st component, heavy triangles = 2nd component, heavy squares = 3rd component). Third, fourth, and fifth plots: spectra of the 1st, 2nd, and 3rd principal components.

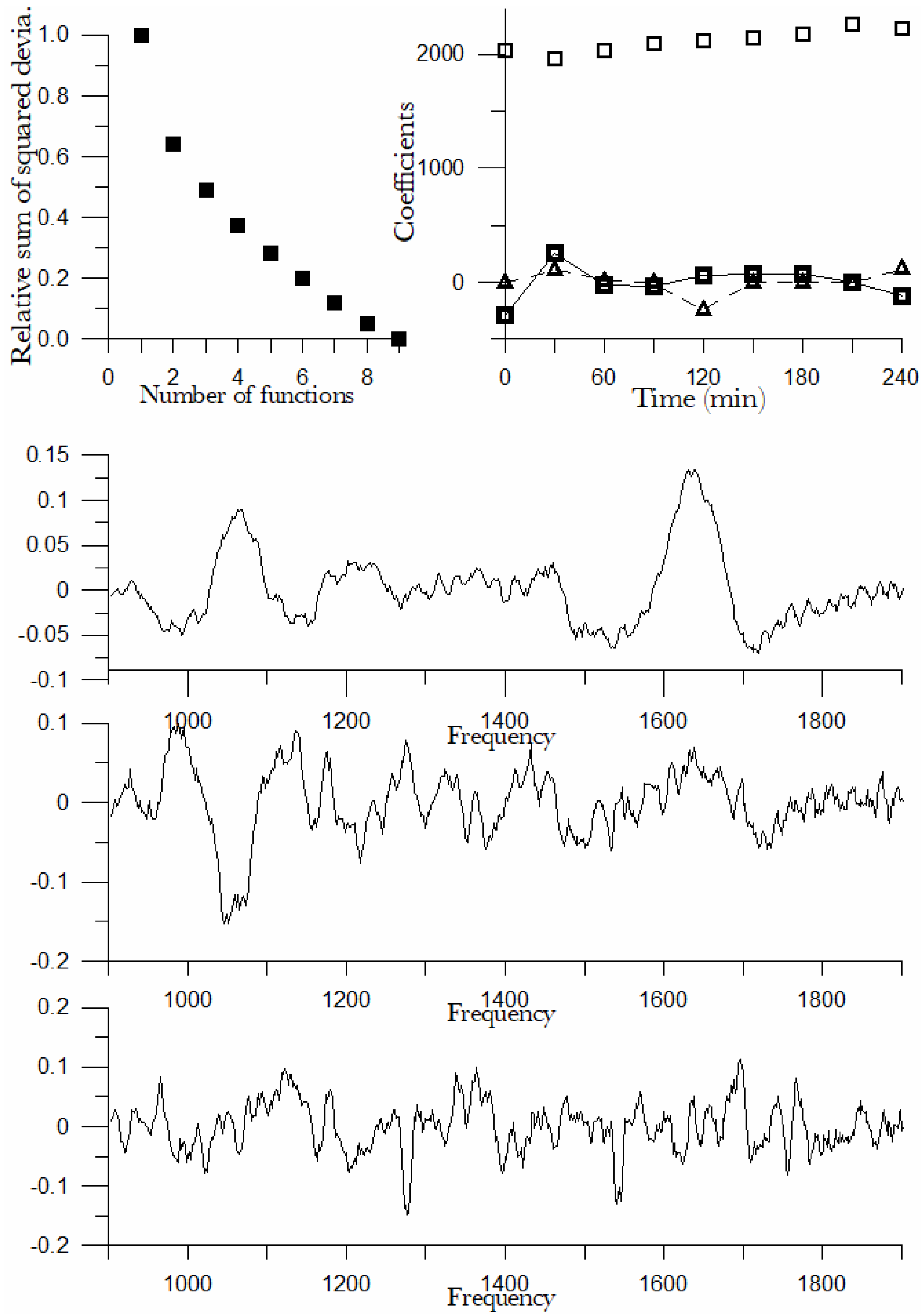

Figure 3-15. Results of Principal Component Analysis applied to a LB growth curve with d-glucose added at t= 0. Upper left: sum of squared deviations between spectra and fits using the first n principal components, divided by the sum for n = 1. Upper right: coefficients of the first three components as functions of time (light squares = 1st component, heavy triangles = 2nd component, heavy squares = 3rd component). Third, fourth, and fifth plots: spectra of the 1st, 2nd, and 3rd principal components.

Thus, the second and third components would seem to contain glucose or d-glucose as well as other substances used by the cells to produce biomatter. This is shown by the fact that their coefficients generally decrease with time, except for an initial uptick at t = 0, when glucose or d-glucose is added. (The decrease can be made more evident by linearly transforming the 2nd and 3rd components so as to make the coefficients as positive as possible; this is allowed since we always use linear combinations to represent the actual spectra.) Because of spectral congestion, possible signal to noise differences across the spectral range for all spectra, the fact that we do not have good spectra below 950 cm^{-1}, and perhaps the variety of environments for glucose binding, the full spectrum of aqueous glucose does not appear in the components.

3.4. Discussion

The purpose of this study was to explore the applicability of modern spectroscopic technology to the noninvasive, *in vivo* real-time study of bacterial cultures and similar mildly turbid systems. The BSN algorithm is an improvement on OD600 in several ways. It offers the potential to simultaneously, continuously and noninvasively monitor two culture parameters e.g. NC concentration and nutrient concentration. By itself, OD600 can give information only on the concentration of organisms and that information is rendered ambiguous by the potential presence of debris and other sources of turbidity in addition to the bacteria. Thus, BSN provides a more complete picture than OD600 of the response of the bacteria to 1) well-defined but not completely controllable variables like NC starting concentrations and 2) intentional perturbations like variations in temperature and nutrient type. The information given by BSN concerning legacy media like LB maybe helpful in discerning culture-induced modification(s) of the fluid environment even though it is not currently possible to assign Raman or other spectroscopic features associated with LB. Another advantage is that bacterial cultures can be studied more quickly and with greater flexibility, improving throughput and possibly increasing the rate of discovery, production and innovation. We here discuss mostly methodological issues and defer most discussion of the results concerning bacteria and cultures to future papers.

In the present work, we parametrized the BSN algorithm for mixtures of PBS, LB and NC, and applied the parametrized algorithm to growth curves. We showed how the calculated volume fractions of NC and LB change with time for five of these growth curves. We also showed that the calculated NC concentrations correlate with separate OD600 measurements. The average and standard deviations for these five curves are plotted in Figure 3-10. The standard deviation was roughly 25% of the mean in the NC vs. time average over 5 runs but it should be noted that the starting OD600 for the set varied by about 44%. Thus, the shape of the observed growth curves would seem to be reproducible independent of the starting OD and BSN would allow experiments in which several cultures were run in parallel to test e.g. some hypothesis that effects the bacterial growth rate.

To apply the BSN algorithm, EE and IE must be measured for a range of bacterial and media dilutions to assure that they are linearly related to concentrations. In this study, we found it easy to meet these requirements without extensive design and fabrication of specialized apparatus. This confirms that the EE and IE are produced and collected in the single scattering limit. Note that the calibration parameters a-f obtained from the bilinear fits are dependent on the excitation/collection geometry. The training set calibration lines comparing BSN-calculated NC and LB concentrations to the actual values have slopes of 1 and intercepts of 0 within experimental error. Thus, our present optical arrangement was adequate to demonstrate the applicability of BSN to bacterial cultures.

However, improvements in design and engineering for specific goals are possible. For example, monitoring the back reflection from the top surface of the liquid to drive a servo to keep the reflection constant would remedy the drift due to evaporation of the liquid over time. With attention to the artifacts revealed in this work, specialized apparatuses and procedures for BSN can be developed that can avoid these issues. Clearly, there will be differences in how BSN is used in cuvettes, 400,000 L bioreactors, 96-well plates and micro fluidic environments but many of the basic ideas and remedies for artifacts are anticipated here. It may also be possible to use the BSN approach in other situations, e.g. flow cytometry.

The determination of the rate of glucose consumption per organism has produced a plausible result although we were unable to find a value from the literature for direct comparison. We do not know of a single analytical approach that would produce both a NC concentration and glucose uptake rate in an internally consistent way. It is possible to use a blood glucometer to independently analyze the glucose in the medium, but this requires a separate calibration that may not be possible in LB medium due to the presence of other sugars and potentially interfering materials, making it much harder than the present method.

Our results suggest that, even after a lag period in which only LB (with no added glucose) was available for nutrition, this NC (E. coli) apparently immediately prefers glucose over all other nutrients present should it become available. Even if the bacteria adapt to the nutrients in LB during the lag phase, glucose is still the preferred source of carbon. In MM, glucose is the only carbon source present initially. Our results imply that NC consumes glucose more rapidly in MM than in LB. Thus we suspect that the carbon intake in LB involves other molecules e.g. amino acids that can be converted to glucose by gluconeogenesis.[153] It would be interesting to prepare a culture in lag phase using MM or lactate medium, and then replace the medium with LB to measure, using the technology described in this study, the resulting glucose uptake. This type of experiment and other phenotype/genotype comparisons would be facile using BSN.

The glucose consumption rates were obtained using a glucose Raman peak, without using multiple instruments and analytical tactics such as OD600 for NC density. Since there was no turbidity correction we refer to the estimates as bounds. It is possible to construct a training set using only the NC and glucose concentrations, e.g. in MM, and then the BSN algorithm would provide turbidity-corrected NC and glucose concentrations directly. This is the subject of future work in our lab.

3.5. Conclusion

The BSN algorithm can be applied to a variety of bacterial and other turbid systems i.e. cell cultures. Using the BSN algorithm can accurately determine the cell count in a culture without taking OD600 readings throughout the experiment. We have demonstrated that continuous, noninvasive monitoring in real time of biomass production and nutrient depletion for NC culture is possible in both LB and MM, using the 1060 cm^{-1} and 1120 cm^{-1} Raman features respectively. Using only the measurements required for BSN, we can estimate the rate of glucose consumption in an ordinary NC culture. The BSN algorithm provides a much more comprehensive picture of the chemical and physical state of bacterial cultures than OD600 alone.

CHAPTER 4

FUTURE DIRECTIONS

Raman spectroscopy can be used for applications such as medical and biological characterizations.[6, 8, 12, 15, 21, 154] Human tissues have been analyzed in real-time, great strides have been made in blood glucose analysis and even spinal cord analysis are all capable of being done using Raman spectroscopy. The research performed in this thesis lead to a new way of analyzing microorganisms and the biofilms they produce. Chapters 2 and 3 show how well this technique can be applied to physical measurements of biological cultures in aqueous solutions such as those encountered in the pharmaceutical industry, biomedical research, food chemistry or any industry using cells to create new compounds. I was able to observe the glucose peak trend down over time and account for an accurate rate of glucose consumption in a culture as shown in Chapter 3. There are many different paths budding from this research that should be pursued, and a couple of the most prominent ones will be highlighted in this chapter.

Following the work seen in Chapter 2 “Optical interference probe of biofilm hydrology”, I would plan to expand on this by using synthetic films. The goal is to determine the physical and chemical properties of these synthetic films in a similar manner to the way biofilms were studied in Chapter 2. Synthetic films involving biofilm-like materials are becoming more popular in the medical field, waste water treatment, filtration, and even some electrical applications.[47-54] Synthetic films are used as drug delivery devices, implants and even synthetic grafts. Unlike biofilms, synthetic films have the unique aspect of being customizable. Synthetic films could be layered with the same compound, alternating compounds, doped with metals to strengthen their structure, or even mix different synthetic compounds together to get different variations in properties.

Using the fringe analysis from Chapter 2, one could analyze the different thicknesses of the water layer in the synthetic films by variation in chemical composition. It would be interesting to see if a pure synthetic film or mixtures of synthetic films are able to retain more water over a predetermined length of time or which would dry out faster. We also observed “cracking” of a film when allowed to completely dry out (Figure 2-4). Developing a synthetic film to resist “cracking” whether it would be for medical applications or water treatment would add to the resilience/robustness of the film over time. Testing is required to determine what kind of synthetic film would be optimal for different applications, and what kinds of cross-linkages can be used as well. Once a better understanding of these films is accomplished, maximizing the efficiency of doping the films with biologics, stem cells and more could lead to an endless range of research.[155-157] A couple examples of these will be discussed in the following paragraphs.

Mapping out the location of the EC cells with a fluorescent tag (Figure 2-8) throughout the biofilm using a confocal fluorescence microscope allowed us to see where the cells congregated in the biofilm. Using the confocal fluorescence microscope could help us see the location of the cells in a synthetic film as well. With a synthetic film you can customize your films by making a layer, placing bacterial/mammalian/stem cells on that layer, apply another layer, placing more cells and so on allowing you to know exactly how thick and the location and number of cells throughout the layers of the film. It would be interesting to know if the microorganisms stay in the layer they were originally placed or if they would migrate to the center like in biofilms. Knowing the location of cells in a synthetic film is useful in some of the applications stated above and knowing where exactly to dope the synthetic film and how thick the synthetic film should be to provide adequate protection for the microorganisms/cells will prove to be very useful as well. Since we could control the number of cells being placed into a synthetic film, it would be interesting to see if we can obtain standardization for cell count in synthetic film and/or biofilms where the number of cells may not be predetermined. This would be a useful tool for the medical industry to accurately determine the number of cells in a specific layer/s of a synthetic film with stem cells and placing these films as a synthetic graft onto the human body. Testing could be done to potentially monitor the change in the stem cell density/location/orientation in real-time as they develop into the new cells and tissue intended for the patient or determine some of the chemicals produced in the process. This would require extensive testing and collaboration with researchers already doping synthetic films with stem cells due to their controlled nature.

Product production monitoring of a cell culture in real-time is a very useful application for Raman spectroscopy. Currently, the most common way to analyze product production from a culture is by HPLC. While this is a very accurate method of analysis, it requires the culture to be sampled and the sample is no longer recoverable. We have shown that Raman spectroscopy can be used to monitor a culture for a chemical being produced in real-time (provided it is Raman active) and there is no need to sample the culture. One could easily incorporate this into any bioreactor as a probe placed into the culture before or during inoculation. This would initially require comparison with HPLC in order to determine how accurate and reproducible the Raman data would be over the entire growth of a culture.

In Chapter 2 some of the physical characteristics of biofilms are determined which may help in leading to the knowledge required to disrupt these films. One goal is to test different chemicals in order to determine which chemical or mixture would be most effective in disrupting the complex polysaccharide matrix[55] that these biofilms produce. Hospitals and the food industry are two of the major organizations that could benefit from this kind of research. The primary linkage that needs to be disrupted is a glycosidic bond. There are many toxic chemicals that can effectively disrupt these linkages but are not safe to use on a person or to prevent leaching of toxic chemicals into food.

A continuation of the research in Chapter 3 could lead to studies using different types of microorganisms. We need to determine how many different types of microorganisms this technique can be applied to, now that we know it works on a couple different types. Yeast would be another route to explore since it is used in the fermentation process of alcohol, some medicinal products and food products.[158] Recently, yeast has been used to produce heme by porphyrin synthesis for vegan meat products. Mammalian cells/stem cells are used in medical research and being able to monitor these cultures in real-time without risk of contamination could have many added benefits. Those two examples only scratch the surface of large-scale applications this technique could be applied to which are of interest. One thing we have determined is that the BSN algorithm is very versatile and can be applied to many different turbid systems.

Brewing is an art form that will not be going away any time soon and must be monitored frequently to prevent contamination and maximize product production. Using Raman spectroscopy on bacterial cultures, as shown in Chapter 3, to monitor cell growth and nutrient depletion in real-time could assist in the optimization of the brewing process. Yeast reproduces by budding which could affect accurate cell count by multiple scattering off of the same yeast cell. Yeast also had an increase in the fluorescence in the Raman spectrum which made it more difficult to separate the Raman scattering from the fluorescence. Tests would need to be run and compared to cell counting and a hemocytometer which are the industry standard of analyzing number of yeast cells in a culture/slurry. In theory, the biomass peak could be optimized to reflect an accurate cell count for yeast similar to the way it was done for *E. coli*, but it will be more challenging than *E. coli* since ethanol is one of the products produced during the brewing process. Ethanol is Raman active and it should be possible to monitor its production throughout the brewing process using our technique.[159] The most prominent peak is around 880 cm^{-1} and would be the best to use provided no other peaks would interfere. It also has a peak around 1055 cm^{-1} which could interfere with the biomass peak at 1060 cm^{-1} making it even more difficult to get an accurate biomass reading. One could still use the Rayleigh line in order to get an accurate cell count since the elastic scattering would primarily come from the yeast cells. While there are many questions whether this will work, it could prove to be a useful tool in monitoring these types of cultures.

The final goal is to create a new device allowing biochemists to analyze their cultures quantitatively in real-time and more efficiently than current methods without the risk of contamination. This device could be incorporated into any bioreactor by simply adding an additional port with a built in Raman device. This would allow the analyst to determine the number density of cells, nutrient depletion and potentially chemical production in real-time. This real-time analysis for any biochemist would be vital information and allow for the maximization of cell growth with optimal product production.

REFERENCES

1. Skoog, D.A., F.J. Holler and S.R. Crouch, *Principles of instrumental analysis*. 2018.
2. Stuart, B.H., *Infrared Spectroscopy: Fundamentals and Applications*. 2004: Wiley.
3. Yi, P., P. Zhang, D. Zheng, X. Liu, T. Lin, H. Wang and Z. Xiao, *Using raman spectroscopy method for detecting pathogens in food [Machine Translation]*. 2017, Beijing Jiewei Technology Co., Ltd., Peop. Rep. China . p. 8pp.
4. Carey, P.R., G.R. Whitmer, M.J. Yoon, M.N. Lombardo, M. Pusztai-Carey, H. Heidari-Torkabadi and T. Che, *Measuring Drug-Induced Changes in Metabolite Populations of Live Bacteria: Real Time Analysis by Raman Spectroscopy.* J. Phys. Chem. B, 2018. **122**(24): p. 6377-6385.
5. Tian, H., N. Zhang, L. Tong and J. Zhang, *In Situ Quantitative Graphene-Based Surface-Enhanced Raman Spectroscopy.* Small Methods, 2017. **1**(6): p. n/a.
6. Sun, L., B. Chen, R. Gao, L. Yuan and W. Li, *Review on Raman spectroscopy application in food analysis.* Zhongguo Shipin Xuebao, 2012. **12**(12): p. 113-118.
7. Mignani, A.G., L. Ciaccheri, A.A. Mencaglia, R. Di Sanzo, S. Carabetta and M. Russo, *Dispersive Raman spectroscopy for the nondestructive and rapid assessment of the quality of southern Italian honey types.* J. Lightwave Technol., 2016. **34**(19): p. 4479-4485.
8. Martinez, J.C., J.R. Guzman-Sepulveda, G.R. Bolanoz Evia, T. Cordova and R. Guzman-Cabrera, *Enhanced Quality Control in Pharmaceutical Applications by Combining Raman Spectroscopy and Machine Learning Techniques.* Int. J. Thermophys., 2018. **39**(6): p. 1-13.
9. Liu, S. and G. Zhao. *Highly sensitive and selective sensing of estrogens in real sample using surface enhanced Raman spectroscopy*. 2018. American Chemical Society.
10. Lahr, R.H., *Advanced Applications of Raman Spectroscopy for Environmental Analyses*. 2013. p. 169 pp.
11. Hassing, S. *Boosting the amount of molecular information through polarized resolved resonance raman scattering*. 2017. InTech.
12. Farquharson, S., *Pharmaceutical applications of Raman spectroscopy: American pharmaceutical review's editorial advisory board column.* Am. Pharm. Rev., 2014. **17**(2): p. 32, 34-39.
13. Alvarez-Puebla, R.A. and L.M. Liz-Marzan, *Environmental applications of plasmon assisted Raman scattering.* Energy Environ. Sci., 2010. **3**(8): p. 1011-1017.
14. Afseth, N.K., M. Bloomfield, J.P. Wold and P. Matousek, *A novel approach for subsurface through-skin analysis of salmon using spatially offset Raman spectroscopy (SORS).* Appl. Spectrosc., 2014. **68**(2): p. 255-262.
15. Mosier-Boss, P.A., *Review on SERS of Bacteria.* Biosensors (Basel), 2017. **7**(4).
16. Efrima, S. and L. Zeiri, *Understanding SERS of bacteria.* J. Raman Spectrosc., 2009. **40**(3): p. 277-288.
17. Lyandres, O., J.M. Yuen, N.C. Shah, R.P. VanDuyne, J.T. Walsh, Jr. and M.R. Glucksberg, *Progress toward an in vivo surface-enhanced Raman spectroscopy glucose sensor.* Diabetes Technol. Ther., 2008. **10**(4): p. 257-265.
18. Efremov, E.V., F. Ariese and C. Gooijer, *Achievements in resonance Raman spectroscopy. Review of a technique with a distinct analytical chemistry potential.* Anal. Chim. Acta, 2008. **606**(2): p. 119-134.
19. McNay, G., D. Eustace, W.E. Smith, K. Faulds and D. Graham, *Surface-enhanced Raman scattering (SERS) and surface-enhanced resonance Raman scattering (SERRS): a review of applications.* Appl. Spectrosc., 2011. **65**(8): p. 825-837.

20. McDonough, R.T., H. Zheng, M.A. Alila, J. Goodisman and J. Chaiken, *Optical interference probe of biofilm hydrology: label-free characterization of the dynamic hydration behavior of native biofilms.* J. Biomed. Opt., 2017. **22**(3): p. 035003/1-035003/13.
21. Ivleva, N.P., P. Kubryk and R. Niessner, *Raman microspectroscopy, surface-enhanced Raman scattering microspectroscopy, and stable-isotope Raman microspectroscopy for biofilm characterization.* Anal. Bioanal. Chem., 2017. **409**(18): p. 4353-4375.
22. Lin, K., Z. Wang, S. Ju and R. Zhang, *Based on removing spectral raman spectroscopy fluorescence background subtraction method [Machine Translation]*. 2018, Xidian University, Peop. Rep. China . p. 11pp.
23. Cadusch, P.J., M.M. Hlaing, S.A. Wade, S.L. McArthur and P.R. Stoddart, *Improved methods for fluorescence background subtraction from Raman spectra.* J. Raman Spectrosc., 2013. **44**(11): p. 1587-1595.
24. Whitaker, D.A. and K. Hayes, *A simple algorithm for despiking Raman Spectra.* ChemRxiv, Anal. Chem., 2018: p. 1-6.
25. Ryabchykov, O., T. Bocklitz, A. Ramoji, U. Neugebauer, M. Foerster, C. Kroegel, M. Bauer, M. Kiehntopf and J. Popp, *Automatization of spike correction in Raman spectra of biological samples.* Chemom. Intell. Lab. Syst., 2016. **155**: p. 1-6.
26. Beier, B.D. and A.J. Berger, *Method for automated background subtraction from Raman spectra containing known contaminants.* Analyst (Cambridge, U. K.), 2009. **134**(6): p. 1198-1202.
27. Dent, P., B. Deng, J. Goodisman and J. Chaiken, *Coupled turbidity and spectroscopy problems: a simple algorithm for the volumetric analysis of optically thin or dilute two-phase systems.* Appl. Spectrosc., 2015. **69**(3): p. 377-388.
28. Chaiken, J., W.F. Finney, X. Yang, P.E. Knudson, K.P. Peterson, C.M. Peterson, R.S. Weinstock and D. Hagrman, *Progress in the noninvasive in-vivo tissue-modulated Raman spectroscopy of human blood.* Proc. SPIE-Int. Soc. Opt. Eng., 2001. **4254**(Biomedical Diagnostic, Guidance, and Surgical-Assist Systems III): p. 216-227.
29. Small, G.W., *Chemometrics and near-infrared spectroscopy: Avoiding the pitfalls.* TrAC, Trends Anal. Chem., 2006. **25**(11): p. 1057-1066.
30. Otto, M., *Chemometrics: Statistics and Computer Application in Analytical Chemistry*. 2007: Wiley.
31. Lavine, *Chemometrics.* Anal Chem, 2000. **72**(12): p. 91R-97R.
32. Kramer, R., *Chemometric Techniques for Quantitative Analysis*. 1998: CRC Press.
33. Chau, F.T., Y.Z. Liang, J. Gao and X.G. Shao, *Chemometrics: From Basics to Wavelet Transform*. 2004: Wiley.
34. Santos, R.B., B. Chandrasekar, M.K. Mandal, F. Kaschani, M. Kaiser, L. Both, R.A.L. van der Hoorn, A. Schiermeyer and R. Abranches, *Low Protease Content in Medicago truncatula Cell Cultures Facilitates Recombinant Protein Production.* Biotechnol. J., 2018: p. Ahead of Print.
35. Koch, A.L., *Turbidity measurements of bacterial cultures in some available commercial instruments.* Anal. Biochem., 1970. **38**(1): p. 252-9.
36. Jia, X., Y. Liu, C. Li and L. Huang, *Optimum growth conditions of klebsiella peneumoniae for degradation of petroleum contaminants and tolerability research methods [Machine Translation]*. 2016, Tianjin University, Peop. Rep. China . p. 8pp.
37. Weiss, D.J. and M.J. Wilkerson. *Flow cytometry*. 2010. Wiley-Blackwell.
38. Freer, G. and L. Rindi, *Intracellular cytokine detection by fluorescence-activated flow cytometry: Basic principles and recent advances.* Methods (Amsterdam, Neth.), 2013. **61**(1): p. 30-38.
39. Adan, A., G. Alizada, Y. Kiraz, Y. Baran and A. Nalbant, *Flow cytometry: basic principles and applications.* Crit. Rev. Biotechnol., 2017. **37**(2): p. 163-176.

40. Howell, M., J.J. Daniel and P.J.B. Brown, *Live cell fluorescence microscopy to observe essential processes during microbial cell growth.* J. Visualized Exp., 2017(129): p. e56497/1-e56497/10.
41. Kim, S.I., H.J. Kim, H.-J. Lee, K. Lee, D. Hong, H. Lim, K. Cho, N. Jung and Y.W. Yi, *Application of a non-hazardous vital dye for cell counting with automated cell counters.* Anal. Biochem., 2016. **492**: p. 8-12.
42. Chen, A., M. Leith, R. Tu, G. Tahim, A. Sudra and S. Bhargava, *Effects of diluents on cell culture viability measured by automated cell counter.* PLoS One, 2017. **12**(3): p. e0173375/1-e0173375/13.
43. Timmaraju, V.A., P.A.S. Theophilus, K. Balasubramanian, S. Shakih, D.F. Luecke and E. Sapi, *Biofilm formation by Borrelia burgdorferi sensu lato.* FEMS Microbiol. Lett., 2015. **362**(15): p. fnv120/1-fnv120/11.
44. Raja Sekharan, T., *Biofilm-a review.* World J. Pharm. Res., 2017. **6**(7): p. 1778-1790.
45. Berhe, N., Y. Tefera and T. Tintagu, *Review on biofilm formation and its control options.* Int. J. Adv. Res. Biol. Sci., 2017. **4**(8): p. 122-133.
46. Ur, R.S., P.G. Casey, C. Hill, M. Tangney, C.G.M. Gahan, R.S. Ur, C. Hill, C.G.M. Gahan, R.S. Ur, M. Stanton, M. Tangney, A. Spagnuolo, G. Bensi, K.P. Francis, M. Tangney, C.G.M. Gahan and C.G.M. Gahan, *Development of a Click Beetle Luciferase Reporter System for Enhanced Bioluminescence Imaging of Listeria monocytogenes: Analysis in Cell Culture and Murine Infection Models.* Front Microbiol, 2017. **8**: p. 1797.
47. Zhang, H. and J. Zhang, *Organic-inorganic composite film for seawater desalination or wastewater treatment, manufacture method, and application*. 2018, Nanjing Ounayi Organic Optoelectronics Co., Ltd., Peop. Rep. China . p. 9pp.
48. Lan, S., J. Qiu and M. Zhang, *Preparation method of photocatalytic sewage treatment composite membrane*. 2018, Dongguan Shigu Sewage Disposal Co., Ltd., Peop. Rep. China . p. 5pp.
49. Chen, M., Y. Xiao and M. Zhang, *Semiconductor film photocatalyst material for wastewater treatment and preparation method thereof*. 2018, Guangdong University of Technology, Peop. Rep. China . p. 9pp.
50. Baysal, G. and B.Y. Celik, *Synthesis and characterization of antibacterial bio-nano films for food packaging.* J. Environ. Sci. Health, Part B, 2018: p. Ahead of Print.
51. Aminzare, M., M. Hashemi, H. Hassanzadazar, E. Amiri and Z. Abbasi, *Antibacterial activity of corn starch films incorporated with Zataria multiflora and Bonium persicum essential oils.* Annu. Res. Rev. Biol., 2017. **19**(1): p. ARRB.37103/1-ARRB.37103/9.
52. Zhen, W. and L. Zheng, *Pol (lactic acid)-modified graphene oxide nanocomposite material, and its preparation method and application for medical material, food package material or agricultural film or fiber*. 2018, Xinjiang University, Peop. Rep. China . p. 14pp.
53. El Sayed, A.M. and A.D.M. Mohamad, *Synthesis, structural, thermal, optical and dielectric properties of chitosan biopolymer; influence of PVP and α-Fe2O3 Nanorods.* J. Polym. Res., 2018. **25**(8): p. 1-14.
54. Yang, M., Y. Wang, R. Cai, G. Tao, H. Chang, C. Ding, H. Zuo, H. Shen, P. Zhao and H. He, *Preparation and characterization of silk sericin/glycerol films coated with silver nanoparticles for antibacterial application.* Sci. Adv. Mater., 2018. **10**(6): p. 761-768.
55. Song, X., Y.-X. Xia, Z.-D. He and H.-J. Zhang, *A Review of Natural Products with Anti-Biofilm Activity.* Curr. Org. Chem., 2018. **22**(8): p. 789-817.
56. Donlan, R.M., *Biofilms: microbial life on surfaces.* Emerg Infect Dis, 2002. **8**(9): p. 881-90.
57. Vu, B., M. Chen, R.J. Crawford and E.P. Ivanova, *Bacterial extracellular polysaccharides involved in biofilm formation.* Molecules, 2009. **14**(7): p. 2535-2554.
58. Mah, T.-F.C. and G.A. O'Toole, *Mechanisms of biofilm resistance to antimicrobial agents.* Trends Microbiol., 2001. **9**(1): p. 34-39.

59. Born, M., E. Wolf and A.B. Bhatia, *Principles of Optics: Electromagnetic Theory of Propagation, Interference and Diffraction of Light*. 2000: Cambridge University Press.
60. Buning-Pfaue, H., *Analysis of water in food by near infrared spectroscopy.* Food Chem., 2003. **82**(1): p. 107-115.
61. Tonova, D., A. Paneva and B. Pantchev, *Determination of refractive index profiles of gradient optical waveguides by ellipsometry.* Opt. Commun., 1998. **150**(1-6): p. 121-125.
62. Todorov, R., A. Paneva and K. Petkov, *Optical characterization of thin chalcogenide films by multiple-angle-of-incidence ellipsometry.* Thin Solid Films, 2010. **518**(12): p. 3280-3288.
63. Jenkins, T.E., *Multiple-angle-of-incidence ellipsometry.* J. Phys. D: Appl. Phys., 1999. **32**(9): p. R45-R56.
64. Sultanova, N., S. Kasarova and I. Nikolov, *Dispersion properties of optical polymers.* Acta Phys. Pol., A, 2009. **116**(4): p. 585-587.
65. Malitson, I.H., *Interspecimen comparison of the refractive index of fused silica.* J. Opt. Soc. Am., 1965. **55**(10): p. 1205-9.
66. Prasad, P., G.S. Guru, H.R. Shivakumar and K. Sheshappa Rai, *Investigation on Miscibility of Sodium Alginate/Pullulan Blends.* J. Polym. Environ., 2012. **20**(3): p. 887-893.
67. Prakash, S.D.R., H.V. Ramakrishna, S.K. Rai and A.V. Rajulu, *Miscibility studies of sodium alginate/poly(vinyl alcohol) blend in water by viscosity, ultrasonic, and refractive index methods.* J. Appl. Polym. Sci., 2003. **90**(1): p. 33-39.
68. Mace, C.R., J. Barber, A. Laromaine Sague, G.M. Whitesides and R. Cademartiri, *Alginate hydrogel fibers, alginate hydrogel paper and related materials*. 2012, Harvard College, USA . p. 43pp.
69. Esteban, O., F. Marva and J.C. Martinez-Anton, *Optical constants of a sodium alginate polymer in the UV-vis range.* Opt. Mater. (Amsterdam, Neth.), 2009. **31**(4): p. 696-699.
70. Herzberg, G. and B.L. Crawford, *Infrared and Raman Spectra of Polyatomic Molecules.* The Journal of Physical Chemistry, 1946. **50**(3): p. 288-288.
71. Schmid, F.-X. *Biological macromolecules: UV-visible spectrophotometry*. 2007. John Wiley & Sons Ltd.
72. Beloin, C., A. Roux and J.M. Ghigo, *Escherichia coli biofilms.* Curr. Top. Microbiol. Immunol., 2008. **322**(Bacterial Biofilms): p. 249-289.
73. Scheiner, S. and M. Cuma, *Relative Stability of Hydrogen and Deuterium Bonds.* J. Am. Chem. Soc., 1996. **118**(6): p. 1511-21.
74. Tu, A.T., *Raman Spectroscopy in Biology: Principles and Applications*. 1982: Wiley.
75. McBain, A.J., *Chapter 4: In vitro biofilm models: an overview.* Adv Appl Microbiol, 2009. **69**: p. 99-132.
76. Kawarai, T., S. Furukawa, N. Narisawa, C. Hagiwara, H. Ogihara and M. Yamasaki, *Biofilm formation by Escherichia coli in hypertonic sucrose media.* J. Biosci. Bioeng., 2009. **107**(6): p. 630-635.
77. Coenye, T. and H.J. Nelis, *In vitro and in vivo model systems to study microbial biofilm formation.* J. Microbiol. Methods, 2010. **83**(2): p. 89-105.
78. Zogaj, X., M. Nimtz, M. Rohde, W. Bokranz and U. Romling, *The multicellular morphotypes of Salmonella typhimurium and Escherichia coli produce cellulose as the second component of the extracellular matrix.* Mol. Microbiol., 2001. **39**(6): p. 1452-1463.
79. Weber, H., C. Pesavento, A. Possling, G. Tischendorf and R. Hengge, *Cyclic-di-GMP-mediated signalling within the σS network of Escherichia coli.* Mol. Microbiol., 2006. **62**(4): p. 1014-1034.
80. Roemling, U., M.Y. Galperin and M. Gomelsky, *Cyclic di-GMP: the first 25 years of a universal bacterial second messenger.* Microbiol. Mol. Biol. Rev., 2013. **77**(1): p. 1-52.

81. Itoh, Y., J.D. Rice, C. Goller, A. Pannuri, J. Taylor, J. Meisner, T.J. Beveridge, J.F. Preston, III and T. Romeo, *Roles of pgaABCD genes in synthesis, modification, and export of the Escherichia coli biofilm adhesin poly-β-1,6-N-acetyl-D-glucosamine.* J. Bacteriol., 2008. **190**(10): p. 3670-3680.
82. O'Toole, G.A.G., Mahmoud A. , *INTRODUCTION TO BIOFILMS: CONCEPTUAL THEMES*. Microbial Biofilms, ed. O.T.G.e. In Ghannoum M. 2004, Washington, DC: ASM Press.
83. Mann, E.E. and D.J. Wozniak, *Pseudomonas biofilm matrix composition and niche biology.* FEMS Microbiol. Rev., 2012. **36**(4): p. 893-916.
84. Starkey, M., M.R. Parsek, K.A. Gray and S.I. Chang, *A Sticky Business: the Extracellular Polymeric Substance Matrix of Bacterial Biofilms*, in *Microbial Biofilms*. 2004, American Society of Microbiology.
85. Redfield, R.J., *Is quorum sensing a side effect of diffusion sensing?* Trends Microbiol., 2002. **10**(8): p. 365-370.
86. Costerton, J.W., Z. Lewandowski, D.E. Caldwell, D.R. Korber and H.M. Lappin-Scott, *Microbial biofilms.* Annu. Rev. Microbiol., 1995. **49**: p. 711-45.
87. Bakke, R. and P.Q. Olsson, *Biofilm thickness measurements by light microscopy.* Journal of Microbiological Methods, 1986. **5**(2): p. 93-98.
88. Zhang, T.C. and P.L. Bishop, *Density, porosity, and pore structure of biofilms.* Water Res., 1994. **28**(11): p. 2267-77.
89. Flygare, W.H., *Molecular Structure and Dynamics*. 1978: Prentice-Hall.
90. Poortinga, A.T., R. Bos, W. Norde and H.J. Busscher, *Electric double layer interactions in bacterial adhesion to surfaces.* Surf. Sci. Rep., 2002. **47**(1): p. 1-32.
91. Marliere, C. and S. Dhahri, *An in vivo study of electrical charge distribution on the bacterial cell wall by atomic force microscopy in vibrating force mode.* Nanoscale, 2015. **7**(19): p. 8843-8857.
92. Amsler, C.D., M. Cho and P. Matsumura, *Multiple factors underlying the maximum motility of Escherichia coli as cultures enter post-exponential growth.* J. Bacteriol., 1993. **175**(19): p. 6238-44.
93. Adler, J. and B. Templeton, *The effect of environmental conditions on the motility of Escherichia coli.* J. Gen. Microbiol., 1967. **46**(2): p. 175-84.
94. Mallepally, R.R., I. Bernard, M.A. Marin, K.R. Ward and M.A. McHugh, *Superabsorbent alginate aerogels.* J. Supercrit. Fluids, 2013. **79**: p. 202-208.
95. Zheng, H., I.V. Korendovych and Y.-Y. Luk, *Quantification of alginate by aggregation induced by calcium ions and fluorescent polycations.* Anal. Biochem., 2016. **492**: p. 76-81.
96. Sun, J. and H. Tan, *Alginate-based biomaterials for regenerative medicine applications.* Materials, 2013. **6**: p. 1285-1309.
97. Lee, K.Y. and D.J. Mooney, *Alginate: Properties and biomedical applications.* Prog. Polym. Sci., 2012. **37**(1): p. 106-126.
98. White, A.P., D.L. Gibson, S.K. Collinson, P.A. Banser and W.W. Kay, *Extracellular polysaccharides associated with thin aggregative fimbriae of Salmonella enterica serovar enteritidis.* J. Bacteriol., 2003. **185**(18): p. 5398-5407.
99. Sutherland, I.W., *The biofilm matrix. An immobilized but dynamic microbial environment.* Trends Microbiol., 2001. **9**(5): p. 222-227.
100. Rice, A.R., M.A. Hamilton and A.K. Camper, *Movement, replication, and emigration rates of individual bacteria in a biofilm.* Microb Ecol, 2003. **45**(2): p. 163-72.
101. Picioreanu, C., J.U. Kreft, M. Klausen, J.A.J. Haagensen, T. Tolker-Nielsen and S. Molin, *Microbial motility involvement in biofilm structure formation--a 3D modelling study.* Water Sci Technol, 2007. **55**(8-9): p. 337-43.

102. Notario, B., J. Pinto, E. Solorzano, J.A. de Saja, M. Dumon and M.A. Rodriguez-Perez, *Experimental validation of the Knudsen effect in nanocellular polymeric foams.* Polymer, 2015. **56**: p. 57-67.
103. Bagwell, C.E., S. Bhat, G.M. Hawkins, B.W. Smith, T. Biswas, T.R. Hoover, E. Saunders, C.S. Han, O.V. Tsodikov and L.J. Shimkets, *Survival in nuclear waste, extreme resistance, and potential applications gleaned from the genome sequence of Kineococcus radiotolerans SRS30216.* PLoS One, 2008. **3**(12): p. No pp. given.
104. Choi, M.H., S.-W. Jeong, H.E. Shim, S.-J. Yun, S. Mushtaq, D.S. Choi, B.-S. Jang, J.E. Yang, Y.J. Choi and J. Jeon, *Efficient bioremediation of radioactive iodine using biogenic gold nanomaterial-containing radiation-resistant bacterium, Deinococcus radiodurans R1.* Chem. Commun. (Cambridge, U. K.), 2017. **53**(28): p. 3937-3940.
105. Di Mario, R.J., M.C. Machingura, G.L. Waldrop and J.V. Moroney, *The many types of carbonic anhydrases in photosynthetic organisms.* Plant Sci. (Shannon, Irel.), 2018. **268**: p. 11-17.
106. Doi, Y., *L-lactate production from biodiesel-derived crude glycerol by metabolically engineered Enterococcus faecalis: cytotoxic evaluation of biodiesel waste and development of a glycerol-inducible gene expression system.* Appl Environ Microbiol, 2015. **81**(6): p. 2082-9.
107. Ferreira, E.A., C. da Conceicao de Matos, E.A. Barbosa, D.V. Silva, J. Barbosa dos Santos, G.A.M. Pereira, A.T. Faria and C. Teixeira da Silva, *Cassava physiological responses to the application of herbicides.* Semina: Cienc. Agrar., 2015. **36**(2): p. 645-656.
108. Friman, H., A. Schechter, Y. Nitzan and R. Cahan, *Phenol degradation in bio-electrochemical cells.* Int. Biodeterior. Biodegrad., 2013. **84**: p. 155-160.
109. Mandal, S., A.-M. Carey, J. Locsin, B.-R. Gao, J.C. Williams, J.P. Allen, S. Lin and N.W. Woodbury, *Mechanism of Triplet Energy Transfer in Photosynthetic Bacterial Reaction Centers.* J. Phys. Chem. B, 2017. **121**(27): p. 6499-6510.
110. Nguyen, N.H.A., R. Spanek, V. Kasalicky, D. Ribas, D. Vlkova, H. Rehakova, P. Kejzlar and A. Sevcu, *Different effects of nano-scale and micro-scale zero-valent iron particles on planktonic microorganisms from natural reservoir water.* Environ. Sci.: Nano, 2018: p. Ahead of Print.
111. Sarro, M.I., A.M. Garcia and D.A. Moreno, *Biofilm formation in spent nuclear fuel pools and bioremediation of radioactive water.* Int. Microbiol., 2005. **8**(3): p. 223-230.
112. Wang, J., *Engineered radiation-resistant bacteria and their application in bioremediation of radioactive waste-contaminated environment.* Fushe Yanjiu Yu Fushe Gongyi Xuebao, 2004. **22**(5): p. 257-260.
113. Fyrestam, J. and C. Oestman, *Determination of heme in microorganisms using HPLC-MS/MS and cobalt(III) protoporphyrin IX inhibition of heme acquisition in Escherichia coli.* Anal. Bioanal. Chem., 2017. **409**(30): p. 6999-7010.
114. Jiang, J., B. Wang, J. Li, B. Ye, S. Lin, W. Qian, L. Shan and T. Efferth, *Total coumarins of Hedyotis diffusa induces apoptosis of myelodysplastic syndrome SKM-1 cells by activation of caspases and inhibition of PI3K/Akt pathway proteins.* J. Ethnopharmacol., 2017. **196**: p. 253-260.
115. Bratbak, G. and I. Dundas, *Bacterial dry matter content and biomass estimations.* Appl Environ Microbiol, 1984. **48**(4): p. 755-7.
116. Loferer-Krossbacher, M., J. Klima and R. Psenner, *Determination of bacterial cell dry mass by transmission electron microscopy and densitometric image analysis.* Appl. Environ. Microbiol., 1998. **64**(2): p. 688-694.
117. Chaiken, J., J. Goodisman, B. Deng, R.J. Bussjager and G. Shaheen, *Simultaneous, noninvasive observation of elastic scattering, fluorescence and inelastic scattering as a monitor of blood flow and hematocrit in human fingertip capillary beds.* J. Biomed. Opt., 2009. **14**(5): p. 050505/1-050505/3.

118. Leth, I.K. and K.A. McDonald, *Media development for large scale Agrobacterium tumefaciens culture.* Biotechnol. Prog., 2017. **33**(5): p. 1218-1225.
119. Chelikani, R., F.H. Bacon and H. Yuan. *Overcoming the challenges of moving from hydrolysate-containing media to chemically defined media for a high cell density perfusion cell culture process*. 2017. American Chemical Society.
120. Hazeltine, L.B., K.M. Knueven, Y. Zhang, Z. Lian, D.J. Olson and A. Ouyang, *Chemically defined media modifications to lower tryptophan oxidation of biopharmaceuticals.* Biotechnol. Prog., 2016. **32**(1): p. 178-188.
121. Krajcovic, M., Y. Ilin, S. Hutchins, A. Borshchenko, W. Ahn, L. Tescione, D. Inlow and C. Lu. *What cells want vs. what cells need: Simplification of chemically defined media for optimal performance*. 2018. American Chemical Society.
122. Sublett, V., B. Cooper and J.O. Boles. *Use of enhanced chemically defined media to improve uptake of L-telluromethionine by Escherichia coli DL41(DE3)*. 2015. American Chemical Society.
123. Xu, J., M.S. Rehmann, X. Xu, C. Huang, J. Tian, N.-X. Qian and Z.J. Li, *Improving titer while maintaining quality of final formulated drug substance via optimization of CHO cell culture conditions in low-iron chemically defined media.* mAbs, 2018. **10**(3): p. 488-499.
124. Silver, J.A., *Frequency-modulation spectroscopy for trace species detection: theory and comparison among experimental methods. [Erratum to document cited in CA116(18):186796f].* Appl. Opt., 1992. **31**(24): p. 4927.
125. Silver, J.A., *Frequency-modulation spectroscopy for trace species detection: theory and comparison among experimental methods.* Appl. Opt., 1992. **31**(6): p. 707-17.
126. Deng, B., A. Simental, P. Lutz, G. Shaheen and J. Chaiken, *Singlet oxygen induced advanced glycation end-product photobleaching of in vivo human fingertip autofluorescence.* Proc. SPIE, 2012. **8219**(Biomedical Vibrational Spectroscopy V): p. 82190D/1-82190D/11.
127. Deng, B., C. Wright, E. Lewis-Clark, G. Shaheen, R. Geier, J. Chaiken and A. Mahadevan-Jansen, *Direct noninvasive observation of near infrared photobleaching of autofluorescence in human volar side fingertips in vivo.* Proc. SPIE, 2010. **7560**(Biomedical Vibrational Spectroscopy IV): p. 75600P/1-75600P/11.
128. Bae, K., W. Zheng and Z. Huang, *Quantitative assessment of spinal cord injury using circularly polarized coherent anti-Stokes Raman scattering microscopy.* Appl. Phys. Lett., 2017. **111**(6): p. 063704/1-063704/4.
129. Saxena, T., B. Deng, E. Lewis-Clark, K. Hoellger, D. Stelzner, J. Hasenwinkel, J. Chaiken and A. Mahadevan-Jansen, *Near infrared Raman spectroscopic study of reactive gliosis and the glial scar in injured rat spinal cords.* Proc. SPIE, 2010. **7560**(Biomedical Vibrational Spectroscopy IV): p. 75600I/1-75600I/12.
130. Saxena, T., B. Deng, D. Stelzner, J. Hasenwinkel and J. Chaiken, *Raman spectroscopic investigation of spinal cord injury in a rat model.* J. Biomed. Opt., 2011. **16**(2): p. 027003/1-027003/14.
131. Shen, J., L. Fan, J. Yang, A.G. Shen and J.M. Hu, *A longitudinal Raman microspectroscopic study of osteoporosis induced by spinal cord injury.* Osteoporos Int, 2010. **21**(1): p. 81-7.
132. Tamosaityte, S., R. Galli, E. Koch, G. Steiner, O. Uckermann, K.H. Sitoci-Ficici, R. Later, G. Schackert, M. Koch and M. Kirsch, *Inflammation-related alterations of lipids after spinal cord injury revealed by Raman spectroscopy.* J Biomed Opt, 2016. **21**(6): p. 61008.
133. Wang, S., Z. Liang, Y. Gong, Y. Yin, K. Wang, Q. He, Z. Wang and J. Bai, *Confocal Raman microspectral imaging of ex vivo human spinal cord tissue.* J. Photochem. Photobiol., B, 2016. **163**: p. 177-184.

134. Chester, T.L., J.J. Fitzgerald and J.D. Winefordner, *Theoretical comparison of the signal-to-noise ratios of Fourier transform spectrometry with single slit linear and slewed scan spectrometric methods for the photon noise limited situation.* Anal. Chem., 1976. **48**(4): p. 779-83.
135. J.D. Ingle Jr., S.R.C., *''Molecular Scattering Methods''. In: Spectrochemical Analysis*. 1988, Englewood Cliffs, NJ: Prentice-Hall.
136. Croce, A.C. and G. Bottiroli, *Autofluorescence spectroscopy and imaging: a tool for biomedical research and diagnosis.* Eur J Histochem, 2014. **58**(4): p. 2461.
137. Patterson, G.H. and D.W. Piston, *Photobleaching in two-photon excitation microscopy.* Biophys. J., 2000. **78**(4): p. 2159-2162.
138. Tu, A.T., *"Lipids and Biological Membranes" and "Carbohydrates" In: Raman Spectroscopy in Biology*. 1982, New York: John Wiley & Sons.
139. Mendelsohn, R., S. Sunder and H.J. Bernstein, *Deuterated fatty acids as Raman spectroscopic probes of membrane structure.* Biochim. Biophys. Acta, Nucleic Acids Protein Synth., 1976. **443**(3): p. 613-17.
140. Chaiken, J., W.F. Finney, C.M. Peterson, K.P. Peterson, P.E. Knudson, R.S. Weinstock and P. Lein, *Noninvasive in-vivo tissue-modulated near-infrared vibrational spectroscopic study of mobile and static tissues: blood chemistry.* Proc. SPIE-Int. Soc. Opt. Eng., 2000. **3918**(Biomedical Spectroscopy: Vibrational Spectroscopy and Other Novel Techniques): p. 135-143.
141. Bindal, S., V.K. Dagar, M. Saini, Y.P. Khasa and R. Gupta, *High level extracellular production of recombinant γ-glutamyl transpeptidase from Bacillus licheniformis in Escherichia coli fed-batch culture.* Enzyme Microb. Technol., 2018. **116**: p. 23-32.
142. Jira, J., B. Rezek, V. Kriha, A. Artemenko, I. Matolinova, V. Skakalova, P. Stenclova and A. Kromka, *Inhibition of E. coli growth by nanodiamond and graphene oxide enhanced by Luria-Bertani medium.* Nanomaterials, 2018. **8**(3): p. 140/1-140/13.
143. Ber, P., S.V. Trappen, P. Vandamme and J. Trcek, *Aeromicrobium choanae sp. nov., an actinobacterium isolated from the choana of a garden warbler.* Int J Syst Evol Microbiol, 2017. **67**(2): p. 357-361.
144. Zhu, S., J. Qiu, H. Wang, X. Wang, W. Jin, Y. Zhang, C. Zhang, G. Hu, J. He and Q. Hong, *Cloning and expression of the carbaryl hydrolase gene mcbA and the identification of a key amino acid necessary for carbaryl hydrolysis.* J. Hazard. Mater., 2018. **344**: p. 1126-1135.
145. Baumgart, L., W. Mather and J. Hasty, *Synchronized DNA cycling across a bacterial population.* Nat. Genet., 2017. **49**(8): p. 1282-1285.
146. Cicuta, P. and A.M. Donald, *Microrheology: a review of the method and applications.* Soft Matter, 2007. **3**(12): p. 1449-1455.
147. Felderhof, B.U., *Generalized Einstein relation for the mutual diffusion coefficient of a binary fluid mixture.* J. Chem. Phys., 2017. **147**(7): p. 074902/1-074902/9.
148. Islam, M.A., *Einstein-Smoluchowski diffusion equation: A discussion.* Phys. Scr., 2004. **70**(2-3): p. 120-125.
149. Ernst, M., T. John, M. Guenther, C. Wagner, U.F. Schaefer and C.-M. Lehr, *A Model for the Transient Subdiffusive Behavior of Particles in Mucus.* Biophys. J., 2017. **112**(1): p. 172-179.
150. Westfall, C.S. and P.A. Levin, *Comprehensive analysis of central carbon metabolism illuminates connections between nutrient availability, growth rate, and cell morphology in Escherichia coli.* PLoS Genet, 2018. **14**(2): p. e1007205.
151. Kazan, D., A. Camurdan and A. Hortacsu, *The effect of glucose concentration on the growth rate and some intracellular components of a recombinant Escherichia coli culture.* Process Biochem. (Oxford), 1995. **30**(3): p. 269-73.
152. Meglen, R.R., *Examining large databases: a chemometric approach using principal component analysis.* J. Chemom., 1991. **5**(3): p. 163-79.

153. Bren, A., J.O. Park, B.D. Towbin, E. Dekel, J.D. Rabinowitz and U. Alon, *Glucose becomes one of the worst carbon sources for E. coli on poor nitrogen sources due to suboptimal levels of cAMP.* Sci. Rep., 2016. **6**: p. 24834.

154. Lynk, T.P., C.S. Sit and C.L. Brosseau, *Electrochemical Surface-Enhanced Raman Spectroscopy as a Platform for Bacterial Detection and Identification.* Anal. Chem. (Washington, DC, U. S.), 2018. **90**(21): p. 12639-12646.

155. Popescu, A.C., P.E. Florian, G.E. Stan, G. Popescu-Pelin, I. Zgura, M. Enculescu, F.N. Oktar, R. Trusca, L.E. Sima, A. Roseanu and L. Duta, *Physical-chemical characterization and biological assessment of simple and lithium-doped biological-derived hydroxyapatite thin films for a new generation of metallic implants.* Appl. Surf. Sci., 2018. **439**: p. 724-735.

156. Marycz, K., M. Maredziak, J. Grzesiak, D. Szarek, A. Lis and J. Laska, *Polyurethane/polylactide-blend films doped with zinc ions for the growth and expansion of human Olfactory Ensheathing Cells (OECs) and Adipose-Derived Mesenchymal Stromal Stem Cells (ASCs) for regenerative medicine applications.* Polymers (Basel, Switz.), 2016. **8**(5): p. 175/1-175/17.

157. Foldberg, S., M. Petersen, P. Fojan, L. Gurevich, T. Fink, C.P. Pennisi and V. Zachar, *Patterned poly(lactic acid) films support growth and spontaneous multilineage gene expression of adipose-derived stem cells.* Colloids Surf., B, 2012. **93**: p. 92-99.

158. Martínez, J.L., L. Liu, D. Petranovic and J. Nielsen, *Pharmaceutical protein production by yeast: towards production of human blood proteins by microbial fermentation.* Current Opinion in Biotechnology, 2012. **23**(6): p. 965-971.

159. Li, Z., J. Lai, W. Liao, J. Liu and G. Wang, *Raman spectroscopic profile of ethanol fermentation in high gravity cassava starch brewing.* Guangxue Xuebao, 2012. **32**(3): p. 0317001-1-0317001-7.

Vita

Education

Syracuse University

- **Ph.D.,** Department of Chemistry, Expected August 2019. Thesis: Towards real-time monitoring of bacterial cultures without the need for physical sampling: elastic scattering, fluorescence and Raman spectroscopy of Escherichia coli cultures.
- **Master's Degree,** Department of Chemistry, August 2015. Thesis: Coupled turbidity and spectroscopy problems: a simple algorithm for volumetric analysis of optically thin or dilute, in vitro bacterial culture systems, and Optical interference probe of biofilm hydrology: label-free characterization of the dynamic hydration behavior of native biofilms.

West Virginia University

- **Bachelor's Degree,** Department of Chemistry, May 2010. Thesis: Effective Methods of Hydrogen Storage in Hydrogen Fuel Cells.

Awards

Nomination for S. A. L. U. T. E. National Honor Society for veteran and military students. January 22, 2016. Gold Member: GPA 3.50-4.00

Research Experience

Syracuse University

Research Advisor: Dr. Joseph Chaiken

- I developed a way to determine the analysis of native Escherichia coli cultures in real-time using Raman Spectroscopy to quantify the growth of a culture, the concentrations of nutrients depleted, and the concentration of products.
- I developed a technique using interference fringes to analyze the hydrology of a biofilm using UV/Vis/NIR spectroscopy, and the characterization of an underlying hydration layer that forms spontaneously in biofilms.

Publications

- Richard T. McDonough, Hewen Zheng, Mercy A. Alila, Jerry Goodisman, Joseph Chaiken, "Optical interference probe of biofilm hydrology: label-free characterization of the dynamic hydration behavior of native biofilms," J. Biomed. Opt. 22(3), 035003 (2017), doi: 10.1117/1.JBO.22.3.035003.
- Richard T. McDonough, Paul Dent, Jerry Goodisman, Joseph Chaiken, "Coupled turbidity and spectroscopy problems: a simple algorithm for volumetric analysis of optically thin or dilute, in vitro bacterial culture systems," Manuscript in Preparation, J. Appl. Spectrosc.

Work Experience

Indium Corporation

Semiconductor Product Specialist (August/2018-Present)

Bristol-Myers Squibb

Quality Control Analyst (June/2017-August/2018)

- Instruments: PerkinElmer Lambda 60 UV/Vis, Cary 50 UV/Vis, HPLC, AKTA, Autosampler (TOC and Water Testing), Centrifuge, Light Meter, pH Meter, Balance.
- Technique/Skills: Spec. Analysis (UV/Vis, and HPLC), TOC, Water Testing, Calibration Curves, Data Analysis/Review, Sample Preparation, Appearance Testing, Chlorine Testing, Receiving Samples, GMP and GLP, LIMS, Citrix, Velquest, Empower 3, Trackwise, Sterilization Procedures, and Microsoft Office (Word, Excel, PowerPoint).

Syracuse University

Research Assistant: Dr. Joseph Chaiken's Lab, Department of Chemistry (August/2013-July/2017)

- Instruments: Raman Spectroscopy, PerkinElmer Lambda 60, 650, 950 UV/Vis, PerkinElmer FT-IR, Fluorescence Spectrophotometry, HPLC, NMR, IR, Mass Spec., LC-MS, Lab Incubator Shaker, Autoclave, Centrifuge, pH Meter.
- Technique/Skills: Cell Culturing, Sterilization Procedures, Detailed/Organized Lab Notebook, Spec. Analysis (Raman, UV/Vis, FL, FT-IR, NMR, IR, Mass Spec.), Data Analysis, Microsoft Office (Word, Excel, PowerPoint), SOP Creation, Training Grads/Undergrads on Lab Equipment, ChemDraw, Origin 9.1.

Teaching Assistant: Department of Chemistry (August/2013-May/2017)

- I instructed and supervised laboratory sections for General Chemistry, Organic Chemistry, Chemistry in the Modern World, and Physical Chemistry. My responsibilities included teaching, grading, office hours.
- As lead TA, I facilitated all the TA meetings and handled any issues with students.

United States Navy

Surface Warfare Officer (August/2010-November/2012)

- I served both home and abroad honorably for the duration of my time in the Navy. I was in charge of 50-100 sailors that maintained the integrity of the ship. My responsibilities included overseeing the operation/maintenance of surface vessels, daily briefing, making sure all daily tasks were completed, naval navigation, and communication control.